

University of Alberta

**Metal Artifact Reduction in Computed Tomographic (CT) Images for
Radiotherapy Treatment Planning**

by

Moti Raj Paudel

A thesis submitted to the Faculty of Graduate Studies and Research
in partial fulfillment of the requirements for the degree of

Doctor of Philosophy

in

Medical Physics

Department of Oncology

©Moti Raj Paudel

Spring 2014

Edmonton, Alberta

Permission is hereby granted to the University of Alberta Libraries to reproduce single copies of this thesis and to lend or sell such copies for private, scholarly or scientific research purposes only. Where the thesis is converted to, or otherwise made available in digital form, the University of Alberta will advise potential users of the thesis of these terms.

The author reserves all other publication and other rights in association with the copyright in the thesis and, except as herein before provided, neither the thesis nor any substantial portion thereof may be printed or otherwise reproduced in any material form whatsoever without the author's prior written permission.

Abstract

High density/high atomic number metallic objects create shading and streaking *metal artifacts* in the CT image that can cause inaccurate delineation of anatomical structures or inaccurate radiation dose calculation.

We developed techniques for reducing metal artifacts in both megavoltage CT (MVCT) and kilovoltage CT (kVCT) images. We remodelled the iterative maximum polychromatic algorithm for CT (IMPACT) by adding a model for pair/triplet production and incorporating the energy dependent response of the detectors and successfully applied it to two MVCT systems. In the corrected image of a phantom, the error in the measured electron density of a plexiglass background was <1%. The mean deviation of measured electron density (0.295-1.695 relative to water) for a range of materials was <3%. For the kVCT beam, a thickness ≥ 13 mm of steel plate resulted in *photon starvation* at the detector. The modifications, similar to those for MVCT, made to kVCT in the IMPACT algorithm did not improve its performance due to photon starvation.

An algorithm (MVCT-NMAR) was developed that uses prior information from MVCT images to correct artifacts in kVCT. The MVCT-NMAR greatly reduced the metal artifacts in kVCT without deforming structures and did not introduce secondary artifacts except for a few faint streaks. The radiation doses calculated on those corrected images were closer to the doses in a reference image due to the more accurate CT numbers. These improvements were significant when compared to the commercial metal artifact correction method (OMAR algorithm in Philips CT scanner).

The MVCT-NMAR algorithm was further improved to remove remaining fine streakings and applied to the images of five patients. The technique greatly reduced the metal artifacts and avoided secondary artifacts. Those were significant improvements over the commercial OMAR correction method and depended upon accurate registration of the MVCT and kVCT images. Large dose reduction outside the planning target volume was observed for a prostate cancer patient when these images were used without the requirement that beams avoid passing through prostheses in TomoTherapyTM treatment plans. Thus the use of MVCT-NMAR corrected images in radiotherapy treatment planning may raise the quality of cancer treatments for patients having metallic implants.

Acknowledgement

It gives me an immense pleasure to acknowledge all the great individuals who have come across during this long journey of my PhD. I would like to dedicate this thesis and express my sincere thanks to my parents in Nepal who are a constant source of inspiration. My very special thanks to my wife Laxmi, and twin daughters Apeksha and Abhilasha for their great support and love during this time. I would like to express my deep and sincere gratitude to my thesis supervisor Dr. Satyapal Rathee for suggesting the project and for his constant guidance throughout this work. His encouragement and assistance have been invaluable. I am very much impressed with his high level of understanding in difficult times, open door policy and prompt response when it comes to helping a student which were highly motivating during this work. I am grateful to the supervisory committee members Dr. Gino Fallone, Dr. Ron Sloboda, and Dr. Marc Mackenzie for their valuable feedback and suggestions. Dr. Mackenzie helped as if he was a co-supervisor. I appreciate his help on editing the papers in spite of his hectic time schedule. I would also like to thank the external reader Dr. Janelle Molloy for her time and the valuable feedback. I am grateful to the internal external Dr. Alan Wilman for his time and constructive comments. I am thankful to Dr. Brad Warkentin and Mr. Colin Field for their help with TomoTherapy system. I would like to acknowledge all the faculty members who mentored and educated me. The project would not have been completed without the help of the machine shop, TMG and the Medical Physics staff at CCI. The Department of Oncology staff Cathy, Jen, and Cheryl were very helpful and nice. Thank you all for your contributions. I would like to thank my friends Amir and Andrei for their great help during the simulations and the experiments. Andrei also deserves special thanks for his numerous rides home during those cold winter nights. I am thankful to Danny and Dan Michael for their support in computing. I would like to thank all other friends at CCI and beyond for helpful discussions, interactions and also for the social time. I finally would like to acknowledge the funding from CIHR, Vanier CGS, FGSR, private donors and the Department of Oncology.

Table of Contents

CHAPTER 1 : Background.....	1
1.1 Overview of Computed Tomography (CT)	1
1.1.1 Interaction of x-rays with matter.....	4
1.1.2 Kilovoltage CT.....	5
1.1.3 Megavoltage CT.....	7
1.2 Uses of CT in radiotherapy	10
1.2.1 Target volume definition.....	11
1.2.2 Dose calculation.....	13
1.2.3 Image guidance	15
1.3 Metal artifacts in CT and their physical basis.....	19
1.3.1 Beam hardening	22
1.3.2 Noise and photon starvation.....	23
1.3.3 Scatter	24
1.3.4 Partial volume effect	25
1.3.5 Motion.....	26
1.3.6 Aliasing	27
1.3.7 Others.....	27
1.4 Metal artifact reduction (MAR) methods.....	28
1.4.1 Simple technical considerations.....	28
1.4.2 Correction methods with FBP image reconstruction	29
1.4.3 Model based correction methods	35
1.4.4 Mixed correction method.....	38
1.5 Motivation and goals.....	39
1.6 Outline of the thesis	43
1.7 References.....	43
CHAPTER 2 : Metal artifact reduction in MVCT using a modified IMPACT	55
2.1 Introduction.....	55
2.2 Methods and Materials.....	56
2.2.1 IMPACT modifications for MVCT	56

2.2.2 Bench-top MVCT	60
2.2.3 TomoTherapy™ Hi Art-II MVCT	63
2.2.4 Energy dependent detector calibration factor calculation.....	64
2.3 Results	67
2.3.1 Energy dependent detector calibration factor	67
2.3.2 Image reconstruction.....	70
2.4 Discussion	79
2.5 Conclusions.....	82
2.6 References.....	82
CHAPTER 3 : Modified IMPACT in kVCT	87
3.1 Introduction.....	87
3.2 Attenuation vs thickness of steel plates	87
3.3 Conclusion	91
3.4 References.....	91
CHAPTER 4 : NMAR in kVCT using MVCT priors, a phantom study	93
4.1 Introduction.....	93
4.2 Methods and Materials.....	95
4.2.1 IMPACT modifications for MVCT	95
4.2.2 Image reconstruction in MVCT	97
4.2.3 Image reconstruction in kVCT.....	99
4.2.4 NMAR with kVCT prior.....	100
4.2.5 NMAR with MVCT priors.....	101
4.2.6 Dosimetric evaluations.....	102
4.3 Results	105
4.3.1 Image reconstructed using kVCT prior.....	105
4.3.2 Images reconstructed using MVCT priors	109
4.3.3 Images reconstructed using a commercial algorithm.....	113
4.3.4 Dosimetric evaluations.....	116
4.3.5 Dosimetric evaluations of clinical plans on phantom images.....	120
4.4 Discussion	125

4.5 Conclusions.....	127
4.6 References.....	128
CHAPTER 5 : NMAR in kVCT using MVCT priors, a patient study	131
5.1 Introduction.....	131
5.2 Methods.....	132
5.2.1 Streaking reduction	132
5.2.2 Image reconstruction.....	133
5.2.3 Dosimetric evaluations.....	136
5.3 Results.....	137
5.3.1 Image quality evaluation.....	137
5.3.2 Dosimetric evaluations.....	143
5.4 Discussion	145
5.5 Conclusions.....	149
5.6 References.....	149
CHAPTER 6 : Conclusions and future work	151
6.1 Conclusions.....	151
6.2 Future work.....	154

List of Tables

Table 4.1. Physical density and electron density relative to water of the inserted plugs shown in Fig. 4.1.	106
--	-----

List of Figures

- Figure 1.1. Typical source spectrum of (a) a kVCT, and (b) an MVCT..... 10
- Figure 1.2. Illustration of definitions set by ICRU reports 50 and 62. The shapes are arbitrarily drawn..... 13
- Figure 1.3. Diagnostic kVCT image of a patient reconstructed using FBP method showing the detrimental effects (streaking, shading etc.) of bilateral hip prosthetics. 20
- Figure 2.1. Variation of measured and calculated attenuation of beam by solid water thickness for two (one central and the other outer) TomoTherapyTM MVCT detectors (a) without and (b) with energy dependent calibration factors. In (a), the measured attenuation by the two detectors is different due to different energy response while the calculated attenuation is the same. The difference between measured and calculated attenuation in (a) for each detector gets removed in (b) after applying energy dependent calibration. Similar variations for a central detector in the bench-top MVCT are in [(c) and (d)]. The energy response of the bench-top MVCT detectors is spatially invariant and a common energy response can be used to match the calculated and measured attenuation for all the detectors, two are shown in (d). Arrows in (a) indicate the corresponding curves for a given detector..... 68
- Figure 2.2. Variation of measured and calculated attenuation with solid water thickness for a central detector in TomoTherapyTM MVCT. The attenuation measured by an ion chamber follows the calculated attenuation validating the simulated energy fluence spectrum used. 69
- Figure 2.3. Images reconstructed using the FBP [(a) and (c)] and IMPACT methods after 150 iterations [(b) and (d)] with the central cortical bone insert. The inserts labeled '1' are steel rods. Top row [(a) and (b)] are TomoTherapyTM MVCT images and bottom row [(c) and (d)] are bench-top MVCT images. The window/level in (a) and (c) are the same as in (b) and (d) respectively. 71
- Figure 2.4. Comparisons of image profiles along the line joining the steel inserts (the curve with three peaks) and in the perpendicular direction to it (the curve with a central peak) in the TomoTherapyTM MVCT image (a). The uniform plexiglass background which is distorted in the FBP image is restored in the IMPACT image, shown in (b). Insets in both figures show the restored background more clearly..... 72
- Figure 2.5. Comparisons of image profiles as in Fig. 2.4 in the FBP image of (a) the TomoTherapyTM MVCT system and (b) the bench-top MVCT system, both in the absence of metal rods. Arrows indicate the uniform plexiglass background.. 73
- Figure 2.6. Comparisons of image profiles along the line joining the steel inserts (the curve with three peaks) and in the perpendicular direction to it (the curve with a central peak) in the bench-top MVCT image (a). The uniform plexiglass

background, destroyed in the FBP image is restored in the IMPACT image in (b). Insets in both figures show the restored background more clearly..... 74

Figure 2.7. Variation of average pixel values with relative electron density in the (a) FBP reconstructed and (b) IMPACT reconstructed bench-top MVCT images for a central insert in the presence (circles) and absence (diamonds) of peripheral steel inserts. The average pixel values in the IMPACT reconstructed images in the presence of steel inserts are close to the corresponding values in the absence of steel inserts within the experimental uncertainty. The red and blue curves are the linear fits to the corresponding points..... 74

Figure 2.8. Variation of average pixel values with relative electron density in the (a) FBP reconstructed and (b) IMPACT reconstructed TomoTherapy™ MVCT images for a central insert in the presence (circles) and in absence (diamonds) of peripheral steel inserts. The average pixel values in the IMPACT reconstructed images in the presence of steel inserts are close to the corresponding values in the absence of steel inserts within the experimental uncertainty. The red and blue curves are the linear fits to the corresponding points. 76

Figure 2.9. Variation of mean pixel values of the plexiglass background with relative electron density in the shadow (1) and out of the 'shadow' (2) of the steel rods in the FBP and IMPACT reconstructed images from (a) the TomoTherapy™ MVCT system and (b) the bench-top MVCT system..... 77

Figure 3.1. The attenuation measured by the central detector for three different thicknesses of steel plates sandwiched between two solid water blocks each 12 cm thick. Here, a view number corresponds to a particular couch position in the scout scan mode while the source and detectors remained stationary. For steel thickness of 18.4 mm (a) and somewhat for 13.4 mm (b), the variation in measured attenuation is reflective of quantization noise indicated by the presence of a finite number of discrete levels. This indicates that the detector signal is so small that the quantization levels in the A-to-D converter are visible. This is not the case for a steel thickness of 10.6 mm (c) where the variations in the measured attenuation are characteristics of quantum mottle. 88

Figure 3.2. Histogram of the attenuation measured by the central detector for varying thicknesses of steel plates sandwiched between two solid water blocks each 12 cm thick. Here, number of views indicates a particular couch position in the scout scan mode for which a particular value of attenuation was recorded while the source and detectors remained stationary. The histograms from (a) to (c) show the broadening of the attenuation distribution curve, indicating the rise in quantum noise with the increase in steel plate thickness. When the steel thickness reaches 13.4 mm (d), new discrete lines appear, one of them at the largest attenuation value of 18.6. Starting at the steel thickness of 18.4 mm (e), the Gaussian-like shape of the histogram completely disappears and the discrete lines are seen at the same attenuation values with increasing height, reflecting the quantization levels in the A-to-D conversion process. 90

Figure 4.1. (a) RMI tissue characterization phantom and (b) TomoTherapy™ cheese phantom; kVCT images of (a) and (b) without metal plugs in (c) and (d)

respectively. The physical properties of the inserts used are listed in Table 4.1. Either the steel inserts [indicated by arrows in (a) and (b)], or water equivalent plugs were inserted in positions '1' and '6' to simulate a bilateral metal implant or artifact free images. The window width/level of the CT images is 1500/0 HU. 106

Figure 4.2. Original FBP reconstructed image of the RMI phantom (a) after correction with NMAR method with kVCT prior (b). The image corrected by the regular PC method with linear interpolation (c) is segmented to provide the prior image (d) for NMAR. The arrows show distorted edges and eroded regions of the structures in the prior and final corrected images. Image window width/level is 1500/0 HU. The inset shows the degraded area inside the lung insert (location 11) for a different (500/-500 HU) window width/level..... 108

Figure 4.3. Profiles through various sections of the corrected image in Fig. 4.2(b) compared with the corresponding profiles in the reference image. Arrows indicate the deformed edges, eroded regions, and large deviation of CT number within the inserts in the corrected image. The fluctuations are predominant in lung, bone and metal inserts. Inset in each panel shows the line in the image along which the profile is taken..... 109

Figure 4.4. (a) Original FBP reconstructed MVCT image of the RMI phantom (b) after correction using modified IMPACT method. The transformed pseudo kVCT images (c) and (d) from images (a) and (b), respectively, are used as prior images in NMAR technique to reconstruct images (e) and (f) in kVCT. Most of the inserts in (e) and (f) are not deformed and clearly visible. However, there are remaining subtle streaks and shadings that have passed from the prior images. Image window width/level is 1500/0 HU. 111

Figure 4.5. Profiles through various regions of the image in Fig. 4.4(e) corresponding to Fig. 4.3. The profiles in the corrected image are very close to the corresponding profiles in the reference image for all the inserts including metal. Although the profiles are noisier inside the inserts, the edges are intact in the corrected image. Inset in each panel shows the line in the image along which the profile is taken..... 112

Figure 4.6. Profiles through various regions of the image in Fig. 4.4(f) corresponding to Fig. 4.3. The profiles in the corrected image are very close to the corresponding profiles in the reference image for all the inserts including metal. Although the profiles are noisier inside the inserts, the edges are intact in the corrected image. Inset in each panel shows the line in the image along which the profile is taken..... 113

Figure 4.7. Image of the RMI phantom corrected by the OMAR algorithm in the Philips CT scanner. The arrows show distorted edges and eroded regions of the structures in the image. Image window width/level is 1500/0 HU. 114

Figure 4.8. Profiles through various regions of the image in Fig. 4.7 compared with the reference image. Arrows indicate the deformed edges, eroded regions, and large deviation of CT number within the inserts in the corrected image. The

fluctuations are predominant in lung, bone and metal inserts. Inset in each panel shows the line in the image along which the profile is taken. 114

Figure 4.9. Comparisons of dose distributions for 6 MV 5 x 10 cm² parallel opposed fields calculated on (a) the reference image, (b) the image corrected using an IMPACT corrected MVCT prior, (c) the image corrected using a FBP reconstructed MVCT prior, and (d) the image corrected using a kVCT prior. The irradiation setting for both the fields is 280 MU. The image window width/level is 1500/0 HU..... 117

Figure 4.10. (a) Variation of calculated dose within the 10 cm width of the beams at the isocentric plane of the images in Fig. 4.9. The arrow shows the point of largest dose difference relative to the dose in the reference image. The arrow in the inset image shows the location and direction of the profiles in the image. (b) The calculated dose profile of the reference image is compared with the measured dose measured using gafchromic film. 119

Figure 4.11. (a) The calculated dose distribution of a four field plan in the reference image. (b) The calculated dose profiles along the arrow shown in the inset for various metal artifact corrected images relative to the reference image. 120

Figure 4.12. Comparisons of dose distributions for a rapid arc plan (a-e) and a seven field IMRT plan (f-j) optimized for prostate patients calculated on (a, f) the reference image, (b, g) the image corrected using an IMPACT corrected MVCT prior, (c, h) the image corrected using a FBP reconstructed MVCT prior, (d, i) the image corrected using a kVCT prior, and (e, j) the OMAR corrected image. The doses are normalized to a prescription dose of 200 cGy at the isocenter for both the plans. The image window width/level is 1500/0 HU..... 124

Figure 5.1. Flow diagram showing the MVCT-NMAR technique. In the corrected image, the metal pixels are set to zero and used again as the prior image in an iterative fashion to reduce the fine streakings. Metal pixels are inserted back in the final corrected image. Three iterations are used in this study..... 133

Figure 5.2. (a) Original uncorrected image (b) OMAR corrected image, MVCT-NMAR corrected images after (c) one iteration and (d) three iterations. The streaks present in (c) are successfully removed in (d). In (b) arrows 1, 2, and 3 show an obscured region anterior to the bladder-rectum interface, lost bone information, and blurred soft tissue close to metal implant, respectively. All of these artifacts are removed in (d) shown by the respective arrows. 138

Figure 5.3. (a) OMAR corrected image and (b) MVCT-NMAR corrected image of a prostate patient with dual hip implants. In (a) arrow 1 shows part of the bladder with higher CT number and arrow 2 shows an obscured region near the bladder-tissue interface. These artifacts are removed in (d) shown by the respective arrows..... 139

Figure 5.4. Four successive image slices of patient no 2 showing prostate, bladder and rectum. The images in the top row (a-d) are corrected by the OMAR algorithm and those in the bottom row are corrected using the MVCT-NMAR

method. In the OMAR corrected images, arrows 1 show an obscured region near the prostate-bladder or prostate-rectum interface, arrows 2 show bladder with higher CT number and arrows 3 show eroded bone regions. These artifacts are removed in the MVCT-NMAR corrected images making tissue structures more visible..... 140

Figure 5.5. (a) OMAR corrected image and (b) MVCT-NMAR corrected image of a female patient with a single hip prosthesis. In (a) arrow 1 shows blurred soft tissue close to the implant, arrow 2 shows eroded bone, and arrows 3 show obscured regions near bladder-tissue-rectum interfaces. These artifacts are removed in (b) as shown by the respective arrows. 141

Figure 5.6. Two successive image slices of a head and neck patient with dental implants: (a) uncorrected images; (b) OMAR corrected images; and (c) MVCT-NMAR corrected images. In (b) for both slices arrow 1 shows remaining artifacts, arrow 2 shows false bony anatomy, and arrow 3 shows a false air gap. These artifacts are removed in (c) as shown by the respective arrows..... 142

Figure 5.7. (a) Differential dose histogram in the planning target volume (PTV) showing the difference in dose of image sets corrected by the MVCT-NMAR and OMAR algorithms for a radiotherapy plan created without blocking the beams through the prostheses. The plan was optimized on an OMAR corrected image set and recalculated on an MVCT-NMAR corrected image set. (b) The dose profiles through the PTV of these images (along a line shown in the inset) show a small (shown by arrow) but constant dose difference. The difference results from the lower CT number inside the metal prostheses and in the shaded region between them in the OMAR corrected images. 144

Figure 5.8. (a) Dose profiles through a slice containing PTV, along a line as shown in inset, in the image corrected by MVCT-NMAR using two plans (one with beams blocked through the prostheses and the other with beams unblocked) showing significantly higher dose outside PTV in the blocked beam plan compared to the dose in unblocked plan. (b) Similar dose profiles in another slice containing pubic bone where there is 12.8% higher dose in the blocked beam plan compared to the unblocked beam plan. Inset in (a) is the dose distribution image whereas the inset in (b) is the CT image. 145

List of Abbreviations

2D	Two dimensional
3D	Three dimensional
A-to-D	Analog to digital
AAA	Anisotropic Analytical Algorithm
AAPM	American Association of Physicists in Medicine
AM	Alternative maximization
CRT	Conformal radiotherapy
CT	Computed tomography
CTV	Clinical target volume
DQA	Delivery quality assurance
DQE	Detective quantum efficiency
DRR	Digitally reconstructed radiographs
DSP	Digital signal processing
EPID	Electronic portal imaging detector
FBP	Filtered backprojection
FOV	Field of view
GTV	Gross tumour volume
HU	Hounsfield unit
ICRU	International Commission on Radiation Units and Measurements
IGRT	Image guided radiotherapy
IM	Internal margin
IMPACT	Iterative maximum-likelihood polychromatic algorithm for CT
IMRT	Intensity modulated radiotherapy
kV	Kilovoltage
kVCBCT	kilovoltage cone beam computed tomography
kVCT	Kilovoltage computed tomography
linac	Linear accelerator
MAP	Maximum a posteriori

MAPPC	Maximum a posteriori-based projection completion
MAR	Metal artifact reduction
MC	Monte Carlo
ML-TR	Maximum likelihood in transmission tomography
MRF	Markov random field
MRI	Magnetic resonance imager
MRS	Magnetic resonance spectroscopy
MUs	Monitor units
MV	Megavoltage
MVCBCT	Megavoltage cone beam computed tomography
MVCT	Megavoltage computed tomography
MVCT-NMAR	Normalised metal artifact reduction using MVCT prior
NIST	National Institute of Standards and Technology
NMAR	Normalized metal artifact reduction
OBIs	On board imagers
OMAR	Orthopaedic metal artifact reduction
OR	Organ at risk
PC	Projection completion
PET	Positron emission tomography
PRV	Planning organ at risk volume
PTV	Planning target volume
QA	Quality assurance
RF	Radio frequency
ROI	Region of interest
SAD	Source to axis distance
SM	Setup margin
SNR	Signal to noise ratio
SPECT	Single photon emission computed tomography
TV	Treatment volume

CHAPTER 1 : Background

1.1 Overview of Computed Tomography (CT)

X-ray computed tomography (CT) is an imaging modality that yields cross-sectional images of an object. Each pixel (picture element) in the image represents the attenuation characteristics of the object in that plane. The attenuation characteristic called *linear attenuation coefficient* (μ), relates the incident (I_0) and transmitted (I) intensities of a narrow collimated monoenergetic x-ray beam passed through a thickness (L) of a tissue/structure in the patient body by:¹

$$I = I_0 \exp(-\mu L) \quad 1.1$$

It is a function of x-ray energy, and the atomic number and electron density of the tissue. In clinical practice, a thin fan-beam of x-rays, wide enough to cover the required field of view, is passed through the patient, and the transmitted radiation is detected by an array of detectors. This process is repeated for multiple discrete azimuthal views by rotating the radiation source-detector assembly in a gantry about the patient. The detector data is converted into a sum of attenuations [$\ln(I_0/I) = \sum \mu dL$] along the beam path for each detector (i.e., line integral of linear attenuation coefficient) and an image is reconstructed using these line integrals. These data are called *projection data*. The Cartesian representation of projection data with the detector number in the array and view angle as the two coordinate axes is called a *sinogram*¹. The most common image reconstruction algorithm is *filtered backprojection* (FBP)² where the projection

data for each view is convolved with a filter function and then backprojected in 2D image space, summing the backprojected result for all view angles.

The attenuation coefficients in a CT image are usually expressed in *Hounsfield Units* (HU), the shifted and normalized whole number with respect to water also called CT number¹:

$$CTnumber = \frac{\mu_{tissue} - \mu_{water}}{\mu_{water}} \times 1000HU \quad 1.2$$

With this definition, water and air (more correctly vacuum) have CT numbers of 0 HU and -1000 HU respectively. Because of the very high dynamic range of CT numbers represented in a single image, a gray scale transformation is applied to the selective visualization of tissues in the region of interest. The transformation is represented by *window* and *level* which are the total span and center of the CT numbers around the center to be displayed in the image respectively. After the transformation, the CT numbers below the range become visually black and those above visually white.

The history of CT can be dated back as early as the accidental discovery of x-rays by Wilhelm Konrad Rontgen³, who got the first Nobel Prize in Physics in 1901. The idea of a reconstruction of a function from its projections, called a Radon transform⁴, was first formulated by Johann Radon in 1917. However the first CT scanner was developed by Godfrey N. Hounsfield⁵ in 1972 based on the mathematical and experimental methods developed by A. M. Cormack^{6,7} in 1963. Both Hounsfield and Cormack shared the 1979 Nobel Prize in medicine and physiology for their work.

Most of the modern clinical CT scanners are *third generation* scanners where the detector array is focussed onto the x-ray source and the x-ray source and detector assembly rotate in unison around the patient. The volumetric data is acquired by scanning in a slice by slice fashion: either by translating the patient couch to discrete positions (axial scan) or in a continuous motion (spiral or helical scan).⁸ Data acquisition with continuous rotation of the source-detector during the continuous patient translation through the rotating x-ray beam in helical scanning is made possible with slip-ring technology.⁸ A further advancement in CT is the introduction of multidetector technology where several rows of detector-arrays are illuminated by the x-ray source at the same time resulting in very fast scanning.⁸ This reduces the motion related artifacts and improves image quality. The CT detectors are arranged in an arc focussed onto the source for efficient detection.

Historically, the CT detectors contained scintillation materials (convert x-ray energy into visible light) coupled with photomultiplier tubes that detect the light photons and convert them to the electrical signal. Modern day CT detectors are either comprised of an arc shaped container of compressed gas such as xenon under 10 to 30 bars pressure and electrodes of high density metals (such as tungsten) for detecting gas ionizations or solid state scintillators (NaI:Ti, CsI:Ti, CdWO₄, Bi₄Ge₅O₁₂, Gd₂O₂S:Tb etc.) joined to the photodiodes.⁸ The gas detectors have higher packing density compared to photomultiplier tube system but have low absorption and geometrical efficiencies compared to solid state detectors. The absorption efficiency measures how efficiently the incident x-ray

quanta are converted into a measurable signal. Solid state detectors have high absorption efficiency (more than 98%), fast response time in addition to high packing density. The most recently used commercial ceramic detectors have ultrafast response time. The signal from a detector in CT gives an estimate of the total energy fluence incident on a detector element, and is a strong function of detector material and photon energy.

1.1.1 Interaction of x-rays with matter

At very low energies (<20 keV) the incident x-ray photons interact with bound atomic electron via two processes. In the process called *Raleigh scattering (or Coherent scattering)* the photons are scattered elastically.⁹ In the same energy range the incident photons may completely disappear in bound electron interactions, knocking out the inner orbit electrons. The process is called *photoelectric effect*.⁹ At a higher energy range (>60 keV), the photons interact with a free electron and get scattered. The term *free* means that the binding energy of the electron is much less than the energy of the incident photon. Atomic electrons in outer orbits take part in this interaction. A part of the incident energy is imparted to the recoiled electron. Both the scattered photon and electron travel at various angles determined by the laws of energy-momentum conservation. This process is called *Compton scattering or incoherent scattering*.⁹ At energies greater than 1.02 MeV the x-ray photons may also interact with the nuclear Coulomb field where the interacting photon gets disappeared creating electron-positron pair. This process is called *pair-production*.⁹ For energies

greater than 2.04 MeV, the photon may interact in the Coulomb field of an orbital electron to create an electron-positron pair, a process known as *triplet production*. At incident energies greater than 10 MeV neutrons may be produced in *photo-nuclear* reactions.⁹

The mass attenuation coefficient (the linear attenuation coefficient divided by the density of an object) for coherent scattering and photo-electric process are approximately proportional to the inverse of second and third power of x-ray energy respectively. For Compton interaction the mass attenuation coefficient decreases with energy whereas it increases for pair production. The sum of the attenuation coefficients for all these processes for a medium is the linear attenuation coefficient defined in Eq. (1.1). Furthermore, the atomic number (Z) dependence of both the Raleigh and pair production processes (mass attenuation coefficients) is approximately linear with Z .⁹ For Compton interactions, it (mass attenuation coefficient) is independent of Z but varies linearly with electron density or number of electrons per gram (ρ).⁹ The mass attenuation coefficient for photoelectric process varies roughly as Z^3 for high Z materials like metals and as $Z^{3.8}$ for low Z materials like water.⁹

1.1.2 Kilovoltage CT

Based on the energy of the x-ray source, there are two categories of CT scanner: kilovoltage CT (kVCT) and megavoltage CT (MVCT). Due to the variation in the physics of production, interactions with tissue, and detection of

x-rays at these two energies, the source-detector system and clinical applications differ significantly between kVCT and MVCT.

Conventional diagnostic scanners are kVCT and use an x-ray tube as the radiation source that produces a polychromatic photon beam in the range of 30-140 keV. The electrons, boiled off the hot filament of high melting point/high density metals like tungsten, are accelerated electrostatically in a high vacuum system towards the anode. The accelerated electrons are slowed down in a target material such as tungsten that produces x-rays of continuous energy up to the peak accelerating potential through the *Bremsstrahlung* process (radiation produced when incident electrons slow down in the nuclear field of target atoms). A small fraction of multiple, single energy (*characteristic*) photons may be produced when the outer orbit (such as L, M,..) electrons in the target jump to fill the vacant position created by incident electrons in the lower energy orbits (such as K). Since most of the electrons lose their energy through excitation and ionization, a huge amount of energy carried by electrons gets lost in the form of heat and only about 1% gets converted into x-rays. The conversion efficiency increases with energy of the incident electrons and the atomic number of the target. This heating of target material limits the time for continuous imaging. Usually, a filter of lower atomic number metals such as aluminum, copper, and beryllium etc. is used to remove the lower energy photons that are otherwise absorbed in the patient and increase radiation dose without contributing to detector signal.⁹

kVCT images have high contrast resulting from the large *Z*-dependence of the photoelectric process, even though less than 10% of interactions occur through

this process in the photon energy range of the highly filtered beam. Low contrast resolution in water-like tissues comes from Compton interactions that account for around 90% of all photon interactions, and hence the CT number is proportional to the electron density. However, due to the photoelectric effect this CT number to electron density linearity is piecewise continuous for a wide range of CT numbers corresponding to the various tissues (from lung to bone) found in the human body.⁹

1.1.3 Megavoltage CT

Although cobalt-60 has been used in the past,¹⁰ polyenergetic megavoltage x-ray beams in modern MVCT units are produced by linear accelerators^{11,12} (linacs). A linac can produce x-ray beams with higher peak energies than the x-ray tubes. In the linac, electrons from an electron gun are accelerated with the help of microwave power (radiofrequency electromagnetic waves) in a waveguide, a structure that contains a series of metal cavities to sustain travelling or standing electromagnetic waves. The electrons “ride” on these waves and get accelerated before impinging upon a target (usually Tungsten) thick enough to stop them. The forward directed *Bremsstrahlung* radiation is used as the photon source for MVCT.

The majority of photon interactions in human tissues at megavoltage energies are Compton scattering. So, the tissue contrast in an MVCT image depends on the electron & physical density and is significantly poorer compared to a kVCT image where the small contribution from the photoelectric effect adds

to image contrast. The ability to resolve small soft tissue contrast differences is limited by the number of photons (determined by the detector signal) used for imaging because the detector noise is increased as the number of detected photons is decreased. Although the value of mass energy absorption coefficient, which represents the average fraction of beam energy absorbed per interaction in soft tissue, is similar for both kV and MV photons, each interacting higher energy megavoltage photon deposits more energy to patient tissues.¹³ Although a lower interaction probability at higher energies counteracts this effect, generally the photon fluence incident on the patient must be decreased to limit the imaging dose. This decreases the photon fluence incident on the detector and coupled with the poor absorption efficiency of the detectors, the overall noise in the detector signal increases in MVCT for the typical imaging dose range (1-5 cGy) used in clinic. The reduced *signal to noise ratio* (SNR) in the resulting MVCT images limits our ability to visually differentiate small soft-tissue organs against background to an extent that is significantly poorer in MVCT compared to kVCT. However, MVCT has two major potential advantages over kVCT imaging that makes it useful in radiotherapy:

1. Since the radiotherapy treatment beam is also at MV energy, attenuation coefficients need not be extrapolated from diagnostic to therapeutic energies.
2. MVCT is less susceptible to imaging artifacts due to high density metal objects such as hip implants or dental fillings.

The megavoltage x-rays are more penetrating than kilovoltage. So, the detectors must have a modified design for efficient beam detection. Often, MVCT functionality is an integral part of the unit used for treatment, and imaging is performed in the treatment position during fractionated *image guided radiotherapy* (to be discussed later). Consequently, electronic portal imaging detectors (EPIDs) that are used to get portal radiographs have been used as detectors for cone beam MVCT applications.^{12,14} The state of the art, sensitive EPIDs, contain a thin copper plate below which a scintillator plate (e.g. Gd₂O₂S:Tb) is overlaid on top of light sensing flat panel active matrix photodiodes made of amorphous silicon.^{15,16,17} In a particular ionization gas type detector array employed in the commercial TomoTherapyTM MVCT system, long thin metal septa within the gas are focussed to a point different than the source and hence serve as an energy converter to increase quantum efficiency.¹⁸ The majority of interactions of the incident MV photon beam take place in the tungsten septa plates, producing lower energy electrons and photons that ionize the high pressure xenon gas. The charge produced in the gas is collected by applying an electric potential to the alternate septa plates. In research MVCT systems, solid state detectors containing segmented thicker and denser scintillating crystals¹⁹⁻²² individually attached to photodiodes are used for this purpose. The dead space between detector elements is often reduced by using thinner septa. To control the spreading of optical photons generated within one scintillator element to its neighbours, and hence to prevent the possible degradation of spatial resolution, segmented detectors with highly reflecting septa

are used.²² The overall spatial resolution of the imaging system depends on the size of the x-ray source, the detector element size, the number of detector elements in the array, along with other parameters such as the shape of the filter function used in the filtered backprojection method. The spreading of the optical light via scattering in non-segmented granular scintillators, such as $\text{Gd}_2\text{O}_2\text{S:Tb}$, is however a major limitation to spatial resolution if the scintillator's thickness is increased to improve the overall detector efficiency. The treatment beam's source size is usually bigger than that of the diagnostic x-ray tube's focal spot and thus also limits the spatial resolution achievable.

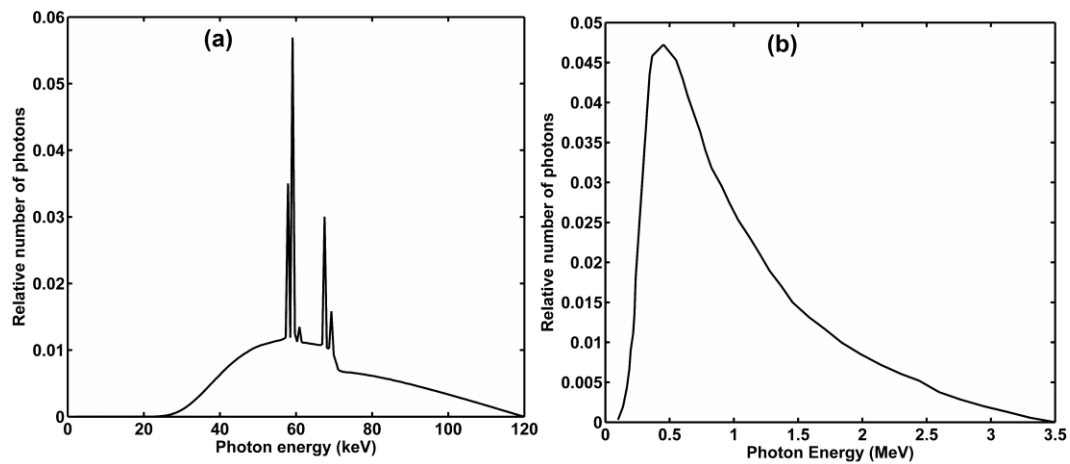


Figure 1.1. Typical source spectrum of (a) a kVCT, and (b) an MVCT.

1.2 Uses of CT in radiotherapy

The outcome of a radiotherapy treatment in theory should depend upon the accuracy by which the dose prescription is fulfilled. This means the accurate amount of prescribed radiation dose needs to be delivered to the target volume containing cancerous tissue in 3D. CT is an integral part of the radiotherapy process and plays a vital role for a successful treatment outcome. There are three

major processes in radiotherapy where CT images are extensively used: target volume definition, dose calculation and image guidance before each delivery.

1.2.1 Target volume definition

After radiotherapy is chosen as the treatment modality, the very first step in the treatment planning process is to determine the tumour location and its extent. Radiotherapy is an agent for local/regional tumour control and hence errors in target volume assessment can cause radiotherapy failure. The *target volume* means a volume that includes the tumour which is demonstrated through imaging means and its spread to surrounding tissues or lymphatics. There is no imaging modality that is capable of revealing the entire extent of the tumour with its microscopic spread. The visible tumour, as often seen through imaging, is a part of the tumour volume called the *gross tumour volume* (GTV). The GTV plus the invisible microscopic disease region that can only be estimated clinically is called *clinical target volume* (CTV). Added to the uncertainty of microscopic spread are the uncertainties of target volume localization in space and time resulting from physiological organ motion, breathing, patient setup, and positioning instabilities. The CTV with added margin for these uncertainties is called the *planning target volume* (PTV), which needs to be encompassed within a certain range of prescribed radiation dose (e.g. 90%-107%). In addition, there is a further margin added to the PTV to account for limitations of the treatment units such as beam penumbra or for contouring accuracy and the final volume inscribed

by the open treatment beam portals: this results finally in the *treatment volume* (TV).

Because of the importance of the accurate determination of PTV and its localization, the International Commission on Radiation Units and Measurements (ICRU) has set up a systematic approach for defining these volumes and margins for the tumour²³ as well as for the *organs at risk*²⁴ surrounding the tumour in ICRU reports 50²³ and 62.²⁴ ICRU 62 defines a margin for organ motion [internal margin (IM)] and a margin for setup and positioning instabilities [setup margin (SM)] separately. CTV with added IM and SM gives PTV. New from ICRU 50 is the definition of organ at risk (OR) and planning organ at risk volume (PRV). Figure 1.2 illustrates the schematic definitions of these volumes.

Diagnostic imaging for target volume definition is made in a dedicated kVCT scanner that generates a 3D image volume. CT is used in target volume definition as the primary modality due to its geometric accuracy and fast scanning. Other modalities like magnetic resonance imaging (MRI), magnetic resonance spectroscopy (MRS), positron emission tomography (PET), single photon emission computed tomography (SPECT) etc. are often combined with CT to help identify the clinical extent of tumours (i.e. CTV)²⁵⁻²⁸ because these modalities can provide important spatial information about biologically relevant characteristics of tumour such as regions of hypoxia, or high cell proliferation or density. MRI has superb soft tissue contrast and the contrast is not affected in the areas surrounded by thick bones where CT can have reduced contrast due to elevated absorption of x-rays by bone. However, MRI is unable to image the bone

itself, lacks electron density information, and cannot be readily used in patients with metallic implants because of their magnetic properties (MRI unsafe) and geometrical distortions they produce in the image. While a dedicated low-field MRI system [e.g., Philips Ingenua MR-RT Oncology Configuration (Philips Healthcare System, Cleveland, OH, USA)] with reduced geometrical distortion, (i.e. low magnetic field inhomogeneity and high linearity of gradients) is currently available as a primary imaging modality for radiotherapy planning, dedicated diagnostic CT scanners remain more prevalent for this role.

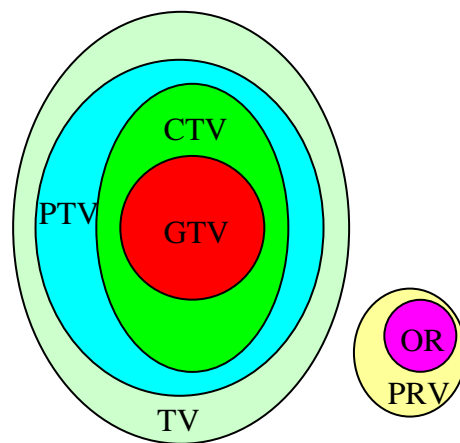


Figure 1.2. Illustration of definitions set by ICRU reports 50 and 62. The shapes are arbitrarily drawn.

1.2.2 Dose calculation

All modern radiotherapy treatment planning systems use a fully 3D point by point or voxel by voxel representation of the patient. A CT image set of the treatment region constitutes the most accurate representation of the patient applicable to the dose computation. This is because there is a fairly reliable one to one correspondence between CT number and electron density.²⁹ However, this

correspondence is sensitive to the kilovoltage energy setting in each scanner and needs to be calibrated routinely. The accuracy of CT numbers is typically within $\pm 2\%$ which corresponds to ± 20 HU and for a megavoltage treatment beam this uncertainty leads to dose calculation uncertainty of $< 1\%$.²⁹

The dose deposited in tissue by a megavoltage beam is proportional to electron density, because of the predominance of the Compton process. Traditionally, one can compute the dose just by replacing the patient anatomy with water, as there is only a small variation in electron densities among major soft tissue types from water. However, there can be a large variation in dose in the presence of significant media change both in terms of density as well as effective atomic number, such as that occurs in lung, air cavities, bone and metallic implants. Further, the contour of a patient is not like a flat slab of water and therefore doses measured in a water tank need contour correction. Heterogeneity correction can result in -10% to $+30\%$ changes in dose distal to lung depending on the size of the field and the lung thickness.³⁰ This indicates how important it is to have correct CT numbers in the image. The pixel by pixel heterogeneity corrections including the contour correction are made using electron density information (as in superposition-convolution type algorithms) or both electron density and atomic number (as in Monte-Carlo based algorithms).

In routine clinical practice, kVCT images are used for radiotherapy dose calculation. However, due to the benefits outlined in section (1.1.3), MVCT could be more accurate and suitable for dose calculation; especially in case of patients with metallic implants.

1.2.3 Image guidance

Treatment techniques such as 3D-conformal radiotherapy (3D-CRT), intensity modulated radiotherapy (IMRT), and proton therapy involve planned dose distributions that have sharp dose gradients between the target and surrounding tissues. There can be substantial inter- and intra-fractional variations in shape, volume and position of these tissues due to various reasons such as: positioning errors, respiratory motion, non-rigidity of body, weight loss or shrinkage in tumour after radiation delivery. To guide the radiotherapy process with reduced PTV margins and reduced normal tissue toxicity, frequent imaging in the treatment room is used. This technique is called *image guided radiotherapy* (IGRT).

Various technologies have been used to image the patient to evaluate and minimise the systematic errors in daily patient set-up on the treatment couch. Two dimensional (2D) projection radiographic imaging using the MV treatment beam and retractable EPIDs³¹⁻³⁴ mounted on the same gantry is a common practice which is also used to verify the shape of the treatment beam portals³⁴⁻³⁶. These images are compared with the digitally reconstructed radiographs (DRR) created using a CT simulator, a dedicated radiation therapy CT scanner with accessories such as a flat couch top, laser light for positioning, immobilization devices and image registration software to reproduce the treatment conditions. MV imaging is a low cost method for direct in-field verification of treatment delivery³⁷ but it includes high imaging dose (typically 1 to 5 cGy) and has poor image quality.

More recently, a separate kV source and flat panel detector mounted orthogonal to the therapy beam in a linac has been used. These on-board imagers (OBIs) help enhance bone contrast at low imaging dose although it adds complexity and cost.

Three dimensional volumetric imaging in IGRT is provided by both fan and cone beam CT in the kV and MV energy range. Unlike radiographs, CT images provide volumetric anatomy information and an electron density map with increased contrast in the treatment room coordinates. These in-room CT images taken just before the treatment may allow for, in principle, image guided adaptive radiotherapy by modifying the treatment parameters to adapt to changes in the patient's anatomy before each treatment or during the course of radiotherapy.

For CT guided radiotherapy, the first integrated clinical system combining a linac and in-treatment-room conventional CT unit was developed by Uematsu *et al.* in Japan.³⁸ In this system, by using a common sliding couch top, a CT scanner couch and a linac table could be aligned for smooth patient transfer to the linac immediately after CT image acquisition. The first commercial CT-linac system in the USA installed in 2000 consists of a Siemens medical linac and a movable Siemens CT scanner that can slide along a pair of rails: the so called *CT-on-Rails*.³⁹ These systems require a larger room and are more expensive.

The TomoTherapyTM Hi-Art II system has an integrated helical MVCT scanner with a linac waveguide^{11,13} detuned to provide a 3.5 MV⁴⁰ photon beam for imaging in a linac that would otherwise produce a 6 MV treatment beam. This system does not contain a flattening filter and is designed for IMRT treatments.^{11,13} Low dose (1-3 cGy) pre-treatment images can be reconstructed

using 540 channels out of 738 xenon gas detectors in the 40 cm wide field of view.⁴⁰ In spite of poor MVCT image quality, these relatively low dose images provide sufficient contrast to enable daily patient set up verification with respect to the treatment beam coordinates.⁴⁰⁻⁴² These images could be sufficient to delineate many anatomic structures and are reliable for dose verification^{40,42,43}. The system is useful for providing IGRT for patients with metallic implants.

Using large area sensitive flat panel imagers¹⁵⁻¹⁷ optimised for MV photon detection and the MV treatment beam, volumetric cone beam CT images can be reconstructed using the portal images (projections) obtained by rotating gantry around the patient, and a cone beam reconstruction algorithm⁴⁴ which is essentially the filtered backprojection algorithm. These megavoltage cone beam CT (MVCBCT) images suffer from a large amount of scattered photons reaching the wide-side detectors (EPIDs) but have better image quality compared to the projection radiographs which contain the overlaid anatomical information. Both TomoTherapyTM MVCT and MVCBCT have advantages vs. kVCT in application for patients with implanted metal objects.^{45,46} Further, the physics of the therapy beam is well understood in the patient geometry. The additional dose due to MVCBCT imaging can be accurately calculated and could be included as a part of the treatment plan.^{45,46}

Similarly, using these sensitive EPIDs in an OBI, kilovoltage cone beam CT (kVCBCT) images can be obtained which have better soft tissue contrast.^{47,48} The advantage of these systems is that they are multifunctional: radiographs or volumetric tomographic images or fluoroscopic images can be obtained using a

single imaging unit mounted in therapy room coordinates having the same isocenter. This gives flexibility in a variety of clinical applications. Although a significant x-ray scatter contribution exists in kVCBCT, it can be reduced by using post-processing⁴⁹ as done in the Electa system (Electa Synergy, Electa Inc., Sweden) or by using an anti-scatter grid.⁴⁵

In the thoracic and abdominal regions, 3D CT images reconstructed at various respiratory phases can be used to provide images to obtain a motion trajectory using 4D CT systems. However, the pre-treatment 4D images obtained using 4D kVCBCT are poor in quality and can't be used for real-time motion tracking because they are retrospectively gated. Besides CT, ultrasound, radio-frequency (RF) and optical tracking have been used for image guidance and are non-ionising methods of imaging. Ultrasound can give non invasive image guidance but the image quality is usually poor compared to CT except at certain sites such as prostate⁵⁰ and the image quality can depend upon the skills of the user^{51,52}. Ultrasound use is limited to the areas accessible to the probe. RF⁵³ tracking works using a radiofrequency transponder implanted within or near the tumour in the patient and an array of external antennae that track the position and motion of the tumour. Optical tracking⁵⁴ uses an infrared camera and reflecting markers placed on the patient surface to track the breathing motion pattern as a surrogate of the tumour motion. Both of these methods are similar to using fiducial markers, which are opaque to x-rays, as the tumour surrogates. They provide non-volumetric, indirect, limited, and sometimes uncorrelated information of tumour motion with no information about the shape of the tumour

and organs at risk. For real time tumour guidance using MRI, active research is being carried out to integrate an MRI with a linac in our department here at Cross Cancer Institute.⁵⁵

1.3 Metal artifacts in CT and their physical basis

Theoretically, any discrepancies between the reconstructed values of attenuation coefficients in CT images from their corresponding true values that are clinically significant in terms of their use in diagnostic radiology, radiation oncology and other areas are referred to as the image artifacts. Image artifacts are created due to many factors such as the nature of the physics at different photon energies, suboptimal system design, patient characteristics, limitations of the technologies, and inappropriate or suboptimal use of the scanner by the operator.

High density-high atomic number metallic objects can be used inside or on the surface of the body such as implants and applicators used in brachytherapy, cochlear simulators and receivers,⁵⁶ implantable orthopaedic appliances like screws and pins, surgical clips and staples,⁵⁷⁻⁵⁸ angiographic stents,⁵⁹ bolus rings, hip implants, and dental fillings or equipment attached to the patient's body such as biopsy needles.⁶⁰ They attenuate the x-ray beam much more significantly than human tissues due to both Compton and photoelectric effects and create black and white streaks, shadings, blurring etc. leading to the creation of false or missing anatomical structures or obstruction of proper visualization of the structures.⁶¹ For a metal implant, the photoelectric effect significantly attenuates the radiation

beam even at the higher end of the diagnostic energy range. These artifacts are called *metal artifacts* in CT. Figure 1.3 shows these artifacts in a kVCT image.

Generally, these artifacts can degrade the diagnostic information in the image and jeopardise the clinician's ability to correctly diagnose diseases, infections, and fractures, and to even assess the functionality of the implants themselves. The severity of metal artifacts in CT depends on the shape, size, composition and density of the metals. For example small screws and pins of titanium create less metal artifacts compared to those created by steel and bigger implants like hip prosthetics.⁶² Metal artifacts become more severe in case of multiple metal implants like bilateral hip prosthetics and multiple dental fillings.

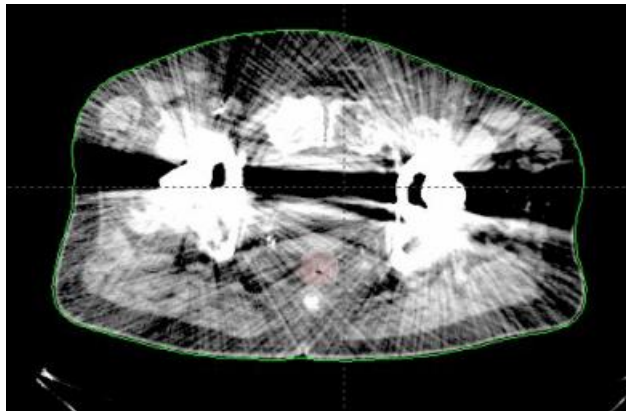


Figure 1.3. Diagnostic kVCT image of a patient reconstructed using FBP method showing the detrimental effects (streaking, shading etc.) of bilateral hip prosthetics.

In cancer patients, metal artifacts pose a problem in the proper diagnosis of tumours. In radiotherapy treatment planning, the delineation of organs at risk and the PTV becomes difficult in the presence of these artifacts. This might lead to missed tumour cells and/or more damage to healthy cells. If the electron density map obtained from a CT image is incorrect due to metal artifacts, the dose calculated using the degraded image can be erroneous.^{63,64} Often, treatment beams

are aimed to avoid the metals mainly because of the lack of correct CT numbers for the metal itself and the tissues in its shadow, which are vital for inhomogeneity correction factor calculation. This constraint often results in increased dose to organs at risk and may yield a poor treatment outcome. According to the American Association of Physicists in Medicine (AAPM) task group report # 63, 1%-4% of cancer patients' diagnosis/treatment can be adversely affected by the presence of metallic implants such as hip prosthetics, dental fillings and others.⁶⁴ Hip prosthetics and dental fillings affect the treatment of prostate and head & neck cancer patients respectively.

Computer simulations and experimental studies have suggested that a metal object can produce excessive beam hardening,⁶⁵ scatter dominated measurement,⁶⁶⁻⁶⁸ noise,^{69,70} partial volume effect,⁷¹⁻⁷⁴ photon starvation, aliasing, distinctly altered detector energy response in the shadow of an implant, and overflow of the dynamic range in the reconstruction process.⁶⁰ But, the most important causes of metal artifacts in kVCT are noise, photon starvation, beam hardening, partial volume effect, and scatter.⁶⁵ Diagnostic CT scanners use the fast and efficient filtered back projection (FBP) method for image reconstruction. However the aforementioned causes of artifacts severely violate linearity of the projection-backprojection operation inherently assumed in the FBP method, thereby leading to artifacts.

Below, the important factors that create metal artifacts are briefly described.

1.3.1 Beam hardening

When a polychromatic beam passes through a uniform object, low energy photons are preferentially absorbed compared to higher energy photons. The mean energy of the beam increases and the beam is more penetrating (lower attenuation coefficient). Therefore, the attenuation of the beam per unit path travelled through a cylindrical object changes from center (lower) to edge (higher) and creates a cupping appearance: *the cupping artifact*. The generally accepted beam hardening correction methods are based on a presumed body composition of either water or water-bone and they correct the non-linear behaviour of attenuation vs tissue thickness using calibration procedures designed under such assumptions. However, in the presence of the metals, the non-linear behaviour of attenuation profile as a function of thickness is significantly different from the bone-water like materials present in the calibration procedure. This is because the attenuation vs. photon energy is drastically different in metals compared to bone and water. This issue is further complicated due to the unknown size, shape and location of the metal. Any attempt to design a beam hardening calibration technique that includes presumed bone-water-metal composition is hampered by other non-linearities such as detector energy response and partial volume effect.⁶⁰ The general nature of metal-induced beam hardening artifacts is shading (i.e., lower attenuation coefficient value in the image) in the direction of higher attenuation, in addition to the cupping artifact.⁶⁵ The beam hardening is more severe for a kilovoltage (keV) spectrum compared to megavoltage (MeV) because the attenuation coefficient for all the materials has a much stronger energy

dependence in the keV range than in the MeV range. In most diagnostic scanners, the water or water-bone type of correction is automatically applied to the projection data for every patient. The response of the detectors changes with the energy of the incident photon. The general calibration assuming the presence of water or water-bone is therefore violated when the beam is hardened significantly due to the presence of metals. This mismatch can produce additional artifacts like bands, rings or additional shadings.

1.3.2 Noise and photon starvation

Noise in the image is inversely dependent upon the number of x-ray photons which reach and get measured at the detector. This is the characteristic quantum noise which comes from the statistics of photon production and interaction within the patient body and detectors, although it also encompasses the electronic noise of the detection system. In the presence of highly attenuating metallic objects, the signal output by the detector is very low approaching zero and the projection noise increases quickly and is further magnified by the derivative nature of the filtering step. The backprojection process maps these highly fluctuating signals to bright and dark lines in the image to form severe streaks. Also, the effects of beam hardening and scatter have been found to exacerbate the artifacts created by noise.⁶⁵ Multiple and thicker metals can nearly block the x-rays completely and create the condition of *photon starvation*. In such a situation the projection value can provide no information about the attenuating object in transmission tomography and an incorrect data is backprojected. This

results in an incorrect CT number being assigned to high density materials. A solid metallic prosthesis appears hollow due to photon starvation effect.⁶⁴

1.3.3 Scatter

In biological tissues, including water in the diagnostic energy range the majority of x-ray photons interact via Compton scattering. Compton scattered photons in the keV range have a very wide angular distribution and some of them can reach the detector even with a sophisticated collimation design.⁶⁶ The scattered photons make the detected signal deviate from the true transmission measurement and their contribution is similar to noise. In the shadow of metal, the scatter can dominate the measured transmission signal which causes significantly non-linear error in the projection data which is obtained after the logarithmic operation as defined in section (1.1) [In other words, Eq. (1.1) now becomes $I=I_0\exp(-\mu L)+S$, where S is a scatter contribution to the measured transmission signal. The measured projection data $\ln(I_0/I)$ now does not provide the true projection μL as expected from Eq. (1.1)]. The metal artifacts due to scatter are similar to those associated with beam hardening such as cupping and black shading in the direction of higher attenuation. In addition, white streaks bordering the dark shadings are also possible.⁶⁵⁻⁶⁸ Even a small contribution of scattered radiation can cause significant degradation of the image and it becomes worse in the presence of noise.⁶⁵

1.3.4 Partial volume effect

The finite size of the focal spot of an x-ray source and the width of real detectors make the beam profiles seen by each detector different from that for a pencil beam (theoretical x-ray beam with infinitesimal width). Thus the measured detector signal represents the attenuation of the incident beam by tissue present in this finite-sized beam instead of in a true pencil beam as assumed in the FBP method. The detector measures the transmitted beam averaged over its dimensions, both in the scanning plane and in the direction perpendicular to the scanning plane. For an image reconstruction in FBP method we obtain *projection data* from the measured transmission signal, using natural log (i.e., \ln), as discussed in section (1.1). In general, the total beam attenuation by the objects occupying a finite size beam cannot be estimated by taking the log of the total measured transmission signal if the beam attenuations along the cohort of ray-lines within the beam are significantly different from each other. Mathematically, if $I_0(t)$, and $I(t)$ represent incident and transmitted intensities for a ray in a beam of finite width (here 't' represents position of a ray along the width of the beam) then the measured attenuation for the finite size of the beam, which is proportional to $\ln(\sum I_0(t) / \sum I(t))$, is not in general equal to the actual attenuation that is proportional to $\sum \ln [I_0(t) / I(t)]$. This is simply due to the mathematical nature of log operation: *the log of sum of variables is not always equal to the sum of log of variables*. The resulting error is significantly large if a highly attenuating object such as a piece of metal partially intrudes into the scanning plane. Thus, for metals partially intruding into the beam, the log of total

transmission over the beam dimension has non-linear relationship with the true total attenuation. This, in addition to shifting of reconstructed pixels towards lower values, creates streaks and shadings in the image.^{71,72} This is called the partial volume effect. More mathematical explanations for CT number shift and streaking can be found elsewhere.^{71,72} In the axial partial volume effect (i.e., perpendicular to scanning plane or slice plane), the shading produced between the metallic objects in trans-axial image could be either bright or dark.⁷² In the trans-axial partial volume effect, the averaging occurs over the beam width in the slice plane. This partial volume effect is commonly termed the exponential edge gradient effect⁷³ or edge-induced streaking artifact⁷⁴ in the literature because it manifests as dark streaks tangent to sharp edges (sharp in terms of attenuation value). The black shading between multiple metallic objects also shows white streak-like borders. Also, black shadings can extend out of these objects in a perpendicular direction to the line joining the metals. Additional streaks originate in and extend out of metal objects.⁷²

1.3.5 Motion

Motion artifacts in CT are not limited to metallic objects only. However, because of the large inconsistencies in the projections due to the higher attenuation coefficient of metal, motion artifacts can be more severe.⁷⁵ The appearance (shape, extent etc) of motion artifacts changes with the type of motion. Black shadings with white streaks and blurring around metallic objects are common.⁶⁵

1.3.6 Aliasing

Aliasing artifacts in CT result from both detector and view (or radial and angular) undersampling. The appearances are quite common in the form of alternating bands of straight or circular streak patterns while scanning sharp objects. The detector undersampling creates the streaks originating from the sharp objects whereas in view undersampling streaks appear at some distance from the object.^{60,65} Though aliasing depends upon several other factors, it may be exacerbated due to the introduction of high density materials because of the sharp jump in the measured signal at the boundaries, which create higher spatial frequencies in the projection value spectrum.

1.3.7 Others

For reconstruction speed, digital signal processing (DSP) chips are often employed in the image reconstruction engine. When multiple highly attenuating metal implants are present in the scanned object the magnitude of *projection data* is so high that the dynamic range of the DSP chips can be exceeded after the filtering (i.e. derivative operator) step. As a result the filtered projection data are numerically ceiled and cause additional image artifacts.⁶⁰ Moreover, there is truncation of CT numbers at 4,096 Hounsfield units in the image produced by present day commercial CT scanners due to their 12-bit storage capacity. Most metallic implants are in the range of 3,000 to 60,000 Hounsfield Units for a typical kVCT beam but strongly depend on the mean beam energy. The cutoff of

very high CT values produces blurring and distortion of the contours of metallic implants on the images.⁷⁶ The electron density information obtained from the CT numbers of metallic objects in such an image is incorrect.

1.4 Metal artifact reduction (MAR) methods

1.4.1 Simple technical considerations

The range of CT numbers in CT images containing metal is very large. So the use of different window and level settings helps in viewing different tissue structures better. The use of an extended CT scale (> 12 bit) can reduce the visual blurring and distortion in the metal artifacts created from CT number truncation.⁷⁶ A change in imaging parameters such as higher peak voltage (e.g., 140 kVp instead of 120 kVp) or beam pre-filtering (i.e. pre-hardening) can help reduce beam hardening and increase the likelihood that photons will penetrate the metal.⁷⁷ However, there may be no improvement in case of bigger and denser metallic implants.⁷⁸ Photon starvation and the issue of noise could be addressed, although with marginal improvement, by using increased tube charge (mAs)⁷⁷ but this increases patient dose. The axial partial volume effect can be reduced using thinner slices. But, too thin a slice results in decreased signal to noise ratio (SNR). In multi row detector CT, several thin slices acquired together can be averaged to increase the SNR. But, the averaging should be done after taking the log operation [i.e., the averaging should be done in *projection data*, not in the *transmitted signal*].⁶⁰ The use of standard or smooth reconstruction filter may help reducing in metal artifacts.⁶²

At best, the above technical considerations can be optimized on a case by case basis but do not provide a workable solution for most clinical applications. So a systematic approach is needed to address the issue of metal artifacts. Various metal artifact reduction (MAR) techniques can be found in the literature but there are no commercially available techniques that can provide a systematic solution to metal artifacts in CT. Some of the published MAR techniques in literatures are reviewed here.

1.4.2 Correction methods with FBP image reconstruction

The MAR methods in this category assume that the metal artifacts arise due to missing or incorrect projection data; the gaps in the transmission sinogram arise from near complete attenuation of the x-ray photons passing through the metallic objects. The strategy of the method is to detect such missing projection data in the sinogram and then fill in the so-called ‘gaps’ with estimated projection data.

1.4.2a Image based correction methods

Image based correction methods segment the metal objects in FBP reconstructed images and create a synthetic sinogram of the metal-only image from knowledge of the CT scanner geometry. This synthetic sinogram is used to make a mask in the measured sinogram. That is why these methods are often called image-based correction methods. This is the **segmentation** step. Now the masked region needs to be filled by appropriate projection data for *lower*

attenuation material. Thus, information regarding the actual attenuation of the metal is sacrificed to gain visual clarity in the image. Usually the replacement is based on neighbouring projection samples that do not contain metal implants. This is the **interpolation** step.

Kalender *et al.*⁷⁹ and Klotz *et al.*⁸⁰ have suggested manual segmentation of metal parts in FBP images and a linear interpolation in each view to fill the gap. This method reduces the severe streak artifacts. This is because the projection data that does not support the linearity assumption of FBP is replaced by pseudo-data which also avoids the problems related to noise and scatter. The method in reference (79) is the first known metal artifact reduction technique temporarily implemented in a commercial scanner (in the Siemens SOMATOM from 1987 to 1990). Many correction methods use this method as a benchmark for comparison.^{63, 81-85}

There are some obvious difficulties in the implementation of these MAR methods. The forward projection of segmented metal regions into the projection space requires the knowledge of the proprietary scanner geometry. Bright streak artifacts in the image and poor contrast in the projection data pose a problem in accurate segmentation of metal objects. Some authors have used adaptive filtering in the segmentation step to smooth bright streaks in the image and reduce segmentation error.⁶⁹⁻⁸⁶ The masked region in the sinogram contains the information of other tissues present in the object which is lost via interpolation since neighbouring detector data in a single view usually contain no information regarding tissue that contributed to the detector data corrupted by metal. This can

introduce secondary artifacts into the corrected image or mislead radiologists by creating spurious structures.⁸² The diagnostically important soft tissue structures very close to large metallic objects can be totally lost.^{61, 81} Several interpolation schemes such as b-spline, cubic spline, polynomial, and wavelet transform have been tried but none of them perform correct and reliable interpolation.

Some authors⁸⁷ have used more unaffected projection data in a local 2D window centered on the missing projection and calculated the missing data as the sum of the weighted nearest unaffected projection values. The weights are based on the distances in the sinogram space. This method has been evaluated by radiologists⁶¹ in real patients with hip implants and orthopaedic hardware. It is found that the algorithm significantly reduces streaking and shading but introduces blurring and secondary shading artifacts which reduce the image quality. Yazdi *et al*⁶³ have used another interpolation scheme where for each projection edge in a view angle in the masked sinogram, the corresponding edge on the other side of the mask is found by simultaneously minimising the distance and difference in attenuation values respectively. The edges are then joined using linear interpolation. This approach helps reduce the destruction of projections from some of the structures that cross the mask and hence recovers the anatomical structures adjacent to the metal implant. This method, however, cannot guarantee correct interpolation when there are multiple tissues, metal objects and structures (heterogeneities) present in the image.

Bal and Spies⁸³ have introduced a novel approach of using *tissue class modelling*. Clustering in the adaptively filtered image is used to segment so-called

‘classes’ such as air, soft tissue, bone, and metal. The metallic region is then substituted by the CT number of surrounding material. The forward projection of this image gives a model sinogram. The metallic part of the model sinogram is then added in the masked sinogram and filtered-backprojected to get the final image. This method gives good results for low and moderate levels of metal artifacts but gives very inaccurate results due to incorrect tissue class modelling inherent in severe metal artifact regions, such as in the case of bilateral hip prostheses.

The effect of a MAR method in dose calculation has been evaluated by Bazalova *et al.*⁸⁸ using the EGSnrc/DOSXYZnrc Monte Carlo (MC) code. They used the method of Yazdi *et al.* but with cubic spline interpolation instead of linear. An extended calibration used to include metal in a MC dose calculation for phantoms showed great reduction (less than 2% from up to 25%) in dose calculation error when artifact corrected images were used. Patient dose volume histograms (DVHs) of a hypothetical target compared with DVHs for the original uncorrected images show significant differences and suggest the requirement of image correction if MC is used for dose calculation.

1.4.2b Projection space based correction methods

Methods have been investigated that are designed to segment metal objects directly from the sinogram space. The reduced contrast and superposition of various structures of an object in projection data make it more difficult to segment metallic regions directly in a sinogram. Hence a very few studies have

been made in this class of correction methods. A very sophisticated approach using image processing is required to segment the metallic region in a sinogram. Zhang *et al.*⁸⁹ in their work segment and mask metallic objects in 2D projection image of a cone beam CT volume at each view angle before interpolating from surrounding data. Likewise Yu *et al.*⁹⁰ segment metals in reformatted projections in a multi-slice helical CT data. The reformatted projection is formed by combining the projection data for all detector rows at the same view angle (every 2π radians apart) over the full longitudinal scan range after the pitch correction. Both the 2D projection image and the reformatted projection image* contain the whole metallic body which is segmented using intensity thresholding.

For the interpolation of data in a masked 2D projection image, Zhang *et al.* have used a variational method of solving the Laplace equation with Dirichlet boundary conditions to fill the masked region by the neighbourhood data. This method is often called the Laplacian diffusion method. However, Yu *et al.* used 2D interpolation based on a Delaunay triangulation⁹¹ of the data (using a MatLabTM [The MathWorks Inc., Natick, MA, USA] function) to accommodate the irregular shapes of the metal implants in reformatted projections.

Recently, direct segmentation of metallic regions in the sinogram has been introduced by Veldkamp *et al.*⁸⁴ They have used the Markov random field model (MRF) in combination with Bayesian statistical techniques to segment metal projections. Three interpolation schemes: linear similar to Kalender,⁷⁹ Laplacian

* A cone beam view or reformatted image is a 2D projection of the 3D image much like a radiographic x-ray image.

diffusion as used by Zhang,⁸⁹ and shortest distance interpolation of Yazdi⁶³ are used and the results are compared. Also a comparison has been made with the image-based segmentation method of Kalender *et al.*⁷⁹

Both the methods of Zhang and Yu were able to improve the soft tissue contrast near the metal objects. However, they can always introduce secondary artifacts. The results of Veldkamp were not significantly different from the image-based correction method of Kalender. This suggests the inherent difficulties of direct segmentation in the raw sinogram. These methods are faster compared to image-based correction methods because they do not require the forward projection of the metal-only region step necessary to make a mask for each view angle. Studies with clinical data using the Wilcoxon signed rank test in the pelvic region in the presence of a unilateral prosthesis have shown improved image quality for two of the methods.^{84,90} However, they will have limited performance and reliability for metal artifact correction similar to the image-based correction methods.

The effectiveness of the FBP-based artifact correction methods, as assessed by the visual quality of the image and the correctness of the CT numbers of the structures and metal objects in the image, largely depends upon the correctness of the segmentation and interpolation steps. These steps are very sensitive and error-prone when multiple dense metallic objects are present in the image. In such a case, even after correction, often the CT numbers corresponding to metal and structures in the shadow of metals exhibit large deviations from their true values because no information about the attenuating object is obtained at the

detectors due to photon starvation. So, the FBP based MAR methods that use a segmentation/interpolation scheme are not reliable and cannot give correct information about metal objects in kVCT images.

1.4.3 Model based correction methods

Model based methods assume that all the artifacts in CT including metal artifacts arise from discrepancies between the actual detector signal formation process and the model assumed by the reconstruction algorithm. We have listed almost all possible physical processes that contribute to metal artifacts in the previous section. Inclusion of some or all of these processes in the detector signal formation model can be expected to minimise or eliminate the metal artifacts.

In a very simplistic, discrete data acquisition model the expected detector signal (\hat{y}_i) in an i^{th} projection in transmission tomography can be expressed as,

$$\hat{y}_i = b_i \cdot \exp\left(-\sum_{j=1}^J l_{ij} \mu_j\right) \quad 1.3$$

where b_i is the detector signal in a blank scan (without an object in the beam path), l_{ij} is the effective intersection length of projection line i with image pixel j , and μ_j is the linear attenuation coefficient of the pixel intercepted by the line joining the detector and x-ray source. This equation assumes that the x-ray beam corresponding to each detector is a *pencil beam*, each pixel can be represented by a single attenuation coefficient (i.e., no beam hardening, meaning mono-energetic photons) and scatter radiation is not a part of the detector signal. Additionally, the measured detector signal is assumed to be free of noise. In reality, the measured detector signals y_i deviate from the expected values of the model due to statistical

fluctuations and the other physical processes mentioned above. Inverting the above equation for μ_j and solving the set of equations using a transform method results in the FBP method. In iterative methods (designed either to include a more realistic detector signal model or to solve for μ from a limited number of projections), the deviation of y_i from \hat{y}_i is taken into account, usually by using a statistical model that describes y_i as a function of \hat{y}_i (Poisson distribution). The reconstruction problem is solved in two steps. Firstly, an objective function is defined, and secondly, the objective function is optimized. This optimization step basically gives less weight to low count detector read-outs, making the algorithm inherently robust against other sources of artifacts that are most prominent in the directions of low counts (such as beam hardening, noise, scatter and partial volume effect). Many different objective functions such as minimum least square error, log-likelihood $[\sum_{i=1}^I (y_i \ln(\hat{y}_i) - \hat{y}_i)]$ etc., and different ways to optimize these objective functions exist. The optimization gives an iterative update scheme that starts from an initial image which is often uniform or a FBP image. The calculated sinogram from the initial image is compared to the measured sinogram. The sinogram difference is transferred back to the image domain and modifies the current reconstruction. The process is repeated a number of times until a good reconstruction is obtained.⁷²

Out of several iterative MAR methods⁹²⁻⁹⁷, alternative maximization (AM)⁹³ and maximum likelihood in transmission tomography (ML-TR)^{95,96} are of particular interest. These two methods can include models for a polychromatic

x-ray beam, scatter, and noise. In phantom studies, Williamson *et al*⁹⁴ have found that the AM algorithm dramatically improves the metal artifacts but, a few black and white streaks connecting high density metals still exist. Their complete removal is possible only if prior information of the attenuation map and the location of metal objects are known, which is impractical in the clinic.

In ML-TR algorithm log-likelihood is expanded in a truncated Taylor series and then optimised using a gradient descent approach where Eq. (1.3) is used for detector signal modeling (monochromatic). The reconstructed image using the ML-TR algorithm becomes coarser as the iteration number increases, in particular when the projection data are very noisy (which is the case in presence of metallic objects). Inclusion of a prior function (a probability distribution function that assumes a prior information about the image, i. e., it is a function of μ), commonly called the Gibb's prior,⁹⁸ modifies the objective function of ML-TR to give a maximum a posteriori (MAP) type algorithm. Phantom and simulation studies have suggested that the MAP algorithm reduces metal artifacts compared to ML-TR but significant streaks and black dots close to metal objects still remain in the image. ML-TR has been extended to the *iterative maximum likelihood polychromatic algorithm for CT* (IMPACT)⁹⁷ by incorporating a polychromatic x-ray beam model. A modified version of this algorithm is adapted for MVCT in this thesis and it is described in detail in the next chapter.

Out of several iterative MAR methods, the most practical algorithm is the IMPACT method⁹⁷ in which a clinically appropriate polychromatic x-ray beam model is used. IMPACT has been found to remove the beam hardening effect and

other artifacts caused by relatively less dense metals such as aluminum.⁹⁷ Titanium and steels are the most commonly found metals in hip prostheses. However, not all the metal artifacts are removed from CT images obtained using a 140 kVp beam when several denser metals like titanium and steels are present.⁹⁷ This is most probably due to photon starvation in the kVCT beam and the partial volume effect.

1.4.4 Mixed correction method

Iterative methods are more reliable, capable of including the physical processes into the model but are computationally extensive whereas FBP is very fast. Combining these two methods could be complementary to each other. One such a combination is suggested by Lemmens *et al.*⁹⁹ The method is called MAP-based projection completion (MAPPC). The algorithm creates an artifact-free constrained image using MAP and completes projections based on this constrained image. The final image can be reconstructed using completed projections (sinogram) and the FBP method.

The final results in a clinical setting for multiple dental fillings and bilateral hip prosthetics show improved results. This algorithm better restores the information close to the metals, at least in reported experiments. However, light shadings can still be observed in the images. Also, the use of heavy constraints in MAP to ensure no black spots around metal objects decreases both the spatial and contrast resolution in the final image. The algorithm does not assign the correct

CT number to metal. As the sinogram is corrected, this method also can fail to reconstruct proximal anatomy and introduce secondary artifacts.

1.5 Motivation and goals

The following points suggest the need for further research into the existing MAR methods:

1. The existing FBP based methods are not reliable since they can introduce secondary artifacts and spurious structures in the image. They can miss a part of the anatomical information of other tissues, usually close to the metal,^{81,82} in the process of removal of the information pertaining to metal objects in the image. They also lose information about the metal itself. If the information about the metal is restored from the uncorrected image, the CT number of the metal and its structure (shape, hollowness) is incorrect due to photon starvation.
2. The evaluation of FBP-based MAR methods⁸² for diagnostic purposes suggests that they are case specific and non-reliable. There is only one evaluation study⁸⁸ of a FBP method for radiotherapy dose calculation error and is done using the Monte Carlo method.
3. At the time of writing this thesis there exists only one commercial method available in the clinic, the *Orthopaedic metal artifact reduction (OMAR)* algorithm in the Phillips Big BoreTM kVCT scanner.¹⁰⁰ There are at least two studies published^{101,102} evaluating this algorithm for radiotherapy treatment planning. One of these studies¹⁰¹ is limited to the evaluation of IMRT plans where beams are constrained not to pass through the prostheses. The other

study¹⁰² evaluates the effect of bit depth change, from 12 to 16, as well as the effect of artifact correction on the radiotherapy dose distribution. This commercial method does not correct artifact inside metal objects. The effect of artifact correction inside metal and its impact in radiotherapy has not been fully explored. No other study has been published that evaluates the radiotherapy dose calculation accuracy of MAR techniques in commercial treatment planning systems that incorporate model based dose calculation methods such as those based on pencil beams and point-dose spread arrays or others such as superposition/convolution based methods.

4. Model based methods are reliable but require longer computation time and huge memory if most causes of metal artifacts are to be modelled. It is generally not easy to model all the causes except for beam hardening. These methods also suffer from the photon starvation effect and cannot provide complete removal of metal artifacts in kVCT.
5. To overcome the problem of photon starvation, one can use MVCT though it suffers from poor soft tissue contrast and limited spatial resolution. The megavoltage x-ray beam is more penetrating than a kilovoltage beam, so that the effects of beam hardening, noise, photon starvation and possibly scatter could be reduced. The lesser variation of the attenuation coefficient between metals and soft tissues in the higher energy range could help minimise the partial volume effect and aliasing.
6. Megavoltage CT has been used in the clinic for daily patient set up in image guided radiotherapy. Recent development of an MVCT scanner using better

detector design with increased detective quantum efficiency (DQE) leading to reduced patient dose can be promising for this purpose.¹⁹⁻²² This system, even without any corrections, suppresses metal artifacts dramatically and only leaves faint shadows connecting dense metals suggesting that beam hardening is the main contributor to the artifact. The use of model based methods like IMPACT for MVCT with faster implementation strategies could be practical for radiotherapy treatment planning purposes where imaging and treatment times are several hours apart.

7. There is not a single MAR method proposed that could potentially use information from both kVCT and MVCT. If this could be done then correct attenuation information from MVCT images and the better soft tissue contrast of kVCT images could be amalgamated, and the complementary benefits of these two modalities would make the algorithm robust and reliable.

In light of the motivations described above we set the following goals for the proposed research:

1. To reduce the metal induced artifacts in CT images and minimize secondary artifacts so that the tissue structures can be seen clearly and outlined correctly.
2. To reconstruct CT images where the CT numbers corresponding to metal and surrounding tissue are accurate so that the images can be used for accurate dose calculation in radiation therapy.
3. To evaluate the dose calculation accuracy in the artifact reduced image using commercial treatment planning systems.

To meet these goals we plan the following new studies.

1. At first we apply a model based correction method, such as an IMPACT, to MVCT images created by two different MVCT scanners. This requires necessary extension of the model to include pair/triplet production, and detector calibration for energy dependence. We evaluate the image improvement.
2. Then we use artifact corrected MVCT images with necessary MVCT number to electron density conversion to evaluate the correctness of the estimated electron density for a range of materials representing tissues found inside the human body.
3. We explore the possibility of using the model to represent the energy dependence of detectors in kVCT, as is done for MVCT in study number 1, and apply IMPACT to correct kVCT images. We evaluate this approach.
4. We use an artifact corrected MVCT image as a prior to correct a corresponding kVCT image. We evaluate the artifact corrected kVCT image for use in radiotherapy treatment planning and compare it with the commercial OMAR correction method. We use phantoms for this purpose.
5. Finally, for clinical patient images, we use an MVCT image as the prior image, as in study number 4, to correct a kVCT image and evaluate the corrected image.

From these studies it is expected to invent new correction strategies for metal artifact reduction in CT images, and explore the effect of these corrections in radiotherapy treatment planning together with the commercial correction method. The study of artifact correction in kVCT with an MVCT prior image is expected to give a significant contribution not only to radiotherapy but also to the general diagnostic imaging community by providing a better solution to metal artifact reduction in CT.

1.6 Outline of the thesis

The breakdown of chapters in this thesis is as follows. The IMPACT algorithm extended to MVCT (modified IMPACT) and the evaluation of the corrected images (study numbers 1 and 2) are presented in chapter 2. Tissue characterization phantoms are used with two MVCT systems: the commercial TomoTherapy Hi-Art IITM system, and an in house bench-top¹⁹⁻²² system. Chapter 3 (study number 3) explores the success/failure of extending the modified IMPACT algorithm to kVCT for metal artifact reduction. Chapter 4 consists of the phantom study (study number 4) with the strategy of using MVCT prior information in kVCT. Chapter five evaluates the correction scheme of chapter 4 in patient images. Finally, chapter six contains the summary of the thesis with conclusions and recommendations for future work.

1.7 References

- ^{1.} H. Barrett and W. Swindell, *Radiological Imaging: The Theory of Image formation, Detection and Processing*, (Academic Press, New York, 1981).

2. G.N. Ramachandran and A.V. Lakshminarayanan, "Three dimensional reconstructions from radiographs and electron micrographs: Application of convolution instead of fourier transforms," Proc. Natl. Acad. Sci., **68**, 2236-2240 (1971).
3. W. C. Roentgen, "Eine neue art con Strahlen. Sitzungs-berichte," Phys. Med. Ges. Wurzburg, **137**, 132-141 (1895). (English translation available: W. C. Roentgen, "On a new kind of rays," Nature, **53**, 274-276 (1896))
4. J. Radon, "Uber die bestimmung von funktionen durch ihre intergral-werte langs gewisser mannigfaltigkeiten," Ber. Sachs. Akad. Wiss., **69**, 262-277, 1917. (English translation available: J. Radon, "on the determination of functions from their integrals along certain manifolds," IEEE. Trans. Med. Imaging. **MI-5(4)**, 170-176 (1986))
5. G. N. Hounsfield, "Computerized transverse axial scanning (tomography): Part I. description of the system," Br. J. Radiol. **46**, 1016-1022 (1973).
6. A. M. Cormack, "Representation of a function by its line integrals, with some radiological applications," J. Appl. Phys. **34**, 2722-2729 (1963).
7. A. M. Cormack, "Representation of a function by its line integrals, with some radiological applications. II.," J. Appl. Phys. **35**, 2908-2913 (1964).
8. W. A. Kalender, *Computed Tomography: Fundamentals, System technology, Image quality, Applications*, (Publicis MCD Verlag, Inc., Munich, Germany, 2000).
9. H. E. Johns and J. R. Cunningham, *The Physics of Radiology*, 4th ed. (Charles C Thomas, Springfield, IL, 1983).
10. L. Schreiner, A. Kerr, G. Salomons, C. Dyck, and G. Hajdok, "The potential for image guided radiation therapy with Cobalt-60 tomotherapy," Proc. of 6th Annu. on Med. Imag. comput. and Comput.-Assist. Interven., Springer, Berlin/Heidelberg, 449-456, (2003).
11. T. Mackie, J. Balog, K. Ruchala, D. Shephard, S. Aldridge, E. Fitchard, P. Rechwerdt, G. Olivera, T. McNutt, and M. Mehta, "Tomotherapy," Semin. Radiat. Oncol. **1**, 108-117, (1999).

12. W. Swindell, R. G. Simpson, J. R. Oleson, E. A. Grubbs, and C. T. Chen “Computed tomography with a linear accelerator with radiotherapy applications,” *Med. Phys.* **10**, 416-420, (1983).
13. K. J. Ruchala, G. H. Olivera, E. A. Schloesser, and T. R. Mackie, “Megavoltage CT on a Tomotherapy system,” *Phys. Med. Biol.* **44**, 2597-2621 (1999).
14. M. A. Mosleh-Shirazi, P. M. Evans, W. Swindell, S. Webb, M. Partridge, “A cone-beam megavoltage CT scanner for treatment verification in conformal radiotherapy,” *Radiother. Oncol.* **48**, 319-328, (1998).
15. B. A. Groh, J. H. Siewerdsen, D. G. Drake, J. W. Wong, and D. A. Jaffray, “A performance comparison of flat –panel imager-based MV and kV cone-beam CT,” *Med. Phys.* **29**, 967-975, (2002).
16. E. C. Ford, J. Chang, K. Sidhu, D. Todor, G. Mageras, E. Yorke, C. C. Ling, H. Amols, and K. Mueller, “Cone-beam CT with megavoltage beams and an amorphous silicon electronic portal imaging device: potential for verification of radiotherapy of lung cancer,” *Med. Phys.* **29**, 2913-2924, (2002).
17. J. Sillanpaa, J. Chang, G. Mageras, C. C. Ling, H. Amols, H. Riem, E. Ford, and D. Todor, “Developments in megavoltage cone beam CT with an amorphous silicon EPID: reduction of exposure and synchronization with respiratory gating,” *Med. Phys.* **32**, 819-829, (2005).
18. H. Keller, M. Glass, R. Hinderer, K. Ruchala, R. Jeraj, G. Olivera, and T. R. Mackie, “Monte Carlo study of a highly efficient gas ionization detector for megavoltage imaging and image-guided radiotherapy,” *Med. Phys.* **29**, 165-175, (2002).
19. T. Monajemi, B. G. Fallone, S. Rathee, “Thick segmented CdWO₄ photodiode detector for Cone Beam CT: A Monte Carlo study of system design parameters,” *Med. Phys.* **33**, 4567-4577 (2006).
20. S. Rathee, D. Tu, T. Monajemi, D. Rickey and B. G. Fallone, "A bench-top megavoltage fan-beam CT using CdWO₄ -photodiode detectors: I. System

- description and detector characterization," *Med. Phys.* **33**, 1078-1089 (2006).
21. T. Monajemi, D. Tu, B. G. Fallone and S. Rathee, "A bench-top megavoltage fan-beam CT using CdWO₄-photodiode detectors: II. Image performance evaluation," *Med. Phys.* **33**, 1090-1100 (2006).
 22. P. Kirvan, T. Monajemi, B. G. Fallone, S. Rathee, "Performance Characterization of a MVCT Scanner using Multi-Slice Thick, Segmented Cadmium Tungstate-Photodiode Detectors," *Med. Phys.* **37**, 249-257 (2010).
 23. ICRU, "Prescribing, Recording and Reporting Photon Beam Therapy, Report 50," (1993).
 24. ICRU, "Prescribing, Recording and Reporting Photon Beam Therapy, Report 62," (1999).
 25. J. M. Balter and M. L. Kessler, "Imaging and alignment for image-guided radiation therapy," *J. Clin. Oncol.* **25**, 931-937 (2007).
 26. V. Gregoire, "Is there any future in radiotherapy planning without the use of PET: unravelling the myth," *Radiother. Oncol.* **73**, 261-263 (2004).
 27. S. L. Sailer, J. G. Rosenman, M. Soltys, T. J. Cullip, and J. Chen, "Improving treatment planning accuracy through multimodality imaging," *Int. J. Radiat. Oncol. Biol. Phys.* **35**, 117-124 (1996).
 28. D. Wang, C. J. Schultz, P. A. Jursinic, M. Bialkowski, X. R. Zhu, and W. D. Brown, "Initial experience of FDG-PET/CT guided IMRT of head and neck carcinoma," *Int. J. Radiat. Oncol. Biol. Phys.* **65**, 143-151 (2006).
 29. M. R. Sontag, J. J. Battista, M. J. Bronskill, and J. R. Cunningham, "Implications of computed tomography for inhomogeneity corrections in photon beam dose calculations," *Radiol.* **124**, 143-149 (1977).
 30. T. R. Mackie, E. El-Khatib, J. J. Battista, J. W. Scrimger, J. Van Dyk, and J. R. Cunningham, "Lung dose corrections for 6 MV and 15 MV x-rays," *Med. Phys.* **12**, 327-332 (1985).
 31. M. G. Herman, J. M. Balter, D. A. Jaffray, K. P. McGee, P. Munro, S. Shalev, M. Van Herk, and J. W. Wong, "Clinical use of electronic portal

- imaging: report of AAPM radiation therapy committee Task Group 58,” *Med. Phys.* **28**, 712-737 (2001).
32. W. De Neve, F. Van den Heuvel, M. De Beukeleer, M. Coghe, L. Thon, P. De Roover, M. Van Lancker, and G. Storme, “Routine clinical on-line portal imaging followed by immediate field adjustment using a tele-controlled patient couch,” *Radiother. Oncol.* **24**, 45-54 (1992).
 33. A. L. Boyer, L. Antonuk, A. Fenster, M. Van Herk, H. Meertens, P. Munro, L. E. Reinstein, and J. Wong, “A review of electronic portal imaging devices (EPIDs),” *Med. Phys.* **19**, 1-16 (1992).
 34. J. Bijhold, K. G. Gilhuijs, and M. Van Herk, “Automatic verification of radiation field shape using digital portal images,” *Med. Phys.* **19**, 1007-1014 (1992).
 35. H. Wang, and B. G. Fallone, “A robust morphological algorithm for automatic radiation field extraction and correlation of portal images,” *Med. Phys.* **21**, 237-244 (1994).
 36. M. K. Woo, A. W. Lightstone, G. Shan, L. Kumaraswamy, and Y. Li, “Automatic verification of step and shoot IMRT field segments using portal imaging,” *Med. Phys.* **30**, 348-351 (2003).
 37. M. van Zijtveld, M. L. Dirkx, H. C. de Boer, and B. J. Heijmen, “Dosimetric pre-treatment verification of IMRT using EPID; clinical experience,” *Radiother. Oncol.* **81**, 168-175 (2006).
 38. M. Uematsu, T. Fukui, A. Shioda, H. Tokumitsu, K. Takai, T. Kojima, Y. Asai, and S. Kusano, “A dual computed tomography linear accelerator unit for stereotactic radiation therapy: a new approach without cranially fixed stereotactic frames,” *Int. J. Radiat. Oncol. Bio. Phys.* **35**, 587-592 (1996).
 39. J. R. Wong, C. W. Cheng, L. Grimm, and M. Uematsu, “Clinical implementation of the world’s first primatom, a combination of CT scanner and linear accelerator, for precise tumour targeting and treatment,” *Med. Phys.* **17**, 271-276 (2001).
 40. S. L. Meeks, J. F. Harmon Jr, K. M. Langen, T. R. Willoughby, T. H. Wagner, and P. A. Kupelian, “Performance characterization of megavoltage

- computed tomography imaging on a helical Tomotherapy unit,” *Med. Phys.* **32**, 2673-2681 (2005).
41. T. R. Mackie, H. Jaradat, S. Hui, J. Balog, D. M. Vail, and M. P. Mehta, “The utility of megavoltage computed tomography images from a helical tomotherapy system for setup verification purposes,” *Int. J. Radiat. Oncol. Biol. Phys.* **60**, 1639-1644 (2004).
 42. P. A. Kupelian, S. L. Meeks, T. R. Willoughby, A. Forbes, T. H. Wagner, and K. M. Langen, “Serial megavoltage CT imaging during external beam radiotherapy for non-small-cell lung cancer: observations on tumour regression during treatment,” *Int. J. Radiat. Oncol. Biol. Phys.* **63**, 1024-11028 (2005).
 43. K. M. Langen, S. L. Meeks, D. O. Poole, T. H. Wagner, T. R. Willoughby, P. A. Kupelian, K. J. Ruchala, J. Haimerl, and G. H. Olivera, “The use of megavoltage CT (MVCT) images for dose recomputations,” *Phys. Med. Biol.* **50**, 4259-4276 (2006).
 44. I. A. Feldkamp, L. C. Davis, and J. W. Kress, “Practical cone-beam algorithm,” *J. Opt. Soc. Am. A.* **1**, 612-619 (1984).
 45. F. M. Khan, *Treatment planning in radiation oncology*, 2nd ed. (Lippincott Williams & Wilkins, Inc., Pennsylvania, USA, 2007).
 46. O. Morin, A. Gillis, J. Chen, M. Aubin, K. Bucci, M. Roach, and J. Pouliot, “Megavoltage cone-beam CT: System description and clinical applications,” *Med. Dosim.* **31**, 51-61 (2006).
 47. D. A. Jaffray, and J. H. Siewerdsen, “Cone-beam computed tomography with a flat panel imager: initial performance characterization,” *Med. Phys.* **27**, 1311-1323 (2000).
 48. D. A. Jaffray, J. H. Siewerdsen, J. W. Wong, and A. A. Martinez, “Flat panel cone-beam computed tomography for image-guided radiation therapy,” *Int. J. Radiat. Oncol. Biol. Phys.* **53**, 1337-1349 (2002).
 49. J. H. Siewerdsen, M. J. Daly, B. Bakhtiar, D. J. Moseley, S. Richard, H. Keller, and D. A. Jaffray, “A simple, direct method for x-ray scatter

- estimation and correction in digital radiography and cone-beam CT,” *Med. Phys.* **33**, 187-197 (2006).
50. M. B. Sharpe, T. Craig, and D. J. Moseley, “Image guidance: Treatment target localization systems,” in *IMRT, IGRT, SBRT: Advances in the treatment planning and delivery of radiotherapy*, edited by J. L. Meyer (Karger, Basel, Switzerland, 2007), pp. 72-93.
51. K. M. Langen, J. Pouliot, C. Anezinos, M. Aubin, A. R. Gottschalk, I. C. Hsu, D. Lowther, Y. M. Liu, K. Shinohara, L. J. Verhey, V. Weinberg, and M. Roach, “Evaluation of ultrasound-based prostate localization for image-guided radiotherapy,” *Int. J. Radiat. Oncol. Biol. Phys.* **57**, 635-644 (2003).
52. X. Artignan, M. H. P. Smitsmans, J. V. Lebesque, D. A. Jaffray, M. van Herk, and H. Bartelink, “Online ultrasound image guidance for radiotherapy of prostate cancer: impact of image acquisition on prostate displacement,” *Int. J. Radiat. Oncol. Biol. Phys.* **59**, 595-601 (2004).
53. P. G. Seiler, H. Blattmann, S. Kirsch, R. K. Muench, and C. Schilling, “A novel tracking technique for the continuous precise measurement of tumour positions in conformal radiotherapy,” *Phys. Med. Biol.* **45**, N103-N110 (2000).
54. S. L. Meeks, W. A. Tome, T. R. Willoughby, P. A. Kupelian, T. H. Wagner, J. M. Buatti, and F. J. Bova, “Optically guided patient positioning techniques,” *Semin. Radiat. Oncol.* **15**, 192-201 (2005).
55. B. G. Fallone, B. Murray, S. Rathee, T. Stanescu, S. Steciw, S. Vidakovic, E. Blosser, and D. Tymofichuk, “First MR images obtained during megavoltage photon irradiation from a prototype integrated linac-MR system,” *Med. Phys.* **36**, 2084-2088 (2009).
56. B. R. Whitting, K. T. Bae, and M. W. Skinner, “Cochlear implants: three dimensional localization by means of co-registration of CT and conventional radiographs,” *Radiol.* **221**, 543-549 (2001).
57. L. M. White, K. A. Buckwalter, “Technical considerations: CT and MR imaging in the postoperative orthopaedic patient,” *Musculoskelet. Radiol.* **6**, 5-17 (2002).

58. K. A. Buckwalter, J. A. Parr, R. H. Choplin, and W. N. Capello, "Multichannel CT imaging of orthopaedic hardware and implants," *Semin. Musculoskelet. Radiol.* **10**, 86-97 (2006).
59. S. Achenbach, "Computed tomography coronary angiography," *J. Am. Coll. Cardiol.*, **48**, 1919-1928 (2006).
60. J. Hsieh, *Computed Tomography: principles, design, artifacts, and recent advances*, 2nd ed. (SPIE Inc. and Wiley-Interscience Inc., USA, 2009).
61. P. T. Liu, W. P. Pavlicek, M. B. Peter, M. J. Spangehl, C. C. Roberts, and, R. G. Paden, "Metal artifact reduction image reconstruction algorithm for CT of implanted metal orthopaedic devices: a work in progress," *Skelet. Radiol.* **38**, 797-802 (2009).
62. M. J. Lee, S. Kim, S. A. Lee, H. T. Song, Y. M. Huh, D. H. Kim, S. H. Han, J. S. Suh, "Overcoming artifacts from metallic orthopaedic implants at high field strength MR imaging and multidetector CT," *Radiographics* **27**, 791-803(2007).
63. M. Yazdi, L. Gingras, and L. Beaulieu, "An adaptive approach to metal artifact reduction in helical computed tomography for radiation therapy treatment planning: experimental and clinical studies," *Int. J. Radiat. Oncol. Biol. Phys.* **62**, 1224-1231 (2005).
64. C. Reft, R. Alecu, I. Das, B Gerbi, P. Keall, E. Lief, B. Mijnheer, N. Papanikolaou, C. Sibata, and J. Van Dyk, "Dosimetric considerations for patients with hip prostheses undergoing pelvic irradiation. Report of the American Association of Physicists in Medicine radiation therapy committee task group 63," *Med. Phys.* **30**, 1162-1182 (2003).
65. B. De Man, J. Nuyts, P. Dupont, G. Marchal, and P. Suetens, "Metal streak artifacts in X-ray computed tomography: A simulation study," *IEEE Trans. Nucl. Sci.* **46**, 691-696 (1999).
66. G. H. Glover, "Compton scatter effects in CT reconstructions," *Med. Phys.* **9**, 860-867 (1982).

67. J. H. Siewerdsen and D. A. Jaffray, "Cone-beam computed tomography with a flat-panel imager: magnitude and effects of x-ray scatter," *Med. Phys.* **28**, 220-231 (2001).
68. M. Endo, T. Tsunoo, N. Nakamori, and K. Yoshida, "Effect of scattered radiation on image noise in cone beam CT," *Med. Phys.* **28**, 469-474 (2001).
69. J. Hsieh, "Adaptive streak artifact reduction in computed tomography resulting from excessive x-ray photon noise," *Med. Phys.* **25**, 2139-2147 (1998).
70. M. Kachelriess, O. Watzke, W. A. Kalender "Generalized multidimensional adaptive filtering for conventional and spiral single-slice, multi-slice, and cone-beam CT," *Med. Phys.* **28**, 475-490 (2001).
71. G. H. Glover and N. J. Pelc, "Nonlinear partial volume artifacts in x-ray computed tomography," *Med. Phys.* **7**, 238-248 (1980).
72. B. De Man, "Iterative reconstruction for reduction of metal artifacts in computed tomography," Ph.D. dissertation, Katholieke University of Leuven, Leuven, Belgium (2001).
73. P. M. Joseph and R. D. Spital, "The exponential edge-gradient effect in x-ray computed tomography," *Phys. Med. Biol.* **26**, 473-487 (1981).
74. W. T. Sheridan, M. R. Keller, C. M. O'Connor, and R. A. Brooks, "Evaluation of edge-induced streaking artifacts in CT scanners," *Med. Phys.* **7**(2), 108-111 (1980).
75. G. H. Glover and N. J. Pelc, "An algorithm for the reduction of metal clip artifacts in CT reconstructions," *Med. Phys.* **8**, 799-807 (1981).
76. T. M. Link, W. Berning, S. Scherf, U. Joosten, A. Joist, K. Engelke, and H. E. Daldrup-Link, "CT of metal implants: reduction of artifacts using an extended CT scale technique," *J. Comput. Assist. Tomogr.* **24**, 165-172 (2000).
77. J. F. Barret and N. Keat, "Artifacts in CT: recognition and avoidance," *Radiographics* **24**, 1679-1691 (2004).
78. N. Haramati, R. B. Staron, K. Mazel-Sperling, K. Freeman, E. L. Nicoloff, C. Barax, and F. Feldman, "CT scans through metal scanning technique

- versus hardware composition,” *Comput. Med. Imaging. Graph.* **18**, 429-434 (1994).
79. W. A. Kalender, R. Hebel, and J. A. Ebersberger, “Reduction of CT artifacts caused by metallic implants,” *Radiology* **164**, 576-577 (1987).
 80. E. Klotz, W. A. Kalender, R. Sokiranski, and D. Felsenberg, “Algorithm for reduction of CT artifacts caused by metallic implants,” *SPIE Med. Imaging IV* **1234**, 642-650 (1990).
 81. J. Rinkel, W. P. Dillon, T. Funk, R. Gould, and S. Prevrhal, “Computed tomographic metal artifact reduction for the detection and quantification of small features near large metallic implants: A comparison of published methods,” *J. Comput. Tomogr.* **32**, 621-629 (2008).
 82. J. Muller and T. M. Buzug, “Spurious structures created by interpolation based CT metal artifact reduction,” *Proc. SPIE Med. Imag.* **7258**, 1Y1-1Y8 (2009).
 83. M. Bal and L. Spies, “Metal artifact reduction in CT using tissue-class modelling and adaptive prefiltering,” *Med. Phys.* **33**, 2852-2859 (2006).
 84. W. Veldkamp, R. Joemai, A. Molen, and J. Geleijns, “Development and validation of segmentation and interpolation techniques in sinograms for metal artifact suppression in CT,” *Med. Phys.* **37**, 620-628 (2010).
 85. X. Pan, “Optimal noise control in and fast reconstruction of fan-beam computed tomography image,” *Med. Phys.* **26**, 689-697 (1999).
 86. O. Watzke, and W. A. Kalender “A pragmatic approach to metal artifact reduction in CT:merging of metal artifact reduced images,” *Eur. Radiol.* **14**, 849-856 (2004).
 87. A. H. Mahnken, R. Raupach, J. E. Wildberger, B. Jung, N. Heussen, T. G. Flohr, R. W. Gunther, and S. Schaller “A new algorithm for metal artifact reduction in computed tomography: In vitro and in vivo evaluation after total hip replacement,” *Invest. Radiol.* **38**, 769-775 (2003).
 88. M. Bazalova, L. Beaulieu, S. Palefsky, and F. Verhaegen, “Correction of CT artifacts and its influence on Monte Carlo dose calculations,” *Med. Phys.* **34**, 2119-2132 (2007).

89. Y. Zhang, L. Zhang, X. R. Zhu, A. K. Lee, M. Chambers, and L. Dong, "Reducing metal artifacts in cone beam CT images by pre-processing projection data," *Int. J. Radiat. Oncol. Biol. Phys.* **67**, 924-932 (2007).
90. L Yu, H. Li, J. Mueller, J. M. Kofler, X. Liu, A. N. Primak, J. G. Fletcher, L. S. Guimaraes, T. Macedo, and C. H. McCollough, "Metal artifact reduction from reformatted projections for hip prostheses in multislice helical computed tomography: techniques and initial results," *Invest. Radiol.* **44**, 691-696 (2009).
91. D. T. Lee and B. J. Schachter, "Two algorithms for constructing a Delaunay Triangulation," *Int. J. Comput. Info. Sci.* **9**, 219-242 (1980).
92. D. L. Snyder, J. A. O'Sullivan, B. R. Whiting, R. J. Murphy, J. Benac, J. A. Cataldo, D. G. Politte, and J. F. Williamson, "Deblurring subject to non-negativity constraints when known functions are present with application to object-constrained computerized tomography," *IEEE. Trans. Med. Imaging.* **20**, 1009-1017 (2001).
93. J. A. O'Sullivan, and J. Benac, "Alternating minimization algorithms for transmission tomography," *IEEE Trans Med. Imag.* **26**, 283-297 (2007).
94. J. F. Williamson, B. R. Whiting, J. Benac, R. J. Murphy, G. J. Blaine, J. A. O'Sullivan, D. G. Politte, and D. L. Snyder, "Prospects for quantitative computed tomography imaging in the presence of foreign metal bodies using statistical image reconstruction," *Med. Phys.* **29**, 2404-2418 (2002).
95. B. De Man, J. Nuyts, P. Dupont, G. Marchal, and P. Suetens, "Reduction of metal streak artifacts in x-ray computed tomography using transmission maximum a posteriori algorithm," *IEEE Trans. Nucl. Sci.* **47**, 977-981 (2000).
96. K. Lange, and R. Carson, "EM reconstruction algorithms for emission and transmission tomography," *J. Compt. Assist. Tomogr.* **8**, 306-316 (1984).
97. B. De Man, J. Nuyts, P. Dupont, G. Marchal, and P. Suetens, "An iterative maximum-likelihood polychromatic algorithm for CT," *IEEE Trans. Med. Imaging.* **20**, 999-1008 (2001).

- ⁹⁸. E. U. Mumcuoglu, R. M. Leahy, and S. R. Cherry, “Bayesian reconstruction of PET images: methodology and performance analysis,” *Phys. Med. Biol.* **41**, 1777-1807 (1996).
- ⁹⁹. C. Lemmens, D. Faul, and J. Nuyts, “Suppression of metal artifacts in CT using a reconstruction procedure that combines MAP and projection completion,” *IEEE Trans. Med. Imaging.* **28**, 250-260 (2009).
- ¹⁰⁰. Metal Artifact Reduction for Orthopedic Implants (O-MAR). Philips HealthCare System 2012 [available URL: [http://clinical.netforum.healthcare.philips.com/us_en/Explore/White-Papers/CT/Metal-Artifact-Reduction-for-Orthopedic-Implants-\(O-MAR\)](http://clinical.netforum.healthcare.philips.com/us_en/Explore/White-Papers/CT/Metal-Artifact-Reduction-for-Orthopedic-Implants-(O-MAR))].
- ¹⁰¹. H. Li, C. Noel, H. Chen, H. Harold, D. Low, K. Moore, P. Klahr, J. Michalski, H. A. Gay, W. Thorstad, and S. Mutic, “Clinical evaluation of a commercial orthopedic metal artifact reduction tool for CT simulations in radiation therapy,” *Med. Phys.* **39**, 7507-7517 (2012).
- ¹⁰². C. Glide-Hurst, D. Chen, H. Zhong, and I. J. Chetty, “Changes realized from extended bit-depth and metal artifact reduction in CT,” *Med. Phys.* **40**, 061711 (2013).

CHAPTER 2 : Metal artifact reduction in MVCT using a modified IMPACT

A version of this chapter has been published: M. R. Paudel, M. Mackenzie, B. G. Fallone, and S. Rathee, "Evaluation of metal artifacts in MVCT systems using a model based correction method," Med. Phys. 39, 6297-6308 (2012).

2.1 Introduction

The x-ray tubes in diagnostic CT scanners produce a polychromatic beam in the range of 30 keV - 140 keV. Numerous metal artifact reduction (MAR) techniques^{1,2,3,4,5,6,7,8,9} have been proposed and used in diagnostic kilovoltage CT (kVCT) imaging, either in phantom or clinical studies. Most of these methods sacrifice the quantitative accuracy in CT numbers of both the metal implant and the tissue in the shadow of the artifact in favor of minimizing the visual effects of the artifacts. Although model based iterative methods show great promise, they require prior information of the location and composition of the metallic regions⁹ in addition to longer computing times. Among the model based methods, the iterative maximum-likelihood polychromatic (IMPACT) algorithm has been remarkably successful⁸ in reducing artifacts in kVCT images, which include a lightly attenuating metal like aluminum. However, the algorithm failed to completely remove the artifacts created by iron. This suggests that the photon starvation effect may prevent the beam hardening model of the algorithm from working properly. The most important causes of metal artifacts in kVCT are noise (and, related to this, photon starvation at the detector), beam hardening, partial volume effects and increased scattering.^{1,9}

Megavoltage CT (MVCT) has promising benefits over kVCT regarding these factors due to reduced photon starvation, and reduced beam hardening issues due to a smaller difference in attenuation coefficients between metal and other tissues at MV energies. However there are still significant metal artifacts in MVCT images that are likely to be enhanced in future MVCT systems, which are designed to utilize a lower energy photon spectrum generated by a lower atomic number target (i.e. not tungsten; carbon, for example).¹⁰ The aim of this study is to apply the IMPACT algorithm to reduce metal artifacts in two MVCT systems: our optimized in house, bench-top MVCT system and the commercial TomoTherapyTM Hi Art-II [TomoTherapy Inc., Madison, WI, USA] MVCT system. The IMPACT algorithm is modified to include pair/triplet production and the modeled energy dependent response of individual detectors. A metal artifact corrected MVCT image can either be used directly for treatment planning^{11,12} or to serve as a good initial image for further development in metal artifact reduction in a kVCT image.

2.2 Methods and Materials

2.2.1 IMPACT modifications for MVCT

The IMPACT algorithm⁸ considers the polychromatic nature of the x-ray beam and expects the detector signal, \hat{y}_i , normalized to air scan, in view i to be

$$\hat{y}_i = \sum_{k=1}^K b_{ik} \cdot \exp\left(-\sum_{j=1}^J l_{ij} \mu_{jk}\right) \quad 2.1$$

Here k represents the index of photon energy bin in the discretized imaging beam spectrum, and j represents image pixel index. The coefficient b_{ik} is the x-ray

beam's energy fluence spectrum. Also, l_{ij} is the length of intersection of i^{th} ray with j^{th} pixel, and μ_{jk} represents the linear attenuation coefficient of the j^{th} pixel for the k^{th} photon energy. This model of signal formation only assumes polychromatic pencil beam and does not include other possible factors, if any, such as scatter, energy response of the detectors, partial volume e.t.c. Unlike the FBP method, which casts μ as a function of spatial coordinates alone, the model in Eq. (2.1) introduces the spectral energy as an additional dimension. Reconstruction of μ as a function of space as well as energy is not feasible with currently used energy integrating type of detectors in CT. In an attempt to reduce the dimensionality of the problem, a crucial step of the IMPACT algorithm is the formulation of a realistic model for the energy dependence of μ_{jk} .

Compton and photoelectric processes are the two main modes of interaction in human tissues for the diagnostic (kV) energy range. The energy dependencies of these processes are well known and the values of the attenuation coefficients for a variety of elements, compounds and mixtures are well documented.¹³ The pair/triplet production processes are important interactions in the MV energy ranges, especially in high Z materials like metals. For example, for 3 MeV photons in iron, the portion of the linear attenuation coefficient due to pair/triplet interaction is about 12% of the portion due to the Compton interaction.¹³ Using our knowledge of the x-ray source beam spectrum, this method models the energy dependence of linear attenuation coefficient $\mu(E)$ using a few basic substances such as air, water, bone and metal. Mathematically, this formulation is expressed as:

$$\mu(E) = \phi \cdot \Phi(E) + \theta \cdot \Theta(E) + \tau \cdot \Gamma(E), \quad 2.2$$

$$\Phi(E) = E_0^3 / E^3, \quad \Theta(E) = f_{kn}(E) / f_{kn}(E_0), \quad \Gamma = \sum_{i=0}^3 (\ln(1 + 2\alpha) / \ln(1 + 2\alpha_0))^i, \quad 2.3$$

$$\alpha = E(\text{MeV}) / 0.511, \quad \alpha_0 = E_0(\text{MeV}) / 0.511$$

Here, $f_{kn}(E)$ is the Klein-Nishina function,⁸ and Γ ¹⁴ includes both pair and triplet productions for the megavoltage energies in the MVCT imaging beams. This latter part is not included in the original IMPACT algorithm, which was formulated for kilovoltage energy. Theoretically, Eq. (2.2) and Eq. (2.3) show that the coefficients ϕ , θ , τ refer to photoelectric, Compton, and pair/triplet production parts of the total attenuation coefficient at the reference energy (E_0) respectively. Practically, for each base substance (air, water, bone and metal), the known¹³ linear attenuation coefficients at the discrete energy points (E) in the imaging beam spectrum and at a reference energy E_0 (e. g. 1.25 MeV) are used in Eq. (2.2), which is subjected to a least square fit to get the values for ϕ , θ , τ .⁸ The reference energy E_0 is any energy close to the mean energy of the imaging beam spectrum.

The energy dependent attenuation of any other material can be determined from Eq. (2.2) if the corresponding coefficients (ϕ , θ , τ) are known. These coefficients, for the unknown μ_j in the image, are now assumed to be functions of the linear attenuation coefficient $\mu(E_0)$ of base substances at energy E_0 . The corresponding values of (ϕ , θ , τ), for a pixel with estimated attenuation μ_j at the reference energy, are calculated in each iteration step by using linear interpolation between the basis materials. The energy dependent attenuation of the unknown

pixels, $\mu(E)$, is then calculated from the estimated (ϕ, θ, τ) using Eq. (2.2), and then substituted in to Eq. (2.1) to give an estimate of the detector signal \hat{y}_i . The difference between the measured (y_i) and the estimated detector signal at each iteration step is thus passed to the update step of the algorithm to provide the next estimate of the image ($\bar{\mu}_j$). Briefly, the update step of the algorithm is obtained as follows. The log-likelihood function $L = \sum_{i=1}^I (y_i \cdot \ln(\hat{y}_i) - \hat{y}_i)$ is maximized to obtain the image ($\bar{\mu}_j$), where the measured data, y_i , is assumed to be a Poisson realization of \hat{y}_i . In the practical implementation, the log-likelihood function is expanded in a truncated Taylor series and optimized using gradient descent method to get the update step in the IMPACT algorithm.⁸ The x-ray beam path lengths (l_{ij}) in Eq. (2.1) are pre-calculated using Siddon's algorithm¹⁵ for the geometry of each system. Using the updated estimate of the image μ_j , the new estimation of parameters (ϕ, θ, τ) is made and the iteration continues until a satisfactory final image is produced. Thus the final image represents the attenuation coefficient map at the pre-defined energy E_0 , usually the mean energy of the spectrum.

Although the energy dependent detector calibration factor is mentioned in the theoretical formulation of the original IMPACT paper, it appears that b_{ik} were approximated by the photon fluence spectrum ignoring the energy dependent response of the detectors. In the presence of multiple metal implants there can be significant beam hardening. The strong energy dependency of the detectors, if it exists, can alter the measured detector signal quite significantly. We have

included this energy dependent factor (a_{ik}) into the model and therefore express Eq. (2.1) in the form:

$$\hat{y}_i = \sum_{k=1}^K a_{ik} b_{ik} \cdot \exp\left(-\sum_{j=1}^J l_{ij} \mu_{jk}\right) \quad 2.4$$

Here, b_{ik} now represents the photon fluence spectrum instead of the energy fluence spectrum in Eq. (2.1). The factors (a_{ik}) represent the relative signal of the detector measuring the i^{th} view for the k^{th} energy bin per unit fluence in the k^{th} energy bin. The rationale behind using this factor is our hypothesis that CT detectors can have strong energy dependent gain, which is further justified in section (2.3.1). The signal formation model in Eq. (2.4) also assumes polychromatic pencil beam and adds the energy response of detectors as an extra model compared to the model in Eq. (2.1). Scatter as a model is not included in the calculation of a_{ik} and if there be any that will add an error in the estimated a_{ik} .

2.2.2 Bench-top MVCT

Our optimized bench-top MVCT system and the data acquisition technique have been described in a previous publication.¹⁶ Briefly, the detector system contains 16 rows each with 320 individual CdWO_4 crystals attached to photodiodes with a detector pitch of 1 mm in both dimensions. A 19.1 cm diameter, cylindrical plexiglass phantom containing two cylindrical steel rods of 2.7 cm diameter at the periphery, along with ten other peripheral inserts of physical density in the range 0.65 g/cc - 2.18 g/cc, was used in these experiments. At the center of the phantom, cylindrical inserts of variable electron density were scanned one at a time. The central inserts [Tissue Characterization Phantom,

Gammex Inc., Middleton, WI, USA] have nominal electron density ranging from 0.295 - 1.695, relative to water. The bench-top MVCT used the bremsstrahlung radiation of a 6 MeV electron beam, generated by filtering the electrons through a 4 cm thick solid water slab. The field size used in these experiments was 29 cm x 2 cm at 100 cm from the source, chosen to irradiate all 16 detector rows to a uniform noise level. These experiments were conducted on a Varian Clinac 2300 C [Varian Medical Systems Inc., Palo Alto, CA, USA] using the total skin electron irradiation applicator setting in the service mode with the accessory interlock overridden. The sinograms of 5 detector rows (3 - 7), each containing 320 detectors, were normalized to the corresponding air scan data and then averaged to obtain the raw fan beam sinogram with 2790 views per rotation. Furthermore, the sinogram data were averaged over five rotations. Since the dose per pulse in the imaging beam is very small, these steps are needed to ensure that the noise level and the effective slice thickness in bench-top MVCT images are similar to that in the TomoTherapy™ case.

A traditional 256x256 image was reconstructed using the filtered backprojection (FBP) method within MatLab™ [The MathWorks Inc., Natick, MA, USA] environment. The sinogram was first converted from the fan-beam to the parallel beam geometry using the ‘fan2para’ function. The inverse Radon Transform, with Ram-Lak filter and linear interpolation (MatLab™ function ‘iradon’), was used to reconstruct images from the parallel beam sinogram after applying a beam hardening and detector calibration correction. For the calibration factors, the experimental raw parallel beam sinogram of a larger (20 cm diameter),

uniform plexiglass phantom was averaged over all 2790 views and normalized among the pseudo parallel rays to unity. The corresponding averaged and normalized sinogram of the same size mathematical phantom (using function 'phantom') of unit pixel value was obtained using the Radon transformation (using function 'radon'). The calibration factors were obtained by dividing the mathematical sinogram by the experimental sinogram for each pseudo parallel ray. These factors were multiplied with the raw parallel beam sinogram data of the phantom to obtain the beam hardening and the detector calibration corrections.

The phantom without the steel inserts was scanned and similarly processed to obtain the calibration of attenuation coefficients vs electron density, which is unaffected by any metal artifacts.

The model based image is reconstructed using the modified IMPACT algorithm described in section (2.2.1). The previously benchmarked¹⁶ photon spectrum, calculated using the BEAMnrc¹⁷ and BEAMdp¹⁸ Monte Carlo codes, was divided into 20 equally sized energy bins. Air, plexiglass, cortical bone (as defined by ICRU 44)¹⁹, and iron were used as the base materials. The energy dependent detector calibration factors were estimated as described in section (2.2.4). The IMPACT iterations start with the FBP reconstructed image. The IMPACT algorithm then uses the uncorrected raw fan beam sinogram data, normalized only to the air scan, to obtain the measured detector signal since the detector signal modeled in IMPACT includes the energy dependence in the response of individual detectors. The reconstructed image, after each update, was smoothed by a 3 x 3 Gaussian filter with 0.25 pixels standard deviation [a

MatLab™ filter]. Although the kernel of this filter has adjacent neighbours that are not largely different compared to the center pixel, it does produce a visible difference in the final image when applied to the image after each of the 150 iterations. Since the average change in pixel values in the 10 iterations beyond 150 iterations was less than 0.3%, the reconstruction algorithm was terminated after 150 iterations.

2.2.3 TomoTherapy™ Hi Art-II MVCT

The phantoms were scanned in helical mode with the J1 jaw setting and pitch = 1, and the sinogram data were converted to pseudo axial fan beam format using 2π linear interpolation. The CT numbers in 256x256 FBP images from TomoTherapy™ MVCT were converted to attenuation coefficient maps at 1 MeV (roughly the average photon beam energy of the TomoTherapy™ MVCT)²⁰ using

$$CTnumber = \frac{\mu_{tissue} - \mu_{water}}{\mu_{water}} \times 1000 .$$

The phantom without the steel inserts was also imaged for each central insert of different electron density. The corresponding FBP images were remapped to the attenuation coefficient map at 1 MeV as above for comparison purposes. Since the phantoms were scanned using the same clinical protocol as used for patients, the noise level in the phantom images is similar to that expected in clinical patient images.

For the model based image reconstruction in TomoTherapy™ MVCT, the incident photon spectrum was calculated at the isocenter (85 cm SAD) of the MVCT using the BEAMnrc¹⁷ and BEAMdp¹⁸ Monte Carlo codes. The spectrum was benchmarked against the beam attenuation by solid water as measured using

an ion chamber. The measurements and the results for this validation are described in sections (2.2.4) and (2.3.1), respectively. The number of spectral energy bins and the base materials were the same as used for the bench-top MVCT case. The energy dependent detector calibration factors were estimated as described in section (2.2.4). The FBP image, remapped to attenuation coefficients and containing metal inserts, was then used as the seed image in the IMPACT algorithm. Since the fan beam in TomoTherapyTM MVCT only covers 540 detectors (channels 58 - 597), the pseudo-axial fan beam raw data for these 540 detectors, normalized to an air scan, were used in the IMPACT algorithm. This matches the field of view (38.7 cm) and pixel resolution of the clinical TomoTherapyTM MVCT images. Similar to the bench-top MVCT case, a 3 x 3 Gaussian filter with 0.25 pixels standard deviation is applied to the image after each update. The final 256x256 image is obtained after 150 iterations.

2.2.4 Energy dependent detector calibration factor calculation

TomoTherapyTM MVCT detectors consist of compressed xenon gas chambers that are separated by metal septa (tungsten plates). The incident photons primarily interact with the tungsten septa, thereby creating lower energy particles. The lower energy particles, in turn, ionize the gas to create a charge, which is proportional to the detector signal.²¹ The tungsten septa thus give this detector a very strong energy dependence. Furthermore, the xenon gas detector is in the shape of an arc whose radius of curvature is not focused to the source. The resulting element to element variation in energy response is expected to cause

element to element variation in the measured attenuation of the beam by an object of uniform thickness. In order to characterize this response, several experiments were conducted. We measured the attenuation of the imaging beam for 17 known thicknesses (0, 0.5, 1, 1.5, 2, 3, 4 cm, then steps of 2 cm up to a total of 24 cm) of slabs of solid water [Gammex RMI[®], Middleton, WI, USA] using a static procedure (non rotating source-detector but same beam parameter and jaw settings as for the TomoTherapy[™] MVCT imaging beam). The theoretical attenuation was calculated from Eq. (2.1) using the normalized energy fluence spectrum in 20 discrete energy bins (b_{ik}). The theoretical linear attenuation coefficient (μ_{jk}) of water at these energies,¹³ as well as the calculated radiological path length (l_{ij}) for the geometry of the source, detector, and solid water slabs, were used.

The attenuation measurements by the same slabs of solid water were also carried out using an ion chamber to validate the calculated beam spectrum. An A1SL EXRADIN thimble ion chamber [Standard imaging Inc., Middleton, WI, USA] with 0.056 cc collecting volume and a PTW UNIDOS E electrometer [PTW Inc., Freiburg, Germany] were used for these measurements. The ion chamber was aligned with the help of the system positioning lasers and placed below the isocenter in between the solid water slabs and the TomoTherapy[™] detectors. The ion chamber position was far from both the detectors and the water slabs (~ 20 cm) to minimize the effect of backscatter. The field size used in the measurements (40 cm x 0.4 cm) was the same fan beam as used in MVCT imaging. The signal measured by the ion chamber (y) for each thickness of solid

water was normalized to an air scan (y_0) to get the reference attenuation [i.e., $-\ln(y/y_0)$] data.

Using this thickness vs detector signal measurement for 0 - 24 cm solid water thickness range, a_{ik} in Eq. (2.4) is calculated using a constrained optimization technique.²² For each detector, a matrix $[y_i]$ is obtained as the ratio (y/y_0) . The exponent matrix $[b_{ik} \cdot \exp(-\sum_{j=1}^J l_{ij} \mu_{jk})]$ is obtained using the normalized particle fluence spectrum (b_{ik}), the theoretical attenuation coefficient of water at the corresponding 20 discrete energy points, and solid water path lengths. Thus, the detector matrix $[y_i]$ is related to the multiplication between the exponent matrix and $[a_{ik}]$. The $[a_{ik}]$ vector for each detector is obtained by inverting this system through an iterative constrained least squared minimization technique.²² A smoothing constraint based on L_2 norm minimization of $[a_{ik}]$ was included in the cost function and a non-negativity constraint was applied after each iteration. This technique is chosen because by using the method of least squares or pseudo inverse alone we get non-physical (oscillatory or negative) solutions for $[a_{ik}]$. This is because the exponent matrix is close to being singular (i.e., it is an ill-posed problem).

A similar approach was used to determine the energy response of the bench-top MVCT detector system. Because this arc shaped detector is focused on the source, no element to element difference in the measured attenuation vs solid water thickness is expected for the bench-top MVCT, unlike the TomoTherapyTM MVCT system. Since the beam spectrum was previously validated for this system, no ion chamber measurements were carried out.

2.3 Results

2.3.1 Energy dependent detector calibration factor

The comparison of the measured attenuation with the theoretical values, calculated using Eq. (2.1), as a function of solid water thickness is shown in Fig. 2.1 (a) for two typical detectors [a central (at zero degrees) and an outer located at ~9.7 degrees from the central, the angle being taken with respect to the source] in the TomoTherapyTM MVCT system. The theoretical calculation of the attenuation using the model includes the divergent path length in solid water for each detector. In Fig. 2.1(a), the theoretical calculation assumed a uniform energy response for all detector elements. Thus the calculated curves are nearly the same for the outer and the central channel. However, there is a large difference between the central and the outer detector in the case of measurement. The difference is caused by the distinctly different energy response of the detectors resulting from the detector arc not being focused on the source. The deviation of measured attenuation from the theoretical value increases with the increasing thickness of solid water.

Figure 2.2 shows the attenuation of the TomoTherapyTM MVCT beam by the solid water as measured by the central TomoTherapyTM detector and the ion chamber. The theoretical calculation of Eq. (2.1) is also shown, which matches well with the ion chamber measurements. This indicates that the spectrum of the imaging beam used in Eq. (2.1) is valid. It also suggests that the scatter contribution, if any, in the narrow fan-beam geometry is small. A large difference

between the ion chamber and TomoTherapy™ detector measurements supports our hypothesis that the TomoTherapy™ MVCT detectors have a strong energy dependent response.

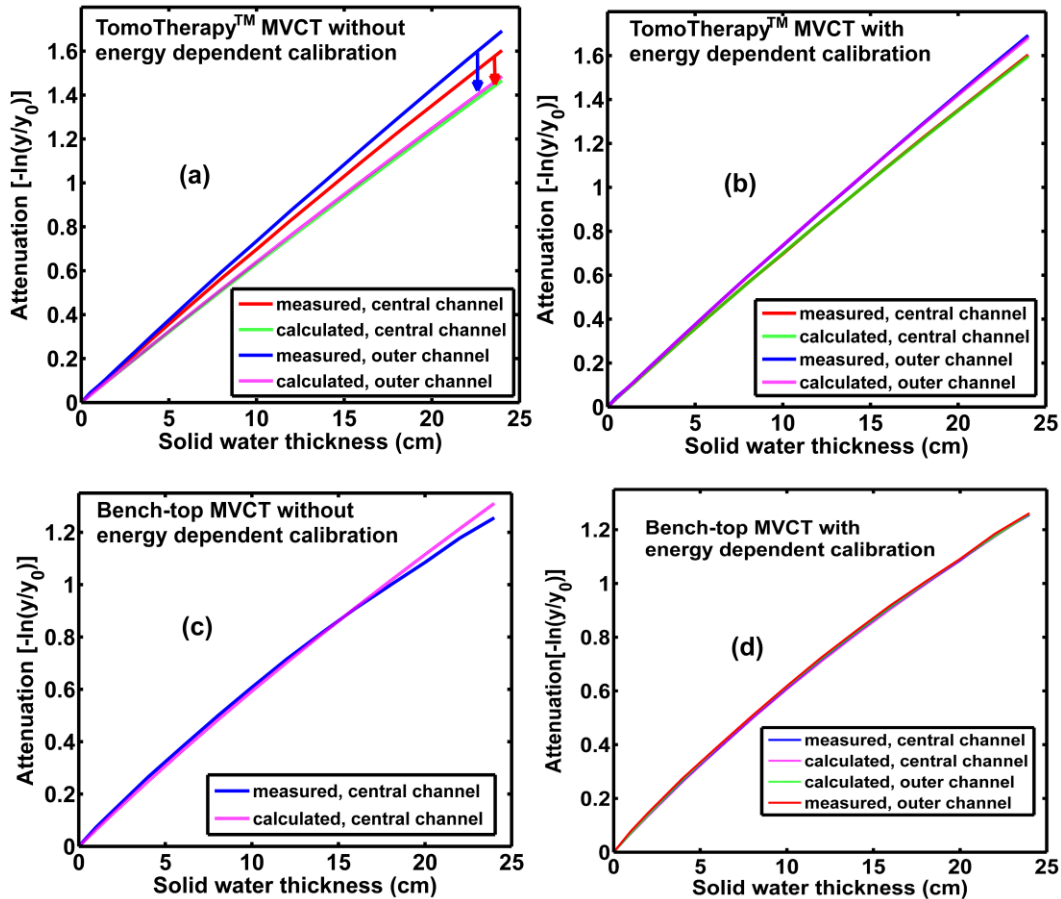


Figure 2.1. Variation of measured and calculated attenuation of beam by solid water thickness for two (one central and the other outer) TomoTherapy™ MVCT detectors (a) without and (b) with energy dependent calibration factors. In (a), the measured attenuation by the two detectors is different due to different energy response while the calculated attenuation is the same. The difference between measured and calculated attenuation in (a) for each detector gets removed in (b) after applying energy dependent calibration. Similar variations for a central detector in the bench-top MVCT are in [(c) and (d)]. The energy response of the bench-top MVCT detectors is spatially invariant and a common energy response can be used to match the calculated and measured attenuation for all the detectors, two are shown in (d). Arrows in (a) indicate the corresponding curves for a given detector.

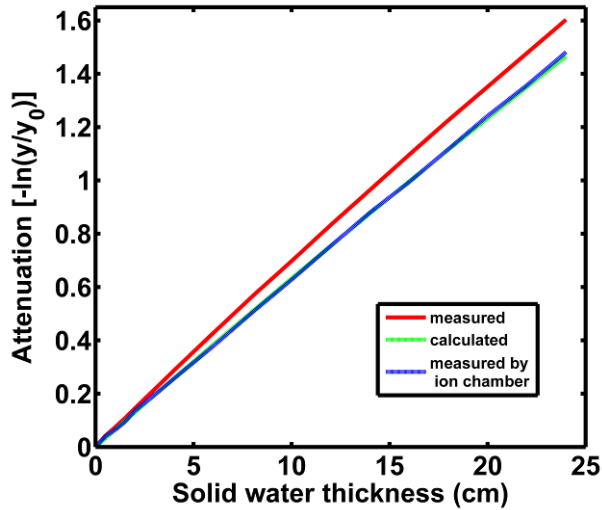


Figure 2.2. Variation of measured and calculated attenuation with solid water thickness for a central detector in TomoTherapyTM MVCT. The attenuation measured by an ion chamber follows the calculated attenuation validating the simulated energy fluence spectrum used.

The energy response of the detectors was determined and used in Eq. (2.4) to calculate the theoretical attenuation as a function of solid water thickness. The newly calculated attenuations are very close to the measured values for all detectors and for the range of solid water thickness used. The newly calculated values of the central and the same outer detector as in Fig. 2.1(a) are shown in Fig. 2.1(b) along with the measurements made with the TomoTherapyTM detectors. The difference in the measured attenuation between the outer and the central detector still persists; however, each matches to its own calculation better after the energy correction.

The variations of measured and calculated attenuation as a function of solid water thickness for a central CdWO₄ solid state detector used in the bench-top MVCT without and with the energy dependent calibration are shown in Figs. 2.1(c) and 2.1(d) respectively. Fig. 2.1 (d) also shows the variation of measured attenuation together with the calculated attenuation that includes the

energy dependent response of the central detector for an outer detector. The calculated and measured attenuation for both of these detectors are almost identical after including the same energy response [Fig. 2.1(d)]. This shows the spatial invariant nature of the energy response of the detectors. The theoretical calculations in Fig. 2.1(c) and 2.1(d) were made using Eqs. (2.1) and (2.4), respectively. The overall data in Fig. 2.1 indicate that there is more beam hardening and less energy dependence in detector response in the bench-top MVCT system compared to the TomoTherapyTM MVCT system. As a result of defocused tungsten septa, TomoTherapyTM detectors exhibit large detector to detector variation in the attenuation data although the measured attenuation for individual detectors is very linear with the solid water thickness.

2.3.2 Image reconstruction

The traditional FBP based images with the corresponding model based images in the IMPACT algorithm are shown in Fig. 2.3 for both MVCTs after 150 iterations. Figures 2.3(a) and 2.3(c) show the FBP images for the TomoTherapyTM and bench-top MVCT systems, respectively, and Figs. 2.3(b) and 2.3(d) show the corresponding model based reconstructions. The FBP method produces visibly dark shading in the area connecting the two steel rods [Figs. 2.3(a) and 2.3(c)]. In the IMPACT reconstructed images [Figs. 2.3(b) and 2.3(d)], the dark shading connecting the steel rods is almost completely removed and the uniform background restored.

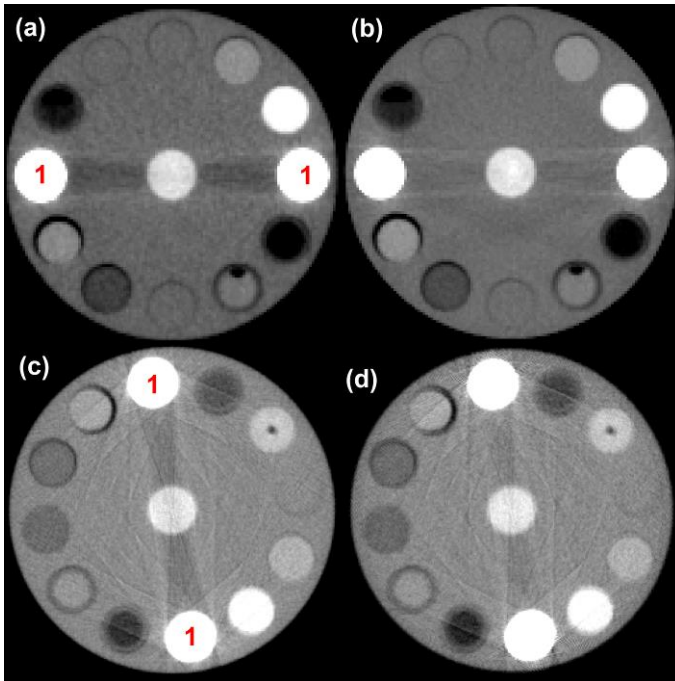


Figure 2.3. Images reconstructed using the FBP [(a) and (c)] and IMPACT methods after 150 iterations [(b) and (d)] with the central cortical bone insert. The inserts labeled ‘1’ are steel rods. Top row [(a) and (b)] are TomoTherapy™ MVCT images and bottom row [(c) and (d)] are bench-top MVCT images. The window/level in (a) and (c) are the same as in (b) and (d) respectively.

Several factors contribute to the poorer image quality for the bench-top MVCT case. The detectors in the arc are not equally spaced due to the imperfect assembly. The increased scatter produced by the slightly thicker fan beam (29 cm x 2 cm) may degrade the images. Finally, the smaller pixel size due to the smaller field of view (~28.6 cm) in bench-top geometry and the Ram-Lak filter may have increased the graininess in the images.

Figure 2.4(a) shows two profiles through the center of the FBP image from the TomoTherapy™ MVCT with the central cortical bone insert, which has a relative electron density of 1.695 compared to water. For clarity, the profiles are plotted only for the central 128 x 128 image. One of the profiles is through the region connecting the steel inserts and the other perpendicular to the first one. The

inset in Figure 2.4(a) shows the decreased attenuation coefficients of the plexiglass background in the 'shadow' created by the metal inserts. The plexiglass attenuation coefficients in the background region of the two profiles were the same in the absence of steel inserts [Fig. 2.5(a)]. Figure 2.4(b) shows the corresponding profiles in the IMPACT reconstructed image. In this image, the plexiglass attenuation coefficients in the two profiles are nearly the same. Thus, the model based algorithm results in near complete removal of the dark shading metal artifact and restoration of the uniform background between the metal rods. The inset in Fig. 2.4(b) is a zoomed view, shown for increased clarity.

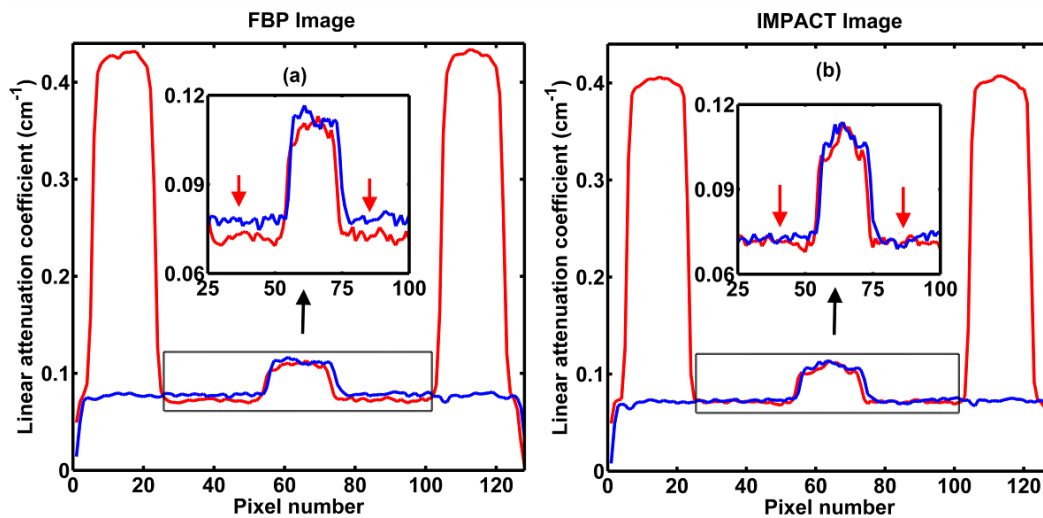


Figure 2.4. Comparisons of image profiles along the line joining the steel inserts (the curve with three peaks) and in the perpendicular direction to it (the curve with a central peak) in the TomoTherapyTM MVCT image (a). The uniform plexiglass background which is distorted in the FBP image is restored in the IMPACT image, shown in (b). Insets in both figures show the restored background more clearly.

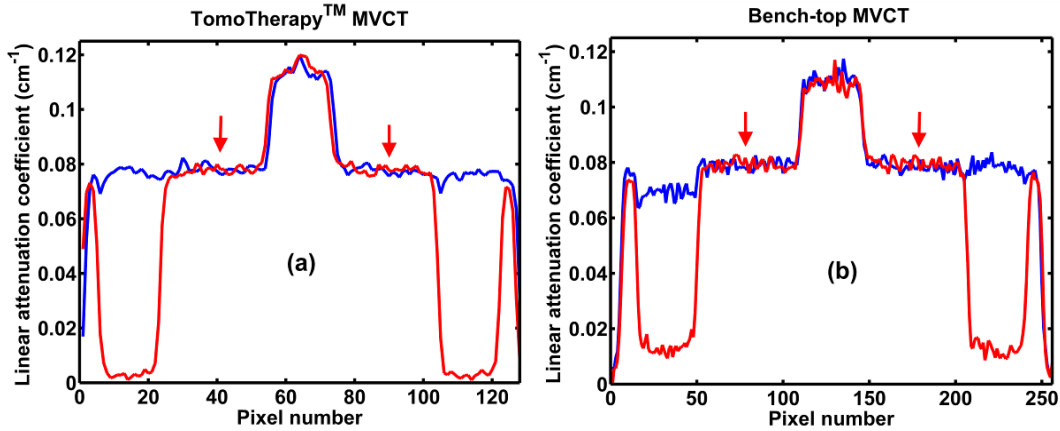


Figure 2.5. Comparisons of image profiles as in Fig. 2.4 in the FBP image of (a) the TomoTherapy™ MVCT system and (b) the bench-top MVCT system, both in the absence of metal rods. Arrows indicate the uniform plexiglass background.

Figures 2.6(a) and 2.6(b) show the data for the bench-top MVCT system corresponding to the data in Figs. 2.4(a) and 2.4(b), respectively, for the TomoTherapy™ MVCT system. Model based image profiles in Fig. 2.6(b) show an improvement in restoring the degraded attenuation coefficient map in the shaded region between the metal rods compared to the corresponding profiles in Fig. 2.6(a) for the FBP image. Figure 2.5(b) shows that the plexiglass attenuation coefficient in the background region of the two profiles was the same in the absence of steel inserts. However, due to the fine streak image artifacts originating from the metals, there is larger fluctuation in the profiles at some of the pixels in the images with steel rods [Figs. 2.6(a) and 2.6(b)]. These fluctuations make the improved match between two profiles in Fig. 2.6(b) less obvious. These streaks are probably due to the tiny air gaps present between the detector blocks (each block contains 16 detectors and there are 20 such blocks) in the bench-top MVCT system.

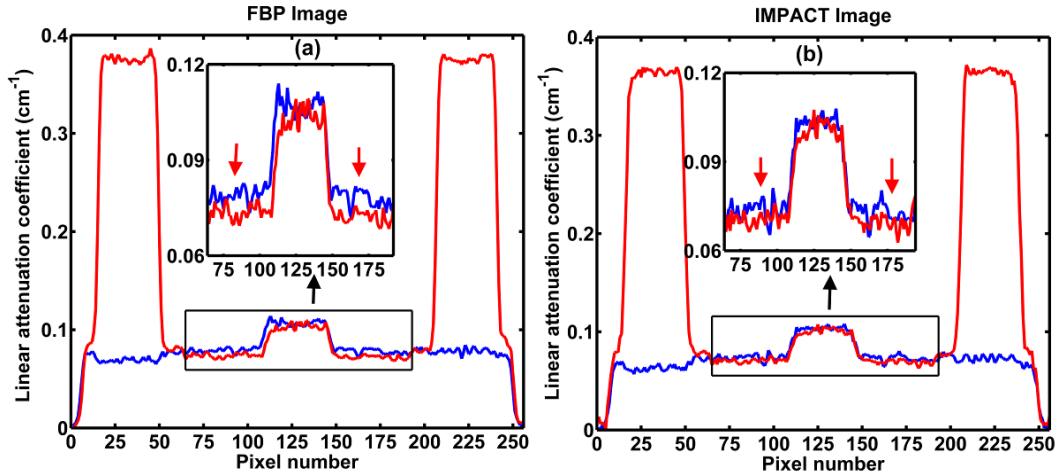


Figure 2.6. Comparisons of image profiles along the line joining the steel inserts (the curve with three peaks) and in the perpendicular direction to it (the curve with a central peak) in the bench-top MVCT image (a). The uniform plexiglass background, destroyed in the FBP image is restored in the IMPACT image in (b). Insets in both figures show the restored background more clearly.

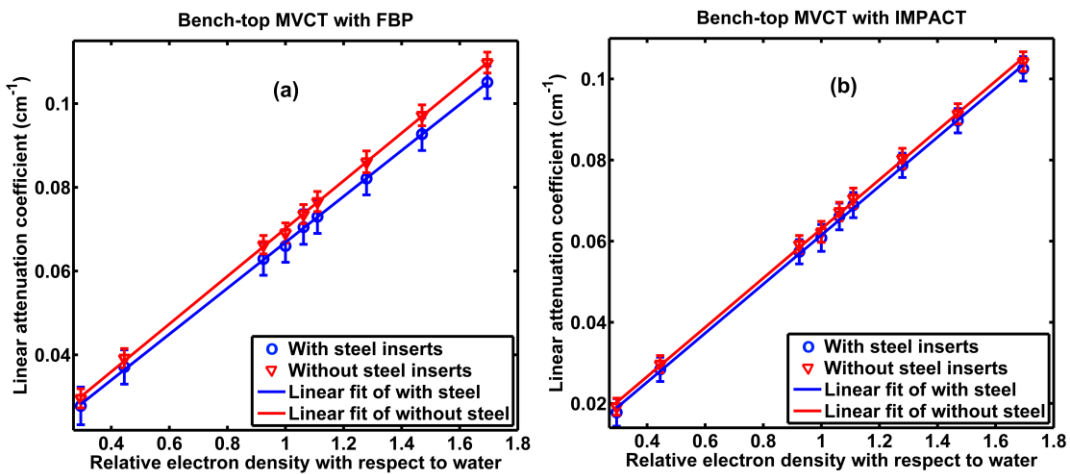


Figure 2.7. Variation of average pixel values with relative electron density in the (a) FBP reconstructed and (b) IMPACT reconstructed bench-top MVCT images for a central insert in the presence (circles) and absence (diamonds) of peripheral steel inserts. The average pixel values in the IMPACT reconstructed images in the presence of steel inserts are close to the corresponding values in the absence of steel inserts within the experimental uncertainty. The red and blue curves are the linear fits to the corresponding points.

Figure 2.7(a) shows the variation of average attenuation coefficient in the region of interest (ROI) within the central insert as a function of its relative electron density, both in the presence and in the absence of the steel inserts, for

the bench-top MVCT system. Both sets of data indicate the usual linearity of measured attenuation in the MVCT image with electron density. However, the steel rods reduce the attenuation coefficient of the central insert at all electron densities. Also, the slope of the linear fit is somewhat smaller in the presence of steel inserts indicating increased beam hardening for some of the views. Assuming the average attenuation coefficients in the absence of steel inserts, over the range of the electron density in Fig. 2.7(a) as calibration points, and using linear interpolation, the electron density in the corresponding ROI of central insert in the presence of the steel rods is calculated. Thus, the reduction in attenuation coefficient caused by the steel rods can be expressed as a percentage reduction in the electron density. The dark shading connecting the steel rods in the FBP images causes 4.0% - 9.5% underestimation of relative electron density with an average of $(6.3 \pm 1.8)\%$ in the central insert for the relative electron density range of (0.295 - 1.695). For the insert representing lung with a relative electron density of 0.295, the average underestimation is 9.5%. Figure 2.7(b) shows the corresponding data in the IMPACT reconstructed images. The average attenuation coefficients of the central inserts in the presence of the steel rods are very close to the corresponding values in the absence of steel rods. Similar to the FBP case, the attenuation coefficients of the central inserts in the phantom containing the steel rods were converted to electron densities. The underestimation of relative electron density in the IMPACT image for the central insert is 1.4% - 6.8%, with an average underestimation of $(3.1 \pm 1.7)\%$.

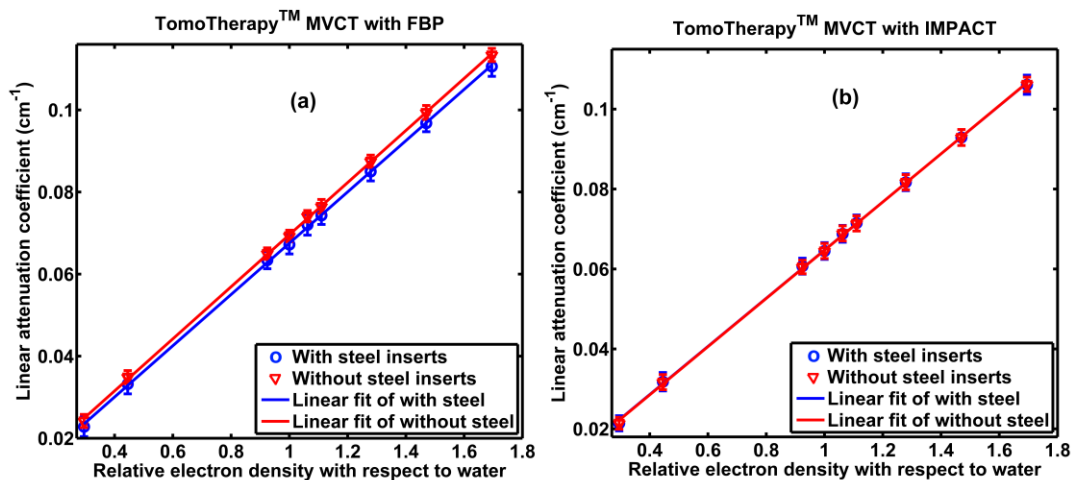


Figure 2.8. Variation of average pixel values with relative electron density in the (a) FBP reconstructed and (b) IMPACT reconstructed TomoTherapy™ MVCT images for a central insert in the presence (circles) and in absence (diamonds) of peripheral steel inserts. The average pixel values in the IMPACT reconstructed images in the presence of steel inserts are close to the corresponding values in the absence of steel inserts within the experimental uncertainty. The red and blue curves are the linear fits to the corresponding points.

In the TomoTherapy™ MVCT images, there is an inherent artifact called “button artifact” at the center of the image. This artifact appears as a small circular region of either higher or lower intensity in alternate slices. It results from the rapidly changing detector response in the central region of the non focused detector array²³ to the radiation source. This button artifact is present in the FBP reconstructed images and carries through the iterations of the IMPACT algorithm. As suggested in Ref (23), we have excluded this artifact in the calculation of average attenuation coefficient in the ROI of the central inserts, both in the FBP and the IMPACT reconstructed images. Figures 2.8(a) and 2.8(b) show the data for TomoTherapy™ MVCT images corresponding to the data in Fig. 2.7(a) and 2.7(b) respectively for bench-top MVCT. Similar to the bench-top case, the steel rods cause a reduction in the measured attenuation coefficients of the central insert in the FBP images [Fig. 2.8(a)]. The shading artifact creates 2.6% - 6.7%

underestimation of the electron density with an average of $(3.7 \pm 1.4)\%$ in the central insert of the FBP image. IMPACT has improved the dark shading, and the average attenuation coefficients in the ROI inside the central insert are almost identical to the corresponding average attenuation coefficients in the absence of steel inserts [Fig. 2.8(b)]. The underestimation of electron density is -0.4% to $+0.1\%$, with an average of $(-0.1 \pm 0.2)\%$ in the full range of electron density studied.

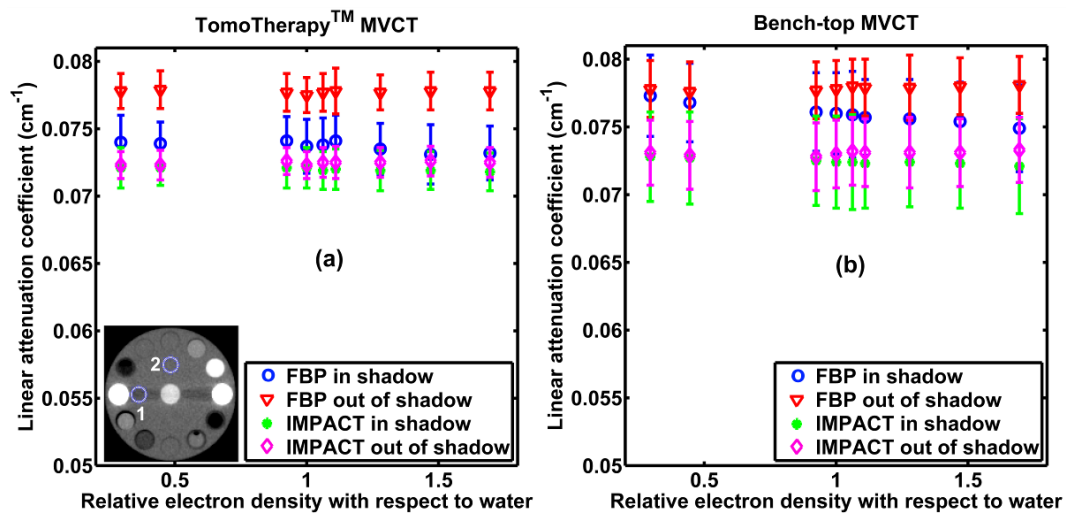


Figure 2.9. Variation of mean pixel values of the plexiglass background with relative electron density in the shadow (1) and out of the 'shadow' (2) of the steel rods in the FBP and IMPACT reconstructed images from (a) the TomoTherapy™ MVCT system and (b) the bench-top MVCT system.

Figures 2.9(a) and 2.9(b) show the variation of the average attenuation coefficients of two ROIs in the plexiglass background. The first ROI, indicated by '1' in the inset of Fig. 9(a), is in the 'shadow' artifact caused by the metal inserts, and the second ROI is out of 'shadow' as indicated by '2'. These data are presented as a function of the relative electron density of the central insert in both MVCT images. Ideally, the average attenuation coefficients in the ROIs '1' and

'2' should be the same and equal to that of the plexiglass background. However, the metal artifact makes the mean of ROI '2' smaller than the mean of ROI '1'. The deviation between two ROIs increases [Fig. 2.9(a) and 2.9(b)] with an increase in the electron density of the central insert suggesting the dark 'shadow' created by the metal rods becomes darker in the presence of a denser insert between the steel rods. As noted previously, the IMPACT algorithm reduces this difference by removing the 'shadow' artifact. The average attenuation coefficients within the two ROIs from the images obtained by the IMPACT algorithm are remarkably closer to each other. In the TomoTherapyTM MVCT image [Fig. 2.9(a)], the underestimation of electron density in ROI '2' compared to ROI '1' in the FBP image is 5.9% - 7.2% (for various central inserts) with an average underestimation of $(6.4 \pm 0.5)\%$. The amount of underestimation generally increases with increasing electron density of the central insert. In the IMPACT reconstructed images, the underestimation is only 0.3% - 1.0%, with an average underestimation of $(0.7 \pm 0.3)\%$. Similarly, in the bench-top MVCT images [Fig. 2.9(b)], the underestimation of electron density in the FBP images is 0.8% - 4.7%, with an average underestimation of $(2.9 \pm 1.2)\%$. In the IMPACT reconstructed images the underestimation is only 0.3% - 1.8%, with an average underestimation of $(0.9 \pm 0.5)\%$.

2.4 Discussion

Previous metal artifact reduction methods have mostly been applied to diagnostic CT systems, with an emphasis to reduce the visibility of artifacts. In many of these techniques, the metal is segmented and replaced with a lesser density material to reduce the artifacts.^{3,4} Moreover, due to the excessive beam hardening caused by the metal, the reconstructed metal pixels in the initial FBP images are generally incorrect. Thus, even if the metal segmented from the initial FBP image is replaced back in the final, artifact reduced image, the electron density of the metal estimated from the image is generally not correct and must be overridden. For the specific application of CT to radiation therapy planning, both the visual aspects of the metal artifact and its impact on the accuracy of the CT numbers (and hence the electron density) in the images are important. It is widely accepted that MVCT imaging can reduce these artifacts to a large degree. In this study, we demonstrated that the MVCT system produces shading artifacts in the images of phantoms containing high density bilateral steel inserts (similar to bilateral hip prostheses in a patient), which results in inaccurate CT numbers in the shadow of artifacts. Basically, the electron density in the shadow of artifacts is underestimated due to the presence of metal. To the best of our knowledge, this is the first study in which the MAR technique is applied to MVCT images in an attempt to reconstruct accurate attenuation coefficients.

The conventional FBP method of image reconstruction assumes that a linear projection, i.e., a view consisting of line integrals, of a 2-D attenuation map can be obtained from the detector data. Spectral hardening, scattered radiation

reaching the detector, and the finite dimensions of the detector make it difficult to obtain linear projections from the detector data. However, the error caused by these factors, especially after empirical spectral hardening corrections, is generally small if no metal objects are present in the patient. The presence of metal can produce larger errors and artifacts. In this particular work, a model of signal formation in the MVCT detectors is used that explicitly accounts for the spectral hardening and the variable energy response of the detectors. Our current implementation of the algorithm in MatLabTM, using a 2.67 GHz, i7 CPU without any time reduction strategies, takes a day to correct a slice, such as shown in Fig. 2.3. The signal formation model can be extended to include small amounts of scattered radiation reaching the detectors and the dimensions of the detectors. Since the detector signal is non-linearly related to the attenuation coefficient map, the solution necessitates the use of an iterative method of reconstruction that increases the computation time. The use of an iterative method, in addition to reducing the effect of metal on the image visibility and CT numbers, may also help in reducing the noise in the image. This is more evident in the TomoTherapyTM MVCT images of this investigation, i.e., the standard deviations within the ROIs of the central insert were smaller in the IMPACT reconstructions, but it is also present to a lesser extent in the images from the bench-top MVCT.

At the authors' institution, the TomoTherapyTM MVCT is routinely used for the treatment planning of prostate patients with hip prostheses. The MVCT images provide more information in the shadow of the artifact compared to diagnostic CT. It is expected that the artifact reduced MVCT images would

further improve the visibility of prostate in the shadow of the artifact. Further investigations are required to study the improvement in the radiotherapy dose calculation accuracy resulting from this difference in the electron density.

Our MAR technique has significantly reduced the shading metal artifact and restored the degraded uniform background. The difference in the estimated electron density, from the true value, after IMPACT reconstruction is less than 1% in the background plexiglass and less than 3% averaged over the range of electron densities investigated for the bench-top MVCT system. In the TomoTherapy™ MVCT system, this error is < 0.5% for all the electron densities studied. Our method has not introduced and is unlikely to introduce secondary artifacts as long as the correct geometrical information of the scanner is used. This is unlike the segmentation/interpolation based correction methods, which can introduce secondary artifacts and lose anatomical information close to the implant^{3,5,24,25}. This artifact reduced image may be used directly in radiotherapy treatment planning, however further investigation involving patient images is necessary. In addition, it can be used as a good initial image for the further development of metal artifact reduction methods in a kVCT image set. With the ever increasing computing capacity this iterative method could be used in radiotherapy treatment planning where imaging and treatment are generally at least on the order of hours apart from one another.

2.5 Conclusions

This study has demonstrated the importance of model based image reconstruction in two MVCT systems for metal artifact reduction. With accurate geometrical information of the CT scanner and the photon beam spectrum, the shading metal artifacts can be almost completely removed in MVCT images using an iterative reconstruction algorithm such as IMPACT. The error in linear attenuation coefficient, and consequently the error in electron density, is significantly reduced by this method. The difference in the electron density in the plexiglass background is <1%, and it is < 3% averaged over the range of electron densities investigated for the bench-top system. For TomoTherapy™ MVCT system, the average difference in the electron density is <0.5% over the range of electron densities investigated. However, the accurate modeling of detectors' energy dependent response and a model for the energy dependence of relevant photon interaction processes are crucial for the successful implementation of this method.

2.6 References

1. B. De Man, J. Nuyts, P. Dupont, G. Marchal, and P. Suetens, "Metal streak artifacts in X-ray computed tomography: A simulation study," *IEEE Trans. Nucl. Sci.* **46**, 691-696 (1999).
2. W. A. Kalender, R. Hebel, and J. A. Ebersberger, "Reduction of CT artifacts caused by metallic implants," *Radiology* **164**, 576-577 (1987).
3. M. Yazdi, L. Gingras, and L. Beaulieu, "An adaptive approach to metal artifact reduction in helical computed tomography for radiation therapy treatment planning: experimental and clinical studies," *Int. J. Radiat. Oncol. Biol. Phys.* **62**, 1224-1231 (2005).

4. W. Veldkamp, R. Joemai, A. Molen, and J. Geleijns, "Development and validation of segmentation and interpolation techniques in sinograms for metal artifact suppression in CT," *Med. Phys.* **37**, 620-628 (2010).
5. E. Meyer, R. Raupach, M. Lell, B. Schmidt, and M. Kachelriess, "Normalized metal artifact reduction (NMAR) in computed tomography," *Med. Phys.* **37**, 5482-5493 (2010).
6. X. Zhang, J. Wang, and L. Xing, "Metal artifact reduction in x-ray computed tomography (CT) by constrained optimization," *Med. Phys.* **38**, 701-711 (2011).
7. Y. Zhang, L. Zhang, X. R. Zhu, A. K. Lee, M. Chambers, and L. Dong, "Reducing metal artifacts in cone beam CT images by pre-processing projection data," *Int. J. Radiat. Oncol. Bio. Phys.* **67**, 924-932 (2007).
8. B. De Man, J. Nuyts, P. Dupont, G. Marchal, and P. Suetens, "An iterative maximum-likelihood polychromatic algorithm for CT," *IEEE Trans. Med. Imaging.* **20**, 999-1008 (2001).
9. J. F. Williamson, B. R. Whiting, J. Benac, R. J. Murphy, G. J. Blaine, J. A. O'Sullivan, D. G. Politte, and D. L. Snyder, "Prospects for quantitative computed tomography imaging in the presence of foreign metal bodies using statistical image reconstruction," *Med. Phys.* **29**, 2404-2418 (2002).
10. D. Sawkey, M. Lu, O. Morin, M. Aubin, S. S. Yom, A. R. Gottschalk, A. Bani-Hashemi, and B. A. Faddegon, "A diamond target for megavoltage cone beam CT," *Med. Phys.* **37**, 1246-1253 (2010).
11. M. Schirm, S. Yartsev, G. Bauman, J. J. Battista, and J. Van Dyk, "Consistency check of planned adaptive option on helical tomotherapy," *Technol. Cancer Res. Treat.* **7**, 425-432 (2008).
12. S. Martin, and S. Yartsev, "kVCT, MVCT, and hybrid CT image studies – Treatment planning and dose delivery equivalence on helical tomotherapy," *Med. Phys.* **37**, 2847-2854 (2010).
13. <http://www.nist.gov/pml/data/xcom/index.cfm>.

14. O. S. Marenkov, "On a formula for the computation of the cross section for the production of a pair of gamma-quanta in the statistical modeling of transport processes," *Atom. Energ.* **35**, 858-859 (1973).
15. R. L. Siddon, "Fast calculation of the exact radiological path for a three-dimensional CT array," *Med. Phys.* **12**, 252-255 (1985).
16. P. Kirvan, T. Monajemi, B. G. Fallone, S. Rathee, "Performance characterization of a MVCT scanner using multislice thick, segmented cadmium tungstate - photodiode detectors," *Med. Phys.* **37**, 249-257 (2010).
17. D. W. O. Rogers, B. A. Faddegon, G. X. Ding, C.-M. Ma, J. Wei, and T. R. Mackie, "BEAM: A Monte Carlo code to simulate radiotherapy treatment units," *Med. Phys.* **22**, 503-524 (1995).
18. C.-M. Ma and D. W. O. Rogers, BEAMDP Users Manual Report Pirs-0509 (NRCC, Ottawa, Canada, 2004).
19. ICRU - International Commission on Radiation Units and Measurements, "Tissue substitutes in radiation dosimetry and measurement," ICRU Report No. 44 (International Commission on Radiation Units and Measurements, Bethesda MD, 1989).
20. R. Jeraj, T. R. Mackie, J. Balog, G. Olivera, D. Pearson, J. Kapatoes, K. Ruchala, and P. Reckwerdt, "Radiation characteristics of helical tomotherapy," *Med. Phys.* **31**, 396-404 (2004).
21. H. Keller, M. Glass, R. Hinderer, K. Ruchala, R. Jeraj, G. Olivera, and T. R. Mackie, "Monte Carlo study of a highly efficient gas ionization detector for megavoltage imaging and image-guided radiotherapy," *Med. Phys.*, **29**, 165-175, (2002).
22. J. Weese, "A reliable and fast method for the solution of Fredholm integral equations of the first kind based on Tikhonov regularization," *Comput. Phys. Commun.* **69**, 99-111 (1992).
23. K. M. Langen, N. Papanikolaou, J. Balog, R. Crilly, D. Followill, S. M. Goddu, W. Grant III, G. Olivera, C. R. Ramsey, and C. Shi, "QA for helical TomoTherapy: Report of the AAPM Task Group 148," *Med. Phys.* **37**, 4817-4853 (2010).

24. J. Muller, and T. M. Buzug, "Spurious structures created by interpolation-based CT metal artifact reduction," Proc. of SPIE Med. Imag. **7258**, 1Y1-1Y8 (2009).
25. P. T. Liu, W. P. Pavlicek, M. B. Peter, M. J. Spangehl, C. C. Roberts, and, R. G. Paden, "Metal artifact reduction image reconstruction algorithm for CT of implanted metal orthopaedic devices: a work in progress," Skelet. Radiol. **38**, 797-802 (2009).

CHAPTER 3 : Modified IMPACT in kVCT

3.1 Introduction

Our study¹ presented in chapter 2 revealed that the solid state detector in the bench-top MVCT system has a less pronounced but finite energy dependent response. We expect a stronger energy response in commercial solid state kVCT detectors because of the larger variation of the attenuation coefficient of the detector with energy, and greater beam hardening within the patient for low energy kV photons. Therefore we expect that the inclusion of this response into the model (in IMPACT) will reduce metal artifacts in kVCT. We calculated this response exactly the same way as we did for MVCT¹ and modelled it in IMPACT, where only the photoelectric effect and Compton scattering process were included in the expression for the linear attenuation coefficient. However, this modified IMPACT algorithm did not significantly reduce metal artifacts in kVCT for high density metals such as steel, and did not perform better than the existing IMPACT algorithm² without energy dependent detector response. We hypothesize that photon starvation may result in the measured data being uninterpretable by the model in the modified IMPACT algorithm. Therefore, to establish that this is indeed the case, we explored the possibility of photon starvation of the imaging kV beam at the detectors.

3.2 Attenuation vs thickness of steel plates

We conducted attenuation measurements as a function of steel absorber thickness by using a range of steel plate thicknesses. A Phillips Big Bore CTTM

scanner was used in static mode where the couch moved into the bore at constant speed with non-rotating source and detector, i.e. in the scout image acquisition mode. The beam parameters were 120 kVp and 200 mAs. We sandwiched steel plates of a given thickness between two 12-cm-thick solid water blocks, (total thickness of solid water was 24 cm) and measured the transmitted signal (y) which was normalized to the air scan signal (y_0) to get attenuation [i.e., $-\ln(y/y_0)$] data for the central detector.

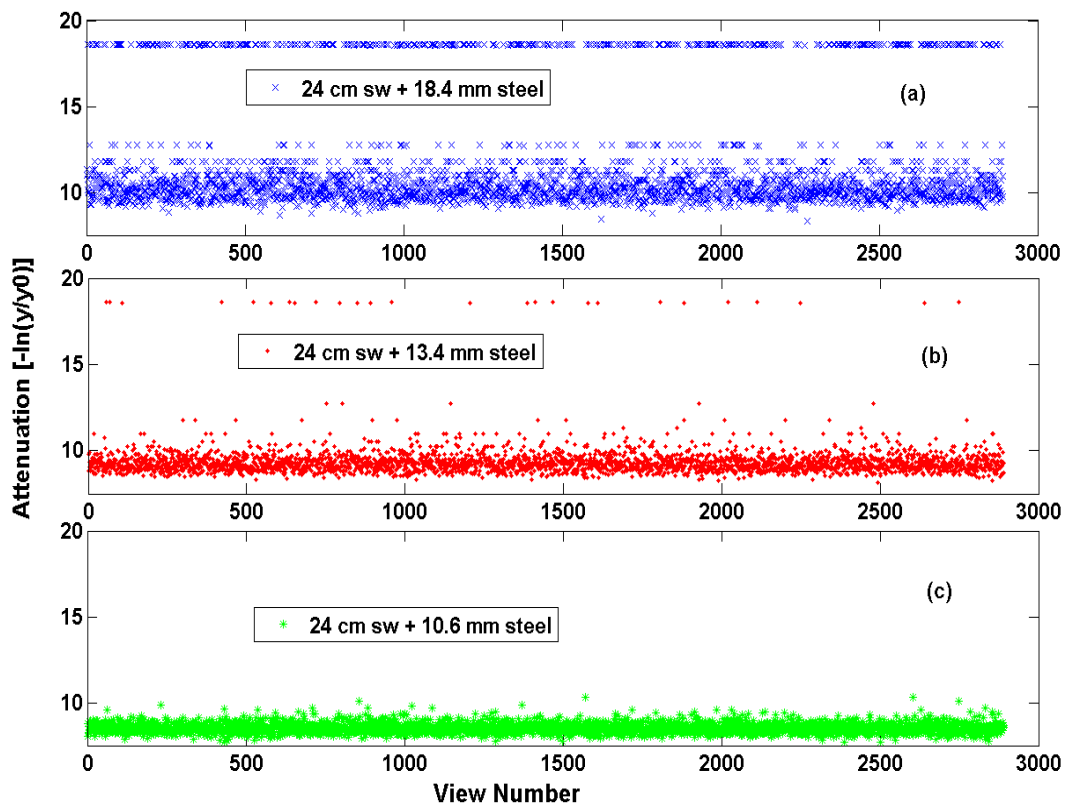


Figure 3.1. The attenuation measured by the central detector for three different thicknesses of steel plates sandwiched between two solid water blocks each 12 cm thick. Here, a view number corresponds to a particular couch position in the scout scan mode while the source and detectors remained stationary. For steel thickness of 18.4 mm (a) and somewhat for 13.4 mm (b), the variation in measured attenuation is reflective of quantization noise indicated by the presence of a finite number of discrete levels. This indicates that the detector signal is so small that the quantization levels in the A-to-D converter are visible. This is not the case for a steel thickness of 10.6 mm (c) where the variations in the measured attenuation are characteristics of quantum mottle.

The variation of the measured attenuation, for three different thicknesses of steel plates (10.6 mm, 13.4 mm, and 18.4 mm) sandwiched between two 12 cm thick solid water blocks, as a function of parallel views through the constant thickness of the steel plate is shown in Fig. 3.1. The plots in Fig. 3.1 show that there is a large variation in the attenuation value between the views for a given thickness of steel plate. When the steel plate thickness is 10.6 mm, the variations in the measured attenuation are characterized by the quantum noise. At steel thicknesses of 18.4 mm (and somewhat at 13.4 mm), the measured attenuation shows discrete levels as a function of view number in addition to the quantum noise. This indicates that the detector signal is so small that the quantization levels in the *analog to digital (A-to-D)* converter are visible. This is the indication for photon starvation.

Further insight into this effect is presented in Fig. 3.2 where the histogram of the measured attenuation for the central detector is presented with varying thickness of steel plate sandwiched between the solid water blocks. When the steel plate thickness changes from 7.6 mm to 10.6 mm [Fig. 3.2 (a) to Fig. 3.2 (c)], the base of the Gaussian-like histogram widens, indicating increase in the level of quantum mottle. When the steel thickness reaches 13.4 mm [Fig. 3.2 (d)], the shape of the distribution starts to change. The histogram now contains a few discrete lines towards the higher attenuation side of the distribution. One of the lines is at a very high attenuation value (18.6). From a steel thickness of 18.4 mm to 36.7 mm [panels (e) to (i) in Fig. 3.2], the height of these discrete attenuation points increases while keeping the same position

(i. e., the same attenuation value). Also, the mean position of the rest of the points is essentially the same at around the attenuation value of 10. These discrete lines represent the quantization levels in the A-to-D conversion process and a fixed attenuation value indicates the presence of *photon starvation*. The maximum value of the measured attenuation (18.6) comes from the maximum limit of the data acquisition system resulting from the minimum possible quantized signal detected in presence of *photon starvation*.

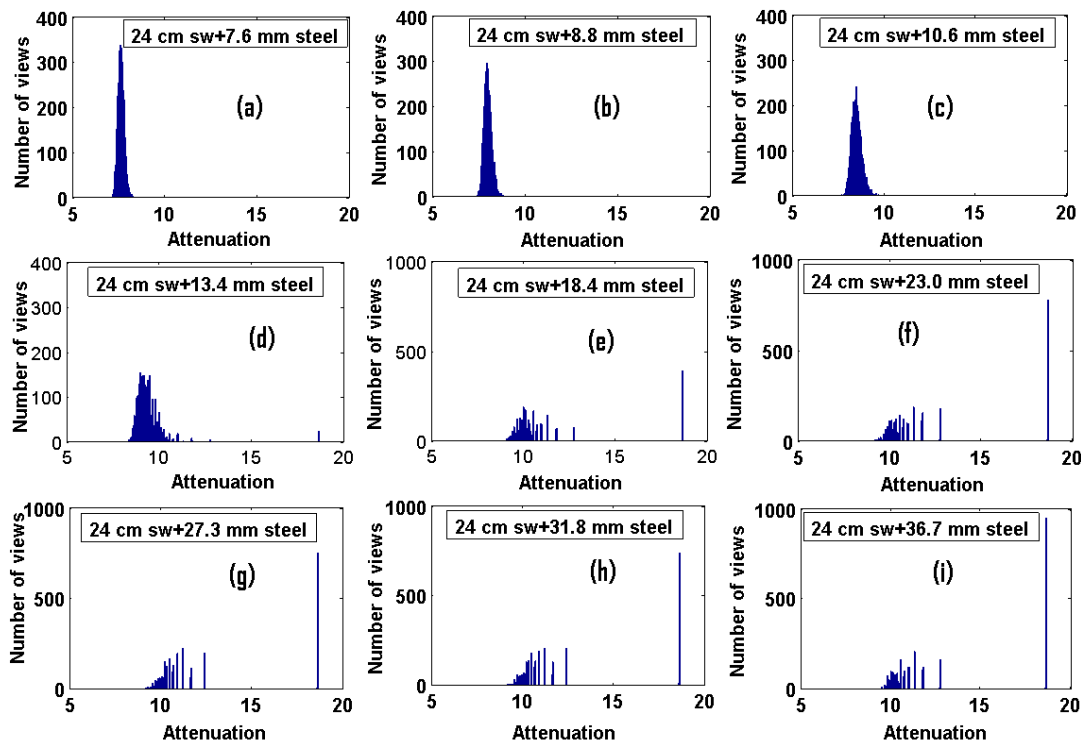


Figure 3.2. Histogram of the attenuation measured by the central detector for varying thicknesses of steel plates sandwiched between two solid water blocks each 12 cm thick. Here, number of views indicates a particular couch position in the scout scan mode for which a particular value of attenuation was recorded while the source and detectors remained stationary. The histograms from (a) to (c) show the broadening of the attenuation distribution curve, indicating the rise in quantum noise with the increase in steel plate thickness. When the steel thickness reaches 13.4 mm (d), new discrete lines appear, one of them at the largest attenuation value of 18.6. Starting at the steel thickness of 18.4 mm (e), the Gaussian-like shape of the histogram completely disappears and the discrete lines are seen at the same attenuation values with increasing height, reflecting the quantization levels in the A-to-D conversion process.

3.3 Conclusion

This study shows that photons reaching the kVCT detector after passing through a thick metal plate are either so low in number that the signal measured has large quantum noise, or are completely absorbed inside the attenuating plate so that the discrete quantization levels become visible. This is the condition of *photon starvation*. In either case, the measured signal does not follow the signal model used in the IMPACT algorithm. As such, the modified IMPACT technique that requires a real measured signal as an input cannot model this situation, nor can we introduce any model for this effect. The practical size of a steel hip implant is at least 13 mm in diameter, and hence we cannot apply a model based method such as the modified IMPACT algorithm to reduce metal artifacts in kVCT for such higher density implants.

3.4 References

1. M. R. Paudel, M. Mackenzie, B. G. Fallone, and S. Rathee, "Evaluation of metal artifacts in MVCT systems using a model based correction method," *Med. Phys.* **39**, 6297-6308 (2012).
2. B. De Man, J. Nuyts, P. Dupont, G. Marchal, and P. Suetens, "An iterative maximum-likelihood polychromatic algorithm for CT," *IEEE Trans. Med. Imaging.* **20**, 999-1008 (2001).

CHAPTER 4 : NMAR in kVCT using MVCT priors, a phantom study

*A version of this chapter has been published: M. R. Paudel, M. Mackenzie, B. G. Fallone, and S. Rathee, "Evaluation of NMAR in kVCT using MVCT prior images for radiotherapy treatment planning," Med. Phys. **40**, 081701 (2013).*

4.1 Introduction

Many metal artifact reduction (MAR) techniques¹⁻¹² have been proposed in diagnostic kilovoltage CT (kVCT) imaging. Two important groups of these algorithms are projection completion (PC) and model based statistical reconstruction methods. PC methods identify the projection data corresponding to metals in the raw sinogram, and replace them with the interpolated values from the surroundings. This replacement greatly reduces the metal artifacts but often introduces secondary artifacts. One such method, normalized MAR (NMAR),⁵ attempts to reduce these secondary artifacts by normalizing the raw projection data before interpolation using the calculated projection data of a prior image. The prior image is a tissue (i.e. air, soft tissue, bone, and metal) classified image. The prior image is obtained in two steps. Firstly, the general PC method is used to obtain an artifact reduced image. The general PC method uses linear interpolation in the detector channel direction to replace sinogram values in the location of the metal portion of the sinogram followed by reconstruction using filtered backprojection (FBP), and then subsequently puts the metal back into the image. Secondly, the artifact reduced image is segmented into various tissue classes using thresholding, and then assigned fixed CT numbers to the air and water classes. In the image corrected by the general PC method before classification, the

shading and streaking is significantly reduced but secondary artifacts are often introduced. The tissue classification step further introduces segmentation errors due to non optimal classification. These segmentation errors present in the prior image can pass on to the final corrected image in the NMAR method.¹³ Thus, the contrast and edge information of the anatomical structures is often reduced.^{12,13} The ‘closeness’ of the prior image to the actual object is shown to be more critical¹³ than the particular interpolation method for artifact reduction in the NMAR method.

Model based methods show great promise for metal artifact reduction, but they need longer computing times, and may require the location and composition of the metallic regions¹¹ to be known *a priori*. Among the model based methods, the iterative maximum-likelihood polychromatic (IMPACT) algorithm has been remarkably successful¹⁰ in reducing artifacts in kVCT images due to lightly attenuating metals such as aluminum. In the presence of thicker and denser implants such as steel, significant artifacts remain in the corrected images. The method is unable to correctly restore the CT numbers within the metal in the corrected images in kVCT. These remaining issues are most probably due to the photon starvation effect. In order for the signal formation model to properly predict the metal attenuation, the model needs measured transmission data through the metal which is not available in kVCT due to photon starvation.

Megavoltage CT (MVCT) images are dramatically less susceptible to metal artifacts due to reduced photon starvation and reduced beam hardening at MV energies. However, there can be significant shading artifacts in the presence

of denser and thicker implants, but these artifacts can be reduced using a modified IMPACT algorithm.¹⁴ MVCT images give the correct attenuation properties of metal and have been routinely used in the clinic for image guided radiotherapy (IGRT), but lack the superior soft tissue contrast inherent in kVCT images.

The aim of this study is to use uncorrected and corrected (using the modified IMPACT method) MVCT images without tissue classification as prior images for the NMAR technique to reduce the metal artifacts in kVCT images. Although the noise in the MVCT images is relatively larger, it is hypothesized that the avoidance of the segmentation/tissue classification step in addition to reduced artifacts in the MVCT prior images will avoid the contrast and edge loss problems of the existing NMAR method. More importantly, the correct attenuation map of metals in the MVCT image can be utilized to get the correct CT number of metal in the kVCT image, which can't be obtained from any of the existing MAR methods in kVCT.

4.2 Methods and Materials

4.2.1 IMPACT modifications for MVCT

The modified IMPACT algorithm we used for MVCT has been described in detail in Ref. 14. In brief, the algorithm uses the polychromatic detector signal (\hat{y}_i) model:

$$\hat{y}_i = \sum_{k=1}^K a_{ik} b_{ik} \cdot \exp\left(-\sum_{j=1}^J l_{ij} \mu_{jk}\right) \quad 4.1$$

where ' i ' is the index of the projection ray, ' k ' is the energy bin, and ' j ' is the image pixel. Also, b_{ik} is the photon fluence spectrum (practically it is considered

independent of the projection ray ' i '). The factors a_{ik} represent the relative signal of the detector measuring the i^{th} ray for the k^{th} energy bin per unit fluence in the k^{th} energy bin. The factor l_{ij} is the intersection length of the i^{th} ray with pixel j , and μ_{jk} represents the linear attenuation coefficient of the j^{th} pixel for the k^{th} photon energy. The energy dependent linear attenuation coefficient is expressed as a linear combination of Compton, photoelectric, and pair/triplet production components. Each of these components further consists of an energy dependent function and a material dependent parameter. It is further assumed that the material dependent parameters are unambiguously determined using the attenuation coefficients at a specified reference energy, the energy equal to or close to the mean energy of the imaging beam spectrum. For this purpose, a list of possible base materials, such as air, water, bone, metal etc., is chosen. The x-ray beam path lengths (l_{ij}) in Eq. (4.1) are calculated using Siddon's algorithm¹⁵ for the geometry of the imaging system. Using the normalized signal matrix $[y_i]$ measured by each detector for zero to 34 cm total thickness of solid water [Gammex RMI[®], Middleton, WI, USA] and using the calculated exponent matrix $[b_{ik} \cdot \exp(-\sum_{j=1}^J l_{ij} \mu_{jk})]$, a_{ik} in Eq. (4.1) is calculated by inverting this system with the help of an iterative constrained least squares minimization technique subjected to smoothing and non-negativity constraints.¹⁶

The reconstruction of the image is achieved by maximizing the Poisson likelihood $L = \sum_{i=1}^I (y_i \cdot \ln(\hat{y}_i) - \hat{y}_i)$ where y_i is the measured signal. In practice,

the likelihood is first expanded in a truncated Taylor series and optimized using the gradient ascent method¹⁷ to get the update step:

$$\Delta\mu_j = -\frac{\frac{\partial L}{\partial \mu_j}}{\sum_h \frac{\partial^2 L}{\partial \mu_j \partial \mu_h}} \quad 4.2$$

where ‘ h ’ represents an image pixel. Using the model of the expected signal \hat{y}_i in Eq. (4.1), the likelihood function L is updated to get the final iterative step for μ_j , as described in Refs. (10) and (14).

4.2.2 Image reconstruction in MVCT

We have used a TomoTherapyTM Hi Art-II MVCT in this study. Two phantoms were used: the RMI tissue characterization phantom [Gammex Inc., Middleton, WI, USA] of 33 cm diameter and the TomoTherapyTM ‘cheese phantom’ (30 cm diameter), as shown in Figs. 4.1(a) and 4.1(b) respectively. Several tissue equivalent plugs, as listed in Table 4.1, were used with the arrangements shown in Figs. 4.1(a) and 4.1(b). All the plugs are 2.8 cm in diameter except for two solid steel rods (2.7 cm diameter and 7.9 g/cm³ density), which are used to simulate metal implants. The phantoms were scanned in helical mode with a pitch=1. The 256x256 images reconstructed using the FBP method by the TomoTherapyTM MVCT (FBP-MVCT) system were obtained. These images were directly used as priors in the NMAR in one case.

For the second case, the MVCT images were first corrected using the IMPACT method (IMPACT-MVCT). The CT numbers in the FBP-MVCT

images were converted to attenuation coefficient maps (μ_{tissue}) at 1 MeV (roughly the average photon beam energy of the TomoTherapyTM MVCT)¹⁸ using the following equation.

$$CTnumber = \frac{\mu_{tissue} - \mu_{water}}{\mu_{water}} \times 1000 \quad 4.3$$

In this equation μ_{water} at 1 MeV is used to convert the CT number to μ_{tissue} . The μ_{tissue} value was then used as an initial image in the IMPACT method. The measured signal by TomoTherapyTM MVCT detectors was converted to a pseudo axial fan beam format using 2π linear interpolation. This was normalized to an air signal and then used in the IMPACT method. Since the phantoms were scanned using the same clinical protocol as used for patients, the noise level in the phantom images is similar to that expected in clinical patient images.

For the image reconstruction using IMPACT, the incident photon spectrum was calculated at the isocenter (85 cm SAD) of the MVCT using the BEAMnrc¹⁹ and BEAMdp²⁰ Monte Carlo codes. The spectrum was validated in Ref. 14 using transmission measurements. Twenty spectral energy bins and eight base materials [air, lung, adipose, water, soft bone, cortical bone (as defined by ICRU 44)²¹, titanium and iron] were used. The energy dependent linear attenuation coefficients of these materials were obtained from the NIST website.²² The final 256x256 image is obtained after 150 iterations, as used in Ref. 14. The corrected μ_{tissue} distribution was converted back to CT numbers using the average value of μ_{water} in the IMPACT reconstructed image of the RMI phantom without

metal. These IMPACT-MVCT images were also used as priors in the NMAR method.

4.2.3 Image reconstruction in kVCT

The phantoms were scanned on a Philips Brilliance 16-slice Big Bore CT scanner [Philips Healthcare System, Cleveland, OH, USA] in axial mode with the following settings: 140 kVp, 400 mAs, 16 x 1.5 mm² collimation, and 1 s rotation time. An air scan is also obtained to normalize the raw sinogram of the phantoms.

Using the filtered backprojection (FBP) method, a 571x571 image with 38.7 cm field of view (FOV), matching the FOV of the MVCT images, was reconstructed in MatLabTM [The MathWorks Inc., Natick, MA, USA]. The axial scanning mode was used for simplicity of image reconstruction within MatLabTM. The normalized sinogram was first converted from the fan-beam to parallel beam geometry using the built-in “fan2para” function. The inverse Radon Transform, with Ram-Lak filter and linear interpolation (MatLabTM function “iradon”), was then used to reconstruct images from the parallel beam sinogram that covered the chosen FOV. The average pixel value for the pure liquid water plug in the image of the RMI phantom without metal was used to convert the image pixels into the CT numbers using Eq. (4.3). We call this method FBP-kVCT. We have just installed modified software in the CT scanner that extends the CT number scale to 16-bits and also reduces the metal artifacts in CT images of the pelvic region containing hip prostheses using the orthopaedic metal artifact reduction (OMAR)

algorithm. These images, corrected by the scanner itself, will be called “OMAR corrected images”.

4.2.4 NMAR with kVCT prior

The NMAR method requires a prior image for the sinogram normalization step. In our case, a kVCT prior image is obtained as follows. Firstly, the image is reconstructed using FBP in the presence of metals. The image is then segmented to obtain a metal only image using simple thresholding (>3000 HU as used in Ref. 6). The metal only image is forward projected (MatLabTM function “radon”) to identify the location and the projection data of metal in the raw sinogram. The raw data in these locations is replaced using linear interpolation in the detector channel direction from the surrounding data. This modified data is used to reconstruct an image using the FBP method as described in previous section 4.2.3 (MatLabTM function “iradon”). The metal is placed back into the reconstructed image from the metal only image. Secondly, in the tissue classification step, a chosen constant value of -1000 Hounsfield Units (HU) is assigned to pixels <-500 HU, a value of 0 HU is assigned to pixels -500 to 500 HU and pixels >500 HU are left unchanged.^{5,6} This is the final prior image. This prior image is forward projected to get a prior sinogram which is used to divide the original raw parallel beam sinogram pixel-wise to obtain the ratio projection sinogram. In the already identified regions that contain the projections through the metal, the ratio projection values are replaced from the surrounding pixels using linear interpolation in the detector channel direction. The ratio sinogram, after

interpolation, is denormalized by multiplying with the prior sinogram. An image is reconstructed from this denormalized sinogram using the FBP method (MatLab™ function “iradon”), and the metal only image is reinserted to get the final corrected image.

4.2.5 NMAR with MVCT priors

We obtained two different prior images from MVCT for each of the phantoms discussed in section (4.2.2). One is obtained from FBP-MVCT and the other from IMPACT-MVCT. Both of these images are first converted to pseudo kVCT images using the CT number conversion table and linear interpolation.

The calibration table is obtained as follows. Two images of the RMI tissue characterization phantom were obtained for each of the three methods: FBP-MVCT IMPACT-MVCT, and FBP-kVCT. In the first image, the phantom contained the various calibration inserts listed in Table I and two additional metal calibration plugs [titanium (density 4.59 g/cm³) and steel (density 7.9 g/cm³)]. These metal rods of 1.27 cm diameters were embedded in the 2.8 cm, outer diameter solid water inserts for the metal calibration. The particular choice of lesser diameter size (1.27 cm is equal to half an inch) for metal inserts is chosen by Gammex [Gammex Inc., Middleton, WI, USA] that manufactures RMI tissue characterization phantom. Smaller diameter should have been chosen to minimise the effect of variation of CT number within the metal insert (to reduce cupping artifact). In the second image, the metal calibration inserts were replaced with solid water inserts. The average CT number in the region of interest (ROI) within

each insert is calculated. The image with metal inserts is used only to get the average CT numbers of steel and titanium, whereas the average CT number for the remaining tissue inserts are obtained from the image without metals. Thus the calibration curves of FBP-MVCT vs FBP-kVCT, and IMPACT-MVCT vs FBP-kVCT, are used to scale the corresponding MVCT images of the phantoms containing large solid steel rods (2.7 cm diameter) into equivalent, pseudo kVCT prior images.

The equivalent kVCT prior images are resized to 571x571 pixels (using MatLab™ function “imresize” with “bilinear” interpolation) to match the kVCT matrix. Further, the image is translated and rotated, if required, to match the steel rod inserts with the corresponding inserts in the FBP-kVCT image. These prior images are directly used, without any tissue classification, to get the sinogram for normalization and denormalization after the interpolation step in the NMAR algorithm, as described above. The final corrected images, with two large steel rods (i.e., 2.7 cm diameter) at the peripheral plugs of the phantoms, are analyzed both qualitatively and quantitatively by comparing the profiles through the various regions of the image.

4.2.6 Dosimetric evaluations

The TomoTherapy™ 'cheese phantom' is used for dosimetric comparisons of the methods since a film can be placed inside it, and the delivered dose can be measured. A radiotherapy treatment plan is created on the Eclipse treatment planning system for a Varian Clinac 2100 EX linac [Varian Medical Systems,

Palo Alto, CA, USA] and the same plan is applied to all three NMAR corrected images (two with MVCT priors and one with kVCT prior). Two 6 MV, 5 x 10 cm² lateral parallel opposed fields (i.e., 90⁰ and 270⁰ gantry positions) are applied through the centers of the steel inserts with an irradiation setting of 280 monitor units (MUs) for each field. The dose distribution is calculated using the Anisotropic Analytical Algorithm (AAA) version 10.0.25 with heterogeneity correction. AAA is commissioned using routine clinical procedure²³ and no particular modifications related to heterogeneity corrections are allowed in the system. The CT number to density calibration tables extended for metals (titanium and steel) are used. The FBP-kVCT image of the phantom without the steel inserts is taken as the "gold standard" for comparison. The fixed CT number of steel is patched (i.e., substituted) in the image for the corresponding metal regions and the above treatment plan is applied. This image thus contains the correct CT numbers for the tissue as well as the metal. The calculated dose in this reference image is first compared with dose measured using a GAFCHROMIC® EBT2 film [Ashland, Covington, KY, USA]. The methodology of the dose measurement using these films is described in the next paragraph below. The film is placed at the center of the phantom in a vertical plane perpendicular to the beam directions. Finally, the calculated dose distributions in the other corrected images (NMR with FBP-MVCT, IMPACT-MVCT and FBP-kVCT priors) of the phantom containing the steel rods are compared with the dose distribution in the reference image.

Since gafchromic film response is considered to be nearly independent of the energy spectrum (GAFCHROMIC® EBT2 manual), the calibration procedure

routinely used for TomoTherapyTM was employed. This procedure consists of placing the film with 1.5 cm of solid water build-up on top, and delivering a treatment resulting in 13 dose steps along the diagonal of the film. The same treatment is delivered for a second time with an ion chamber in the exact position where the highest dose step had been. Based on this ion chamber measurement the dose for the other 12 steps is recalculated accounting for any daily dose variations. The film is left over night to get developed and then digitized. The digitized film is then opened in MatLabTM and the grey values for a square of pixels (3x3) are averaged in the centre of each dose step. A graph of dose vs. grey value is obtained with 14 points (the 13 dose steps and 1 background assumed to be zero dose). These points are fitted with a 3rd degree polynomial that yields the calibration curve. Once this polynomial is obtained any grey value can be converted into dose. The dose used in this study is within the dose range used in the calibration curve.

To get a realization of a clinical scenario, an optimized “four field plan” is created on the reference image with 5x10 cm² fields. Two clinical plans: “a rapid arc” and “a seven field IMRT” optimized for two different prostate patients are applied (as a verification plan) to all the corrected images to re-calculate the dose. These three plans are also applied to the OMAR corrected image and the re-calculated dose distributions are compared to the calculated dose distribution in the reference image. A 6 MV beam is used in all the cases.

4.3 Results

4.3.1 Image reconstructed using kVCT prior

Figure 4.1 shows the phantoms [Figs. 4.1(a) and 4.1(b)] used in the experiment with the bilateral steel rods (indicated by the arrows). The corresponding FBP-kVCT images have the steel rods replaced by solid water [Figs. 4.1(c) and 4.1(d)]. The physical density and the electron density relative to water of these inserts are listed in Table 4.1. Figure 4.2(a) shows the FBP-kVCT image of the RMI phantom in Fig. 4.1(a) with steel rods which contains severe streaking and shading. These artifacts are greatly reduced in the final NMAR reconstructed image [Fig. 4.2(b)] that uses the kVCT prior image of Fig. 4.2(d). The FBP image obtained using the regular PC method with linear interpolation is shown in Fig. 4.2(c), which is tissue classified to get the kVCT prior image [Fig. 4.2(d)].

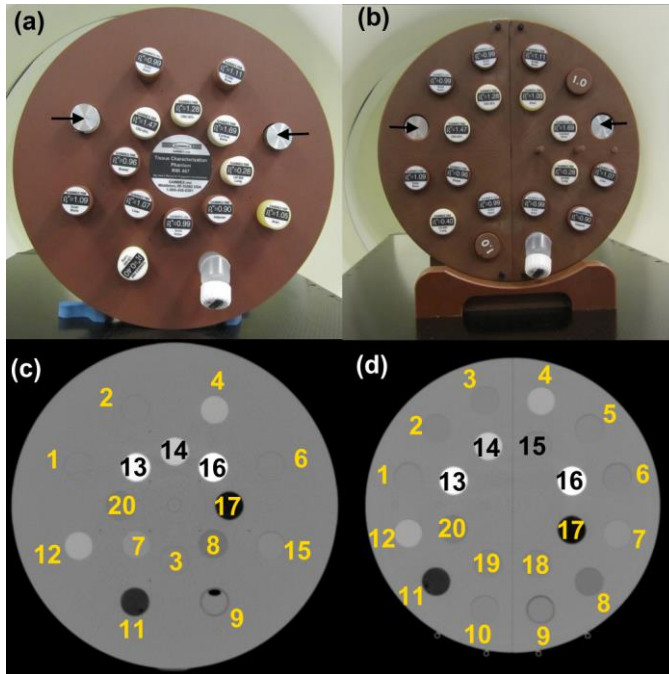


Figure 4.1. (a) RMI tissue characterization phantom and (b) TomoTherapy™ cheese phantom; kVCT images of (a) and (b) without metal plugs in (c) and (d) respectively. The physical properties of the inserts used are listed in Table 4.1. Either the steel inserts [indicated by arrows in (a) and (b)], or water equivalent plugs were inserted in positions ‘1’ and ‘6’ to simulate a bilateral metal implant or artifact free images. The window width/level of the CT images is 1500/0 HU.

Table 4.1. Physical density and electron density relative to water of the inserted plugs shown in Fig. 4.1.

Label #	Inserts	Physical density (g/cc)	Electron density relative to water
1, 2, 3, 6, 18 and 19	Solid water	1.018	0.989
5 and 10	Solid water (cheese phantom)	~1.0	~1.0
7	Liver	1.094	1.062
8	Adipose	0.941	0.924
9	Water	1.0	1.0
11	Lung (LN-300)	0.30	0.295
12	Inner bone	1.144	1.097
13	CB2-50% (CaCO ₃)	1.560	1.470
14	CB2-30% (CaCO ₃)	1.334	1.279
15	Brain	1.094	1.062
16	Cortical bone	1.823	1.695
17	Lung (LN-450)	0.46	0.445
20	Breast	0.979	0.956

Most of the inserts including steel in the corrected image [Fig. 4.2(b)] are deformed (arrows indicate the worst cases), in addition to the remaining shading and secondary streakings. Importantly, the CB2-50% bone equivalent (location 13), the cortical bone (location 16) and the lung inserts (location 17) are deformed the most. These tissues have among the larger deviations in CT numbers from the CT number of water. When the first projection completion is made, the interpolation step incorrectly replaces the attenuation information corresponding to these tissues [bone and lung] in the rays that also pass through the metal. This creates the secondary artifacts (blurring or clipping) at the edges of these structures [see Fig. 4.2(c)] which are not removed during the tissue classification/segmentation step, as indicated by arrows in the image in Fig. 4.2(d). In the tissue classified prior image [Fig. 4.2(d)], these information losses are intact. Further, the segmentation/tissue classification step is also non optimal and parts of the structures are misclassified [e.g. lung insert (LN-300) at location 11, and CB2-50% bone equivalent insert at location 13]. This can be seen from the erosion at the edges and within the regions of these tissues in Fig. 4.2(d). Although first reconstructing using the general PC method is helpful to regain the lost soft tissue information between the metal inserts (which would otherwise be classified as air) in the original FBP image [Fig. 4.2(a)], some of the secondary artifacts introduced are passed to the final image via the prior image.

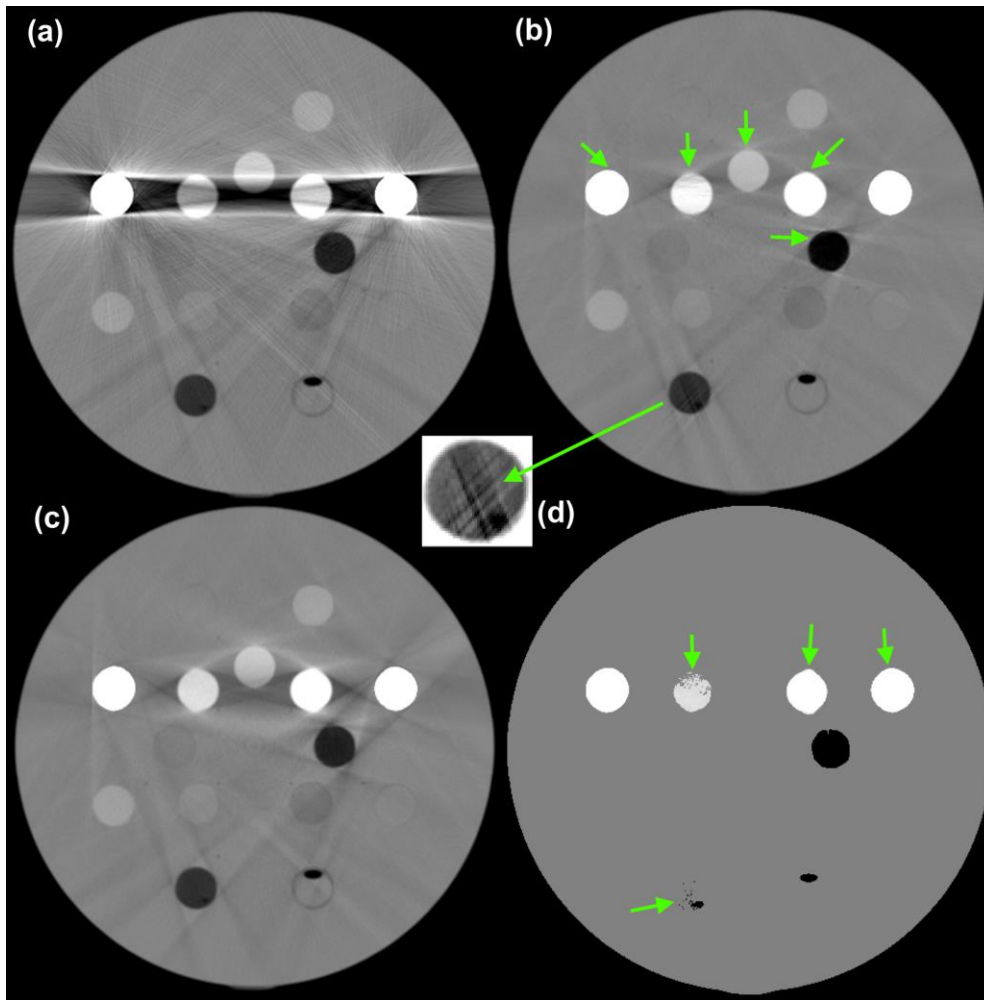


Figure 4.2. Original FBP reconstructed image of the RMI phantom (a) after correction with NMAR method with kVCT prior (b). The image corrected by the regular PC method with linear interpolation (c) is segmented to provide the prior image (d) for NMAR. The arrows show distorted edges and eroded regions of the structures in the prior and final corrected images. Image window width/level is 1500/0 HU. The inset shows the degraded area inside the lung insert (location 11) for a different (500/-500 HU) window width/level.

Figure 4.3 shows the profiles through various regions of the corrected image in Fig. 4.2(b), which are compared with the corresponding profiles in the reference image. The reference image is the “gold standard” image, described in section (4.2.6), patched with the fixed CT number for the steel rods. The loss of edge information for the structures in the corrected image can be clearly seen (indicated by arrows). The CT number in most of the pixels within and at the

edges of the inserts (bone and lung) in the corrected image fluctuates and deviates from the corresponding CT number in the artifact free reference image [Fig. 4.3(a-c)]. A large variation in CT number (a "cupping artifact") can be seen inside the steel inserts in the corrected image [see Fig. 4.3(d)] that differ from the calibrated values in the reference image. A large variation in CT number within a solid cylinder provides incorrect information of electron density information.

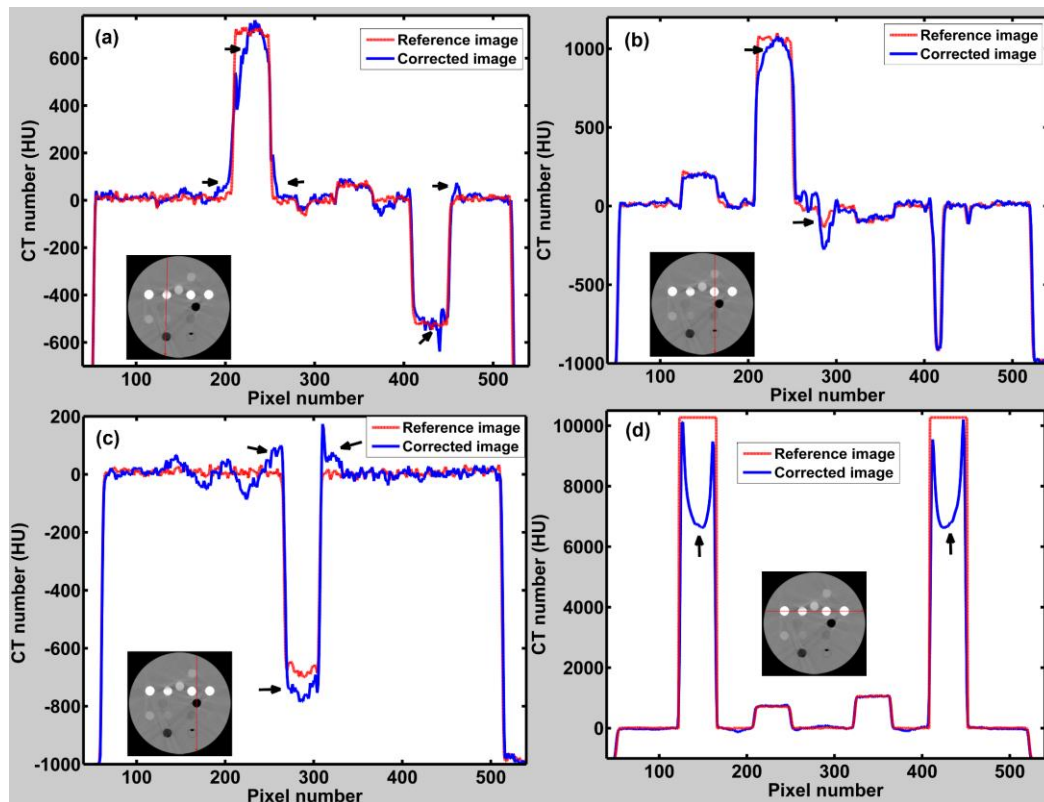


Figure 4.3. Profiles through various sections of the corrected image in Fig. 4.2(b) compared with the corresponding profiles in the reference image. Arrows indicate the deformed edges, eroded regions, and large deviation of CT number within the inserts in the corrected image. The fluctuations are predominant in lung, bone and metal inserts. Inset in each panel shows the line in the image along which the profile is taken.

4.3.2 Images reconstructed using MVCT priors

Figure 4.4 shows the original FBP [Fig. 4.4(a)] and IMPACT reconstructed MVCT images [Fig. 4.4(b)] of the RMI phantom, their pseudo

kVCT counterparts [Figs. 4.4(c) and 4.4(d)] or the prior images, and the final corrected kVCT images [Figs. 4.4(e) and 4.4(f)] using these priors. Compared to the original FBP image in Fig. 4.2(a), the streaking and shading in both the corrected images [Figs. 4.4(e) and 4.4(f)] are largely reduced and the various inserts are more clearly visible. In the prior image without correction [Fig. 4.4(c)], there is a faint shading of lower CT number connecting the steel inserts. This shading causes a similar light shadowing to appear in the final corrected image in Fig. 4.4(e). In the IMPACT reconstructed prior image [Fig. 4.4(b)] and hence on the final corrected image [Fig. 4.4(f)], this shading is absent. Although in both of these images there are some remaining faint streaks originating from the metal inserts, the edge information of the structures are almost intact. These streaks are due to the greater noise present in the MVCT prior images. Almost all the inserts, including the metal ones, are circular. There are no eroded regions within the inserts.

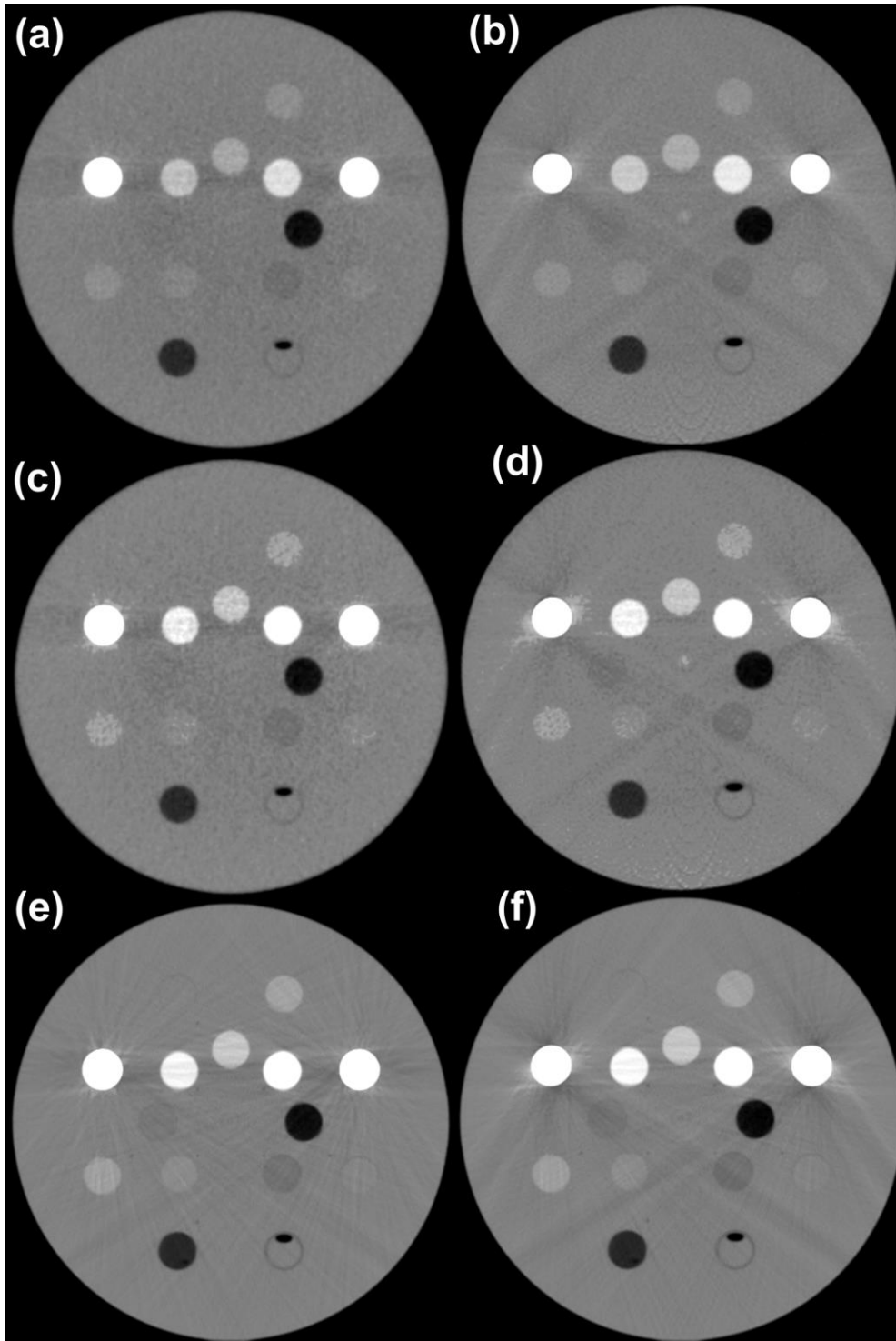


Figure 4.4. (a) Original FBP reconstructed MVCT image of the RMI phantom (b) after correction using modified IMPACT method. The transformed pseudo kVCT images (c) and (d) from images (a) and (b), respectively, are used as prior images in NMAR technique to reconstruct images (e) and (f) in kVCT. Most of the inserts in (e) and (f) are not deformed and clearly visible. However, there are remaining subtle streaks and shadings that have passed from the prior images. Image window width/level is 1500/0 HU.

Figures 4.5 and 4.6 show the profiles corresponding to Fig. 4.3, for the images in Figs. 4.4(e) and 4.4(f), each compared against the profiles in the reference image. The profiles through the corrected image using MVCT priors are nearly identical to the corresponding profiles in the reference image for all the inserts. Although the profiles are noisier inside the inserts, the edges are intact in the corrected image. One striking difference is in the profile through the steel inserts compared to the profile in Fig. 4.3(d). The CT number within the steel inserts is almost constant and very close to the reference value.

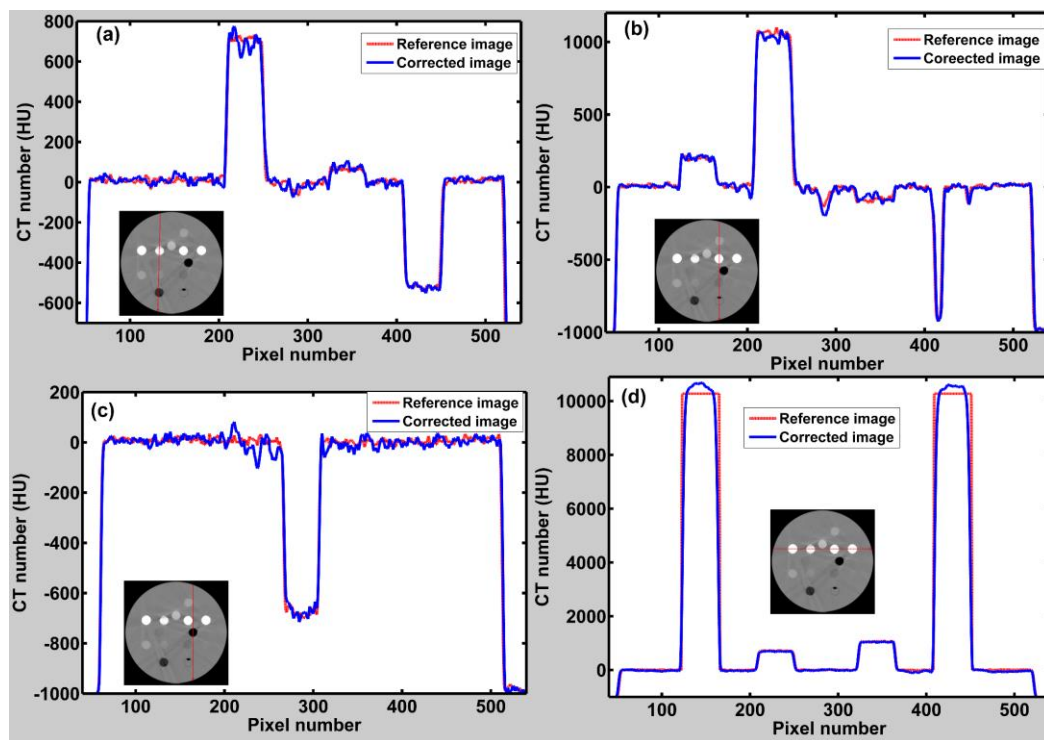


Figure 4.5. Profiles through various regions of the image in Fig. 4.4(e) corresponding to Fig. 4.3. The profiles in the corrected image are very close to the corresponding profiles in the reference image for all the inserts including metal. Although the profiles are noisier inside the inserts, the edges are intact in the corrected image. Inset in each panel shows the line in the image along which the profile is taken.

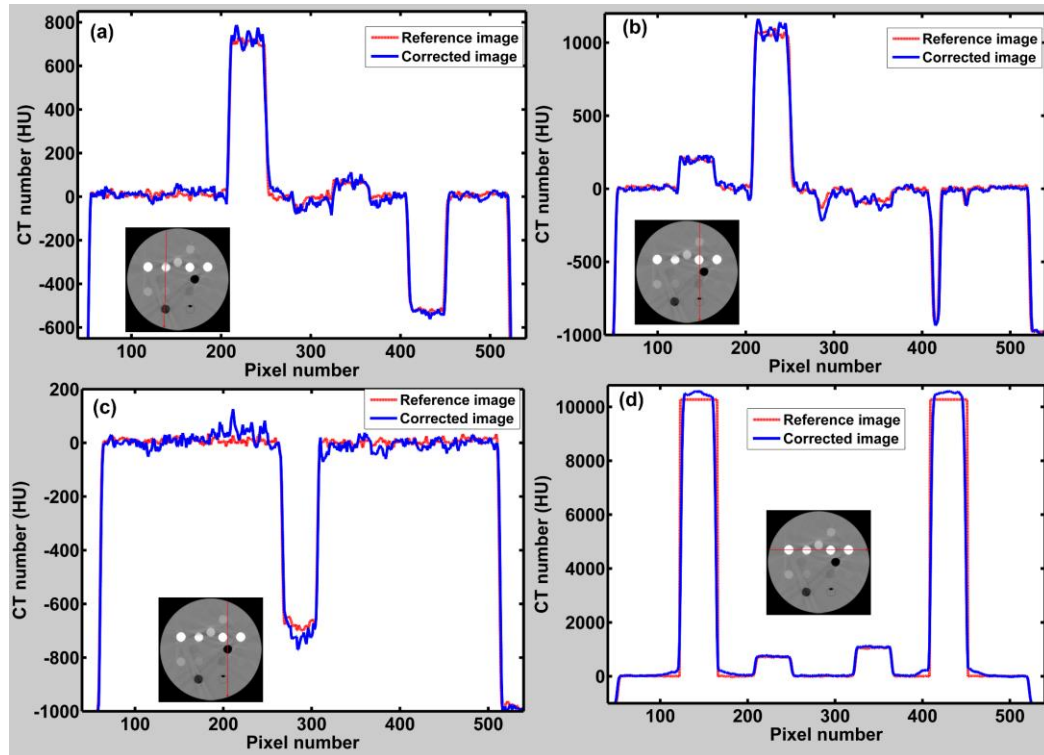


Figure 4.6. Profiles through various regions of the image in Fig. 4.4(f) corresponding to Fig. 4.3. The profiles in the corrected image are very close to the corresponding profiles in the reference image for all the inserts including metal. Although the profiles are noisier inside the inserts, the edges are intact in the corrected image. Inset in each panel shows the line in the image along which the profile is taken.

4.3.3 Images reconstructed using a commercial algorithm

The OMAR corrected image (512x512) of the RMI phantom is shown in Fig. 4.7. The severe streaking and shading present in the image before correction [Fig. 4.2(a)] are greatly reduced in the OMAR corrected image. However, residual shading and new secondary artifacts are present in Fig. 4.7. Many inserts in the image are deformed which are indicated by the arrows.

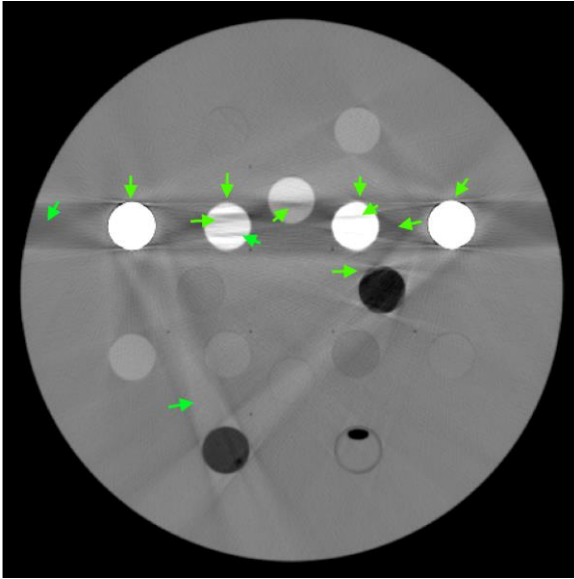


Figure 4.7. Image of the RMI phantom corrected by the OMAR algorithm in the Philips CT scanner. The arrows show distorted edges and eroded regions of the structures in the image. Image window width/level is 1500/0 HU.

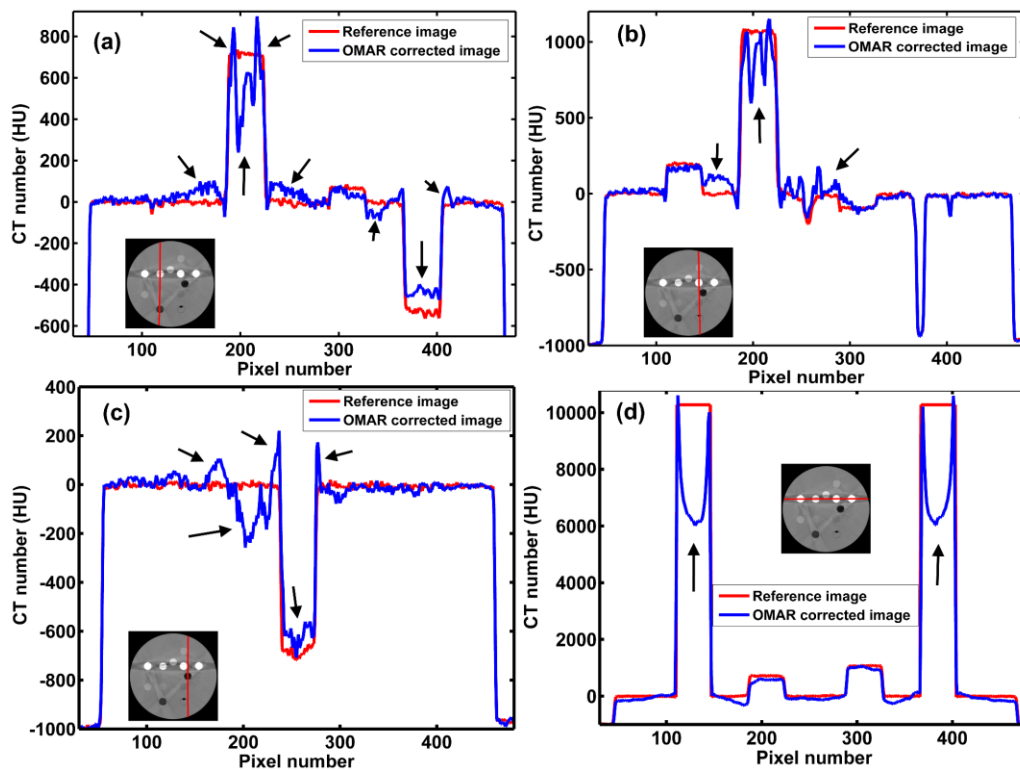


Figure 4.8. Profiles through various regions of the image in Fig. 4.7 compared with the reference image. Arrows indicate the deformed edges, eroded regions, and large deviation of CT number within the inserts in the corrected image. The fluctuations are predominant in lung, bone and metal inserts. Inset in each panel shows the line in the image along which the profile is taken.

The CB2-50% bone equivalent (location 13), the cortical bone (location 16) and the lung insert (location 17), which have a larger deviation of CT number from the CT number of water, are deformed the most. These inserts were also deformed in the kVCT-NMAR reconstructed images in Fig. 4.2(b). However, unlike the erosion from one side in the kVCT-NMAR images, there is erosion within large regions of the inserts (bone and lung equivalent inserts) in the OMAR corrected image in the direction connecting the steel inserts. There is a residual dark shadow that connects the steel rods. There are additional bands of lighter shadow that originate from the steel inserts.

Figure 4.8 shows the profiles through various regions of the corrected image in Fig. 4.7 which are compared with the corresponding profiles in the reference image. The reference image in this case is the CT scanner's reconstructed image of the phantom in which the steel rods are replaced by solid water plugs. The average CT number of steel is artificially inserted in the location of these solid water plugs in the reference image. The loss of edge information for the structures and the fluctuation of CT number due to the remaining/secondary artifacts in the corrected image are indicated by arrows. The CT number in most of the pixels within and at the edges of the inserts (bone and lung) in the corrected image fluctuates and deviates from the corresponding CT number in the artifact free reference image [Fig. 4.8(a-c)]. The amplitude of these fluctuations is larger in bone inserts (locations 13 and 16) in comparison to the corresponding profiles

in Fig. 4.3. The large "cupping artifact" similar to the one in Fig. 4.3(d) can be seen inside the steel inserts in the corrected image.

4.3.4 Dosimetric evaluations

Figure 4.9 shows the dose distributions computed on (a) the reference image, (b) the image corrected using IMPACT corrected MVCT prior, (c) the image corrected using FBP reconstructed MVCT prior, and (d) the image corrected using kVCT prior. The isodose lines (325, 310, 250, 210, 190 and 150 cGy) are shown in the transverse isocentric plane. The isodose lines in Fig. 4.9(b), and Fig. 4.9(c) are quite similar to the corresponding lines in the reference image but are slightly shrunk (i.e., increase in the calculated dose) in the region between the steel inserts. However, a large dissimilarity in dose distribution can be observed between image 4.9(a) and the image corrected using kVCT prior [Fig. 4.9(d)]. The innermost isodose line (190 cGy) is not visible in Fig 4.9(d). The dose measured by gafchromic film at the isocenter of the fields is 165.5 cGy whereas the calculated dose in the reference image at the same point is 171.2 cGy, which is about 3.4% different. The estimated dosimetric uncertainty of the gafchromic film measurement is about 2%. This estimate is based on the average difference in the measured dose (by an ion chamber) from the corresponding dose predicted by the calibration curve. The uncertainty depends on various factors such as the digitization method used, scanner properties, color channel selection, film orientation e.t.c.²⁴ Our single channel (Red channel) method does not make

uniformity correction. The uncertainty resulting due to the variation of film grains increases the magnitude of this uncertainty.

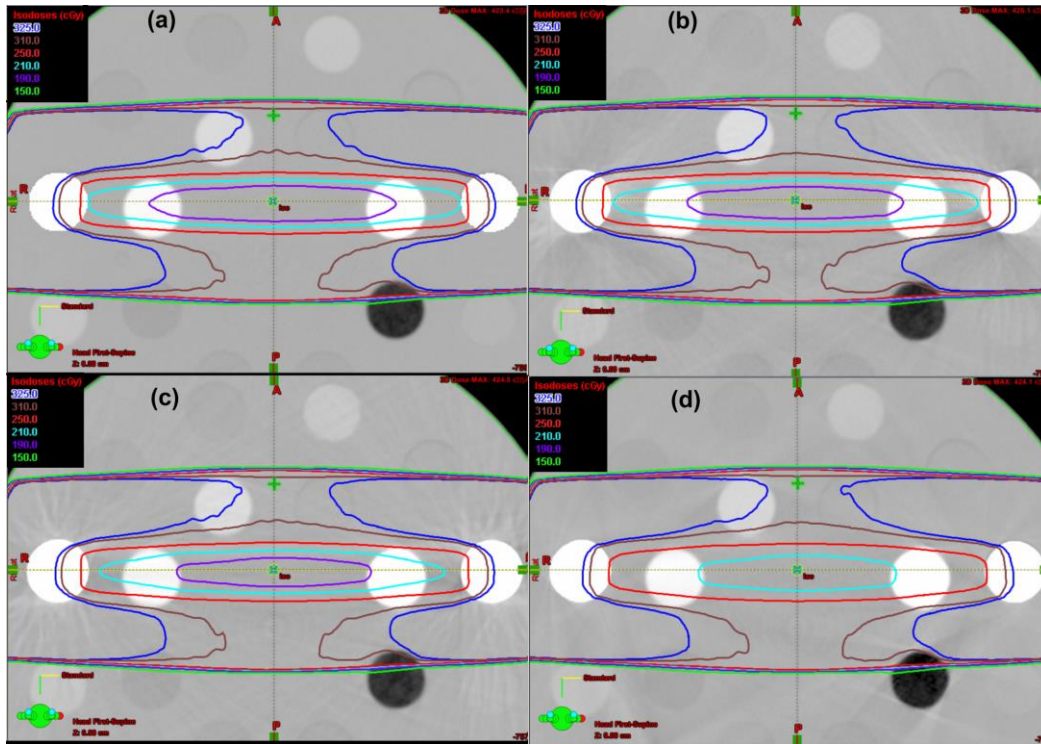


Figure 4.9. Comparisons of dose distributions for 6 MV 5 x 10 cm² parallel opposed fields calculated on (a) the reference image, (b) the image corrected using an IMPACT corrected MVCT prior, (c) the image corrected using a FBP reconstructed MVCT prior, and (d) the image corrected using a kVCT prior. The irradiation setting for both the fields is 280 MU. The image window width/level is 1500/0 HU.

The calculated dose at the isocenter in the image corrected using IMPACT-MVCT prior is 175.8 cGy, which is 2.7% higher than the calculated dose in the reference image. Similarly, the dose at the isocenter in the FBP-MVCT prior corrected image (180.1 cGy) is ~ 5% higher than the corresponding dose in the reference image. The calculated dose at the same point in the corrected image using kVCT prior (197.8 cGy) is about 15.5% higher than that of the reference image. In addition, the light shadow in the lower half of Fig 4.4(f)

caused only a 0.2% dose difference compared to the reference image for a single, posterior 6 MV beam.

The comparison of the calculated dose profiles on the isocenter plane along the line perpendicular to the line joining the steel inserts for both the corrected and the reference image patched with steel inserts is shown in Fig. 4.10(a). The dose profiles in the corrected images using MVCT priors are closer to the reference image dose profile in comparison to the corresponding dose profile in the image corrected using the kVCT prior. The deviation of the dose is larger in the central pixels that fall in the ‘shadow’ of the steel inserts. The cupping artifact [see Fig. 4.3(d)] inside the steel inserts provides lower electron density incorrectly, especially towards the center of the inserts. This creates lower attenuation for the beams, and higher doses are observed towards the center of the beam. The image corrected with the IMPACT-MVCT prior has the closest matching dose profile to the reference image. The existing difference between the reference image and the images corrected with an MVCT prior is due to the difference in the density at the edges of steel rods [Figs. 4.5(d) and 4.6(d)]. Due to the larger partial volume effects in the MVCT images (256x256 images compared to 571x571), the edge pixels of the steel inserts have lower CT numbers compared to the theoretically assumed values in the reference image. In the uncorrected MVCT prior image, the existing shadow connecting the metal further lowers the CT numbers. Due to this the dose difference is slightly higher for the image using uncorrected MVCT prior image. However, the maximum difference in the dose is less than 5% and decreases to 2.7% when using corrected MVCT prior image.

Figure 4.10(b) shows the profile in Fig. 4.10(a) for the reference image patched with metal compared with the corresponding measured dose using gafchromic film. The profiles are close to each other except at the center and at regions indicated by arrows. There is inherent experimental uncertainty in the film dose measurement. The dose calculated by the Eclipse treatment planning system in the presence of metal could also be non optimal. Although a comparison to a Monte Carlo calculation might be more definitive, it is beyond the scope of this study.

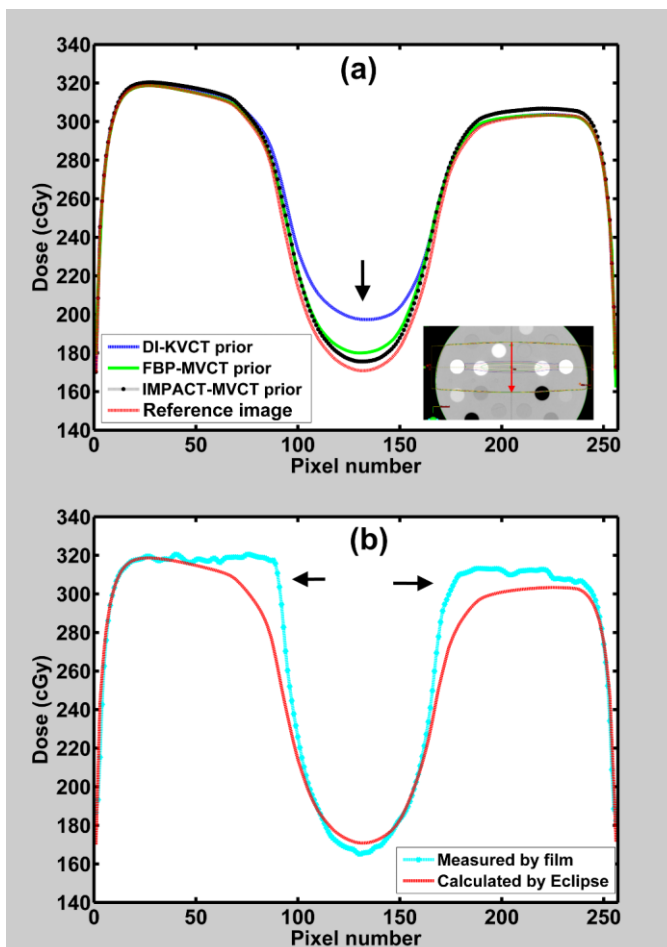


Figure 4.10. (a) Variation of calculated dose within the 10 cm width of the beams at the isocentric plane of the images in Fig. 4.9. The arrow shows the point of largest dose difference relative to the dose in the reference image. The arrow in the inset image shows the location and direction of the profiles in the image. (b) The calculated dose profile of the reference image is compared with the measured dose measured using gafchromic film.

4.3.5 Dosimetric evaluations of clinical plans on phantom images

The optimized four field plan (Relative weights: AP = 0.5, PA = 0.34, and Laterals = 0.1) created on the reference image is shown in Fig. 4.11(a). The planned target dose at the isocenter is 200 cGy.

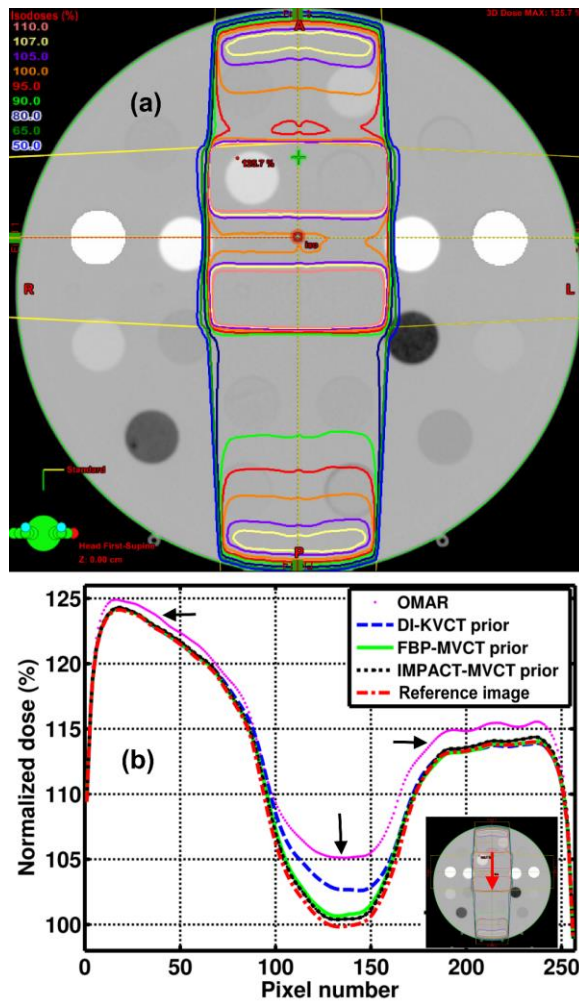


Figure 4.11. (a) The calculated dose distribution of a four field plan in the reference image. (b) The calculated dose profiles along the arrow shown in the inset for various metal artifact corrected images relative to the reference image.

Figure 4.11(a) shows the distribution of isodose lines in the reference image. The comparison of the dose profiles for various artifact corrected images, normalized to the isocenter dose in the reference image, is shown in Fig. 4.11(b). The dose

profile for the OMAR corrected image has the largest deviation from the reference image. This is due to the remaining dark shadow connecting the steel rods, large erosion within the bone inserts and the large “cupping artifact” inside the steel rods in the image. The calculated dose at the isocenter in the OMAR corrected image is 5.2% higher than that in the reference image. Similarly, the calculated dose at the same point in the images corrected using kVCT prior, FBP-MVCT prior and IMPACT-MVCT prior is, respectively, about 3%, 0.8% and 0.4% higher than that in the reference image. The gamma evaluation on the normalized dose distribution (with respect to planned 200 cGy dose at the isocenter) shows the largest percentage of voxels (82.7%) passing an acceptance criteria of 2%/2.5mm in the image corrected using IMPACT-MVCT prior in comparison to FBP-MVCT prior (82.5%), kVCT prior (69.2%), and in the OMAR corrected image (58.5%).

The comparison of the dose distributions resulting from the re-calculation of a rapid arc and a seven field IMRT plan on the images of the phantom is shown in Fig. 4.12. The plans were previously optimized using the patient images and contours in each case, and then simply copied to the various phantom images for re-calculation of dose. The left column in Fig. 4.12 (panels a, b, c, d, e) is the rapid arc plan whereas the right column (panels f, g, h, i, j) is the seven field IMRT plan (gantry positions at 0, 55, 105, 135, 225, 255, and 305 degrees). The rows in both the columns beginning from the top are the plans on the reference image (a, f), the IMPACT-MVCT prior corrected image (b, g), the FBP-MVCT prior corrected image (c, h), the kVCT prior corrected image (d, i), and the

OMAR corrected image (e, j), respectively. The grid size displayed in the images is 1 x 1 cm².

In Fig. 4.12, the distribution (shape and the spatial extent) of isodose lines in the corrected images using the MVCT priors (second and third rows) is very close to the reference image (first row). The images corrected with the kVCT prior and using OMAR show larger deviations of isodose lines compared to the reference image. The image corrected with the IMPACT-MVCT prior shows the closest, and OMAR corrected image show the farthest match of the dose distribution to the reference image.

In the rapid arc plan, the 95%, 100% and 105% isodose lines expand and cover larger regions in the images corrected using kVCT prior [Fig. 4.12(d)] and the OMAR [Fig. 4.12(d)] compared to the plan in the reference image [Fig. 4.12(a)]. In these images, there are new areas with 105% dose which are not present in the reference image. These changes are seen most pronounced in the OMAR corrected image. The 105% isodose lines cover larger areas in the OMAR corrected image and there is a small region of 107% isodose line. All these areas of changed dose distribution with respect to the reference image are indicated by arrows in Fig. 4.12. In the gamma analysis, the largest percentage of voxels (99.2%) pass an acceptance criteria of 2%/2.5mm in the image corrected using IMPACT-MVCT prior in comparison to FBP-MVCT prior (99.2%), kVCT prior (98.6%), and in the OMAR corrected image (88.9%).

In the seven field IMRT plan, the 90%, and 95% isodose lines show a pronounced change among the images. Similar to the rapid arc plan, the isodose

lines are expanded and cover larger regions in the images corrected using kVCT prior [Fig. 4.12(i)] and OMAR [Fig. 4.12(j)] compared to the isodose lines in the reference image [Fig. 4.12(f)]. These changes are seen most pronounced in the OMAR corrected image (shown by arrows). The gamma analysis shows 99.3% of the voxels pass an acceptance criteria of 2%/2.5mm in the image corrected using IMPACT-MVCT prior compared to FBP-MVCT prior (98.8%), kVCT prior (88.2%), and in the OMAR corrected image (82.3%).

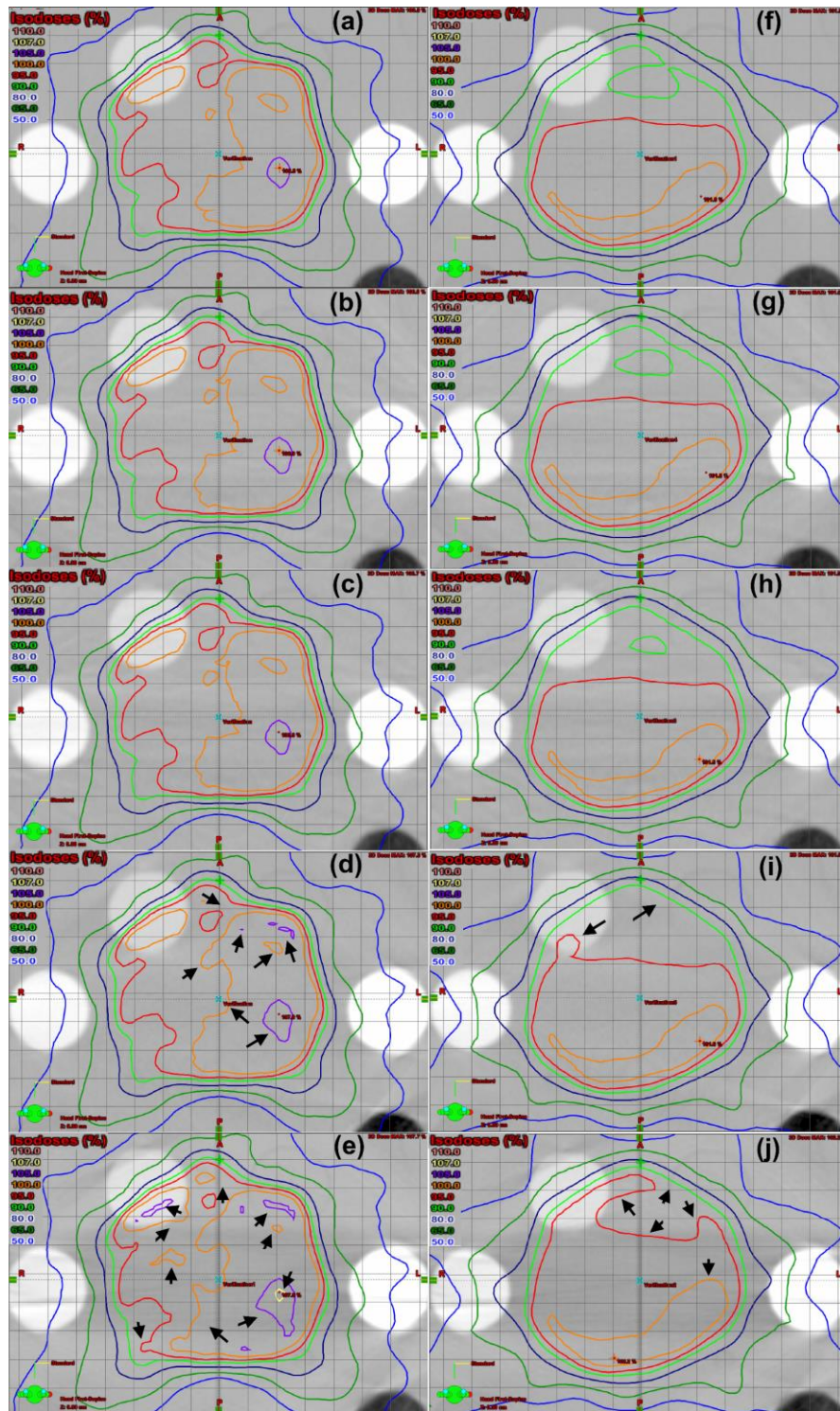


Figure 4.12. Comparisons of dose distributions for a rapid arc plan (a-e) and a seven field IMRT plan (f-j) optimized for prostate patients calculated on (a, f) the reference image, (b, g) the image corrected using an IMPACT corrected MVCT prior, (c, h) the image corrected using a FBP reconstructed MVCT prior, (d, i) the image corrected using a kVCT prior, and (e, j) the OMAR corrected image. The doses are normalized to a prescription dose of 200 cGy at the isocenter for both the plans. The image window width/level is 1500/0 HU.

4.4 Discussion

Most of the published metal artifact reduction methods focus on improving the visibility of structures in diagnostic CT images. Due to the excessive beam hardening and photon starvation caused by metal, the CT numbers of reconstructed metal pixels in the initial FBP images are incorrect. In these methods, the metal segmented from the initial FBP image is replaced back in the final, corrected image. The electron density in the implants in these images is generally incorrect, and it must be overridden, either from a priori knowledge or from data in an MVCT scan. The composition of the metal in the implants is generally not available *a priori*. For the application of CT to radiation therapy planning, both the correct outline of organs and the accuracy of the CT numbers (and hence the electron density) in the images are important. The effectiveness of a particular metal artifact correction method in radiotherapy, thus, relies on the correctness of these two important aspects. MVCT imaging can generally reduce metal artifacts to a large degree and provide correct information on the location and composition of metals, but suffers from lower soft tissue differentiability. This study shows that an MVCT image can be used as a tool to obtain and transfer accurate information about metal implants, as well as improve visual clarity of the tissues in the kVCT image, provided a more accurate registration of MVCT and kVCT images. Registration errors can always introduce secondary artifacts in the corrected images. A systematic study to quantify those artifacts as a function of registration error is beyond the scope of this thesis. We used two MVCT images

without tissue classification to avoid segmentation errors: one without correction and the other corrected using the model based statistical method. The corrected images are thus better suited for radiotherapy.

There are remaining streaks in the corrected images using MVCT priors that originate from metal implants and these are distributed radially. The forward projection data of the MVCT prior image are noisy due to the inherently higher noise in MVCT. As these data are used for normalization/denormalization in NMR, the interpolated projection data in the regions corresponding to the projections through the metal become noisy compared to the rest of the data. The fluctuations at the edges of the interpolated data enhance these streaks.²⁵ In the MVCT image without correction, there is light shading connecting the metals which introduces similar light shadow in the corrected kVCT image. This shading can be nearly removed by using the corrected MVCT prior. There are a few secondary streaks in the corrected kVCT image, most probably due to the non optimal geometry of the MVCT system used in the IMPACT method.

Our study is limited to phantom images, and hence our method should be further investigated with patient data containing hip implants and dental filings. In general, the MVCT and kVCT systems are not available on the same gantry system, and therefore patient positioning differences between the two systems can create mismatch between the kVCT and MVCT priors. Particularly, the mismatch of high contrast structures (metallic objects, bone and air gaps) creates larger difference in the sinogram of prior which creates stronger secondary artifacts.

Further investigation using deformable registration between kVCT and MVCT images is needed.

Our MAR technique, that uses MVCT priors without tissue classification, has significantly improved the image quality and reduced the shading metal artifact without tissue deformation compared to the existing NMAR technique as well as the commercially available technique in the Philips CT scanner. Moreover, our technique has restored the correct electron density of metal. The radiation dose calculated in the images corrected by our method is closer to the dose in the reference image.

4.5 Conclusions

The use of MVCT images without tissue classification, both with and without artifact correction, as prior images greatly reduces the metal artifacts in kVCT without deforming the structures. The light streaks originating from the metals in the corrected images do not obscure the structures. The CT numbers for both the metal and the other tissue inserts are close to the reference image and the radiation doses calculated on these images are closer to the dose in the reference image (within 2.7% and 5%, respectively with the corrected MVCT and uncorrected MVCT priors). Although the kVCT prior creates far fewer streaks than the MVCT prior, the kVCT prior creates structural deformation, edge distortion, and large quantitative error in metal CT numbers. These result in large deviation (~15.5%) of the radiotherapy dose at the isocenter compared to the ground truth.

4.6 References

1. W. A. Kalender, R. Hebel, and J. A. Ebersberger, "Reduction of CT artifacts caused by metallic implants," *Radiology* **164**, 576-577 (1987).
2. M. Yazdi, L. Gingras, and L. Beaulieu, "An adaptive approach to metal artifact reduction in helical computed tomography for radiation therapy treatment planning: experimental and clinical studies," *Int. J. Radiat. Oncol. Biol. Phys.* **62**, 1224-1231 (2005).
3. M. Bal and L. Spies, "Metal artifact reduction in CT using tissue-class modeling and adaptive prefiltering," *Med. Phys.* **33**, 2852-2859 (2006).
4. W. Veldkamp, R. Joemai, A. Molen, and J. Geleijns, "Development and validation of segmentation and interpolation techniques in sinograms for metal artifact suppression in CT," *Med. Phys.* **37**, 620-628 (2010).
5. E. Meyer, R. Raupach, M. Lell, B. Schmidt, and M. Kachelriess, "Normalized metal artifact reduction (NMAR) in computed tomography," *Med. Phys.* **37**, 5482-5493 (2010).
6. E. Meyer, R. Raupach, M. Lell, B. Schmidt, and M. Kachelriess, "Frequency split metal artifact reduction (FSMAR) in computed tomography," *Med. Phys.* **39**, 1904-1916 (2012).
7. Metal Artifact Reduction for Orthopedic Implants (O-MAR). Philips HealthCare System 2012 [available URL: [http://clinical.netforum.healthcare.philips.com/us_en/Explore/White-Papers/CT/Metal-Artifact-Reduction-for-Orthopedic-Implants-\(O-MAR\)](http://clinical.netforum.healthcare.philips.com/us_en/Explore/White-Papers/CT/Metal-Artifact-Reduction-for-Orthopedic-Implants-(O-MAR))].
8. X. Zhang, J. Wang, and L. Xing, "Metal artifact reduction in x-ray computed tomography (CT) by constrained optimization," *Med. Phys.* **38**, 701-711 (2011).
9. Y. Zhang, L. Zhang, X. R. Zhu, A. K. Lee, M. Chambers, and L. Dong, "Reducing metal artifacts in cone beam CT images by pre-processing projection data," *Int. J. Radiat. Oncol. Bio. Phys.* **67**, 924-932 (2007).

10. B. De Man, J. Nuyts, P. Dupont, G. Marchal, and P. Suetens, "An iterative maximum-likelihood polychromatic algorithm for CT," *IEEE Trans. Med. Imaging.* **20**, 999-1008 (2001).
11. J. F. Williamson, B. R. Whiting, J. Benac, R. J. Murphy, G. J. Blaine, J. A. O'Sullivan, D. G. Politte, and D. L. Snyder, "Prospects for quantitative computed tomography imaging in the presence of foreign metal bodies using statistical image reconstruction," *Med. Phys.* **29**, 2404-2418 (2002).
12. K. V. Slambrouck, and J. Nuyts, "Metal artifact reduction in computed tomography using local models in an image block-iterative scheme," *Med. Phys.* **39**, 7080-7093 (2012).
13. S. Karimi, P. Cosman, C. Wald, and H. Martz, "Segmentation of artifacts and anatomy in CT metal artifact reduction," *Med. Phys.* **39**, 5857-5868 (2012).
14. M. R. Paudel, M. Mackenzie, B. G. Fallone, and S. Rathee, "Evaluation of metal artifacts in MVCT systems using a model based correction method," *Med. Phys.* **39**, 6297-6308 (2012).
15. R. L. Siddon, "Fast calculation of the exact radiological path for a three-dimensional CT array," *Med. Phys.* **12**, 252-255 (1985).
16. J. Weese, "A reliable and fast method for the solution of Fredholm integral equations of the first kind based on Tikhonov regularization," *Comput. Phys. Commun.* **69**, 99-111 (1992).
17. J. Nuyts, B. De Man, P. Dupont, M. Defrise, P. Suentens, and L. Mortelmans, "Iterative reconstruction for helical CT: A simulation study," *Phys. Med. Biol.* **43**, 729-737 (1998).
18. R. Jeraj, T. R. Mackie, J. Balog, G. Olivera, D. Pearson, J. Kapatoes, K. Ruchala, and P. Reckwerdt, "Radiation characteristics of helical tomotherapy," *Med. Phys.* **31**, 396-404 (2004).
19. D. W. O. Rogers, B. A. Faddegon, G. X. Ding, C.-M. Ma, J. Wei, and T. R. Mackie, "BEAM: A Monte Carlo code to simulate radiotherapy treatment units," *Med. Phys.* **22**, 503-524 (1995).

20. C.-M. Ma and D. W. O. Rogers, BEAMDP Users Manual Report Pirs-0509 (NRCC, Ottawa, Canada, 2004).
21. ICRU - International Commission on Radiation Units and Measurements, "Tissue substitutes in radiation dosimetry and measurement," ICRU Report No. 44 (International Commission on Radiation Units and Measurements, Bethesda MD, 1989).
22. <http://www.nist.gov/pml/data/xcom/index.cfm>.
23. K. Breitman, S. Rathee, C. Newcomb, B. Murray, D. Robinson, C. Field, H. Warkentin, S. Connors, M. Mackenzie, P. Dunscombe, and G. Fallone, "Experimental validation of the Eclipse AAA algorithm," J. Appl. Clin. Med. Phys. **8**(2), 76-92 (2007).
24. S. Saur, and J. Frengen, "GafChromic EBT film dosimetry with flatbed CCD scanner: A novel background correction method and full dose uncertainty analysis," Med. Phys. **35**(7), 3094-3101 (2008).
25. C. Lemmens, D. Faul, and J. Nuyts, "Suppression of metal artifacts in CT using a reconstruction procedure that combines MAP and projection completion," IEEE Trans. Med. Imaging. **28**(2), 250-260 (2009).

CHAPTER 5 : NMAR in kVCT using MVCT priors, a patient study

5.1 Introduction

In radiotherapy planning, kVCT images are used for the delineation of tumours as well as organs at risk, and for the calculation of radiation dose based on the electron density of tissues derived from the CT numbers. Therefore, the visual reduction of artifacts caused by metal implants as well as the accuracy of CT numbers becomes very important. The application of NMAR in kVCT with MVCT priors showed great promise for the reduction of metal artifacts in phantom kVCT images.¹ Restoration of correct CT number of both the metals and the tissue equivalent inserts as well as intact edge information of these inserts have made the corrected images more useful for quantitative (more accurate calculated dose and more accurate tissue delineation) and qualitative (lesser secondary artifacts and better visualization) purposes. In the study presented in chapter 4, there were some fine streaks, which emanate radially from the metallic rods, present in the corrected images. In this chapter, we introduce a method to further reduce these streaks. Also, we further evaluate our correction scheme as applied to the cancer patient images for better tissue visualization and dosimetric improvements. Since we saw very little difference (in dosimetry or visual clarity) for both IMRT and Rapid Arc plans in the kVCT images corrected using uncorrected or corrected MVCT prior, we use the uncorrected MVCT images as prior information in this study. This dramatically reduces the image correction time since we avoid the computationally extensive step that corrects MVCT

images. We call this NMAR approach the MVCT-NMAR method which uses the uncorrected MVCT prior image in the correction process.

In this study we used five patients in total: three with dual hip implants (all male with prostate cancer), one with a single hip implant (female with gynecological cancer), and one with dental fillings (male with head and neck cancer). Ethics approval for the study was obtained from Alberta Health Services. Only the image data of the patients are used in the study keeping all other patient information anonymous.

5.2 Methods

5.2.1 Streaking reduction

Figure 5.1 shows the flow diagram of the MVCT-NMAR algorithm. The *corrected image* is used as the *prior image* in an iterative scheme which reduces these remaining streakings. We have used three iterations (the final corrected image is the third time corrected image) as this degree of processing shows sufficient reduction of the streakings.

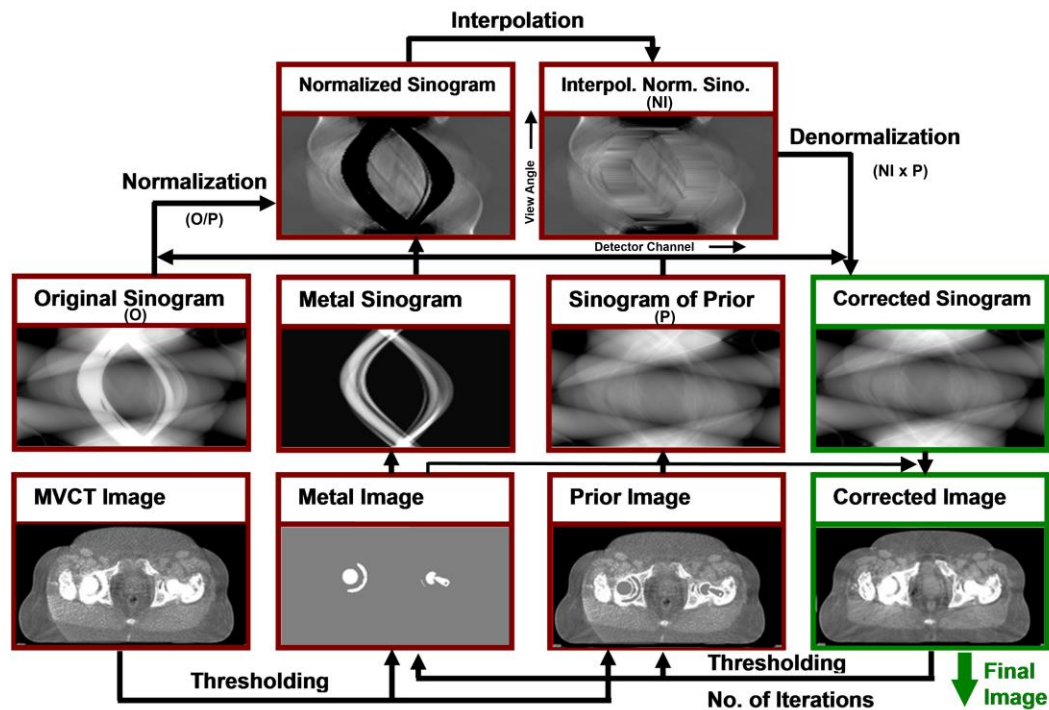


Figure 5.1. Flow diagram showing the MVCT-NMAR technique. In the corrected image, the metal pixels are set to zero and used again as the prior image in an iterative fashion to reduce the fine streakings. Metal pixels are inserted back in the final corrected image. Three iterations are used in this study.

5.2.2 Image reconstruction

The kVCT scanner that we used for all patient studies was a Philips Big BoreTM system. Patients were scanned in helical mode (source-detector rotating around the patient on an axially moving couch) with the following settings: 120 kVp, 500 mAs exposure for pelvic region (350 mAs for head and neck), 16x1.5 collimation, and 0.688 pitch. The 512x512 images were reconstructed with 3mm nominal slice thickness. Two sets of images, one uncorrected and the other corrected using the orthopaedic metal artifact reduction (OMAR)² algorithm were obtained from the same raw data. Both of these image sets contain pixels with 16-bit CT numbers and the reconstruction takes place within the system software.

All kVCT patient studies were part of the normal radiotherapy workflow and did not incur either additional patient dose or appointment time.

In this study, *the original sinogram* in Fig. 5.1 is obtained by forward projecting (using MatLabTM function *radon*) the uncorrected kVCT image (the map of CT numbers) in MatLabTM with pseudo-parallel beam geometry. This approach is chosen for two reasons. First, the actual fan-beam geometry including detector pitch may be present in the header of the raw data files of the system, but it is the proprietary information of Philips which is not accessible without a full non-disclosure agreement. The raw data of the detectors itself was accessible as it was used in the attenuation measurements in Chapter 3. Second, *the metal sinogram* and *the prior sinogram* must be obtained artificially from MVCT images by forward projecting *a metal image* and *a prior image* that need accurate geometry information for the TomoTherapyTM system. If the same pseudo-parallel beam geometry is used for both systems, then the error associated with geometrical mismatch or misinterpretation of the proprietary fan-beam geometry can be eliminated.

As a routine clinical protocol, the MVCT images (512x512) were acquired in TomoTherapyTM MVCT with a nominal slice thickness of 4 mm, although nominal slice thicknesses of 2 mm and 6 mm are also available. The patient in MVCT is scanned several days after taking the kVCT scan. Furthermore, the field of view (FOV) of MVCT and kVCT is generally different as the FOV for kVCT varies from patient to patient while the FOV for MVCT is fixed at ~40 cm. The 3D MVCT image set is registered with the uncorrected 3D kVCT image set using

a rigid registration (applying rotations and translations in 3D). Then the image slices from the 3D MVCT image data are created at the corresponding locations of kVCT image slices using a linear interpolation in the axial direction. Finally, the MVCT images at the new slice locations are transformed to pseudo-kVCT images by using the CT number vs density calibration tables for MVCT and kVCT used in the clinic. The process involves changing MVCT images to tissue density images using the MVCT calibration table, and then changing density images to pseudo-kVCT images using the kVCT calibration table. These tables contain materials ranging from air to high density metal (dental amalgam).

Two separate images are obtained from each pseudo-kVCT image using thresholding: *a metal image* in which the “metal pixels” with CT numbers > 3000 remain unaltered while all other pixels are set to zero, and *a prior image* with all the “metal pixels” set to zero and all other pixels unaltered. Thus the *metal image* and the *prior image* now have the same FOV and same size as the original uncorrected kVCT image. Forward projection (MatLabTM function *radon*) of the *metal image* and the *prior image* give the *metal sinogram* and the *prior sinogram*, respectively. The *original sinogram* (forward projection of the original, uncorrected kVCT image) is pixel-wise divided by the *prior sinogram* to get a *normalized sinogram*. The *metal sinogram* is used to identify the location of metal in the *normalized sinogram*. The projection data in these locations are replaced with the linearly interpolated data of the *normalized sinogram* in the detector channel direction from the surrounding data. The *normalized sinogram* after interpolation is denormalized by multiplying it pixel-wise with the *prior*

sinogram. These steps of normalization, interpolation and denormalization have been shown to reduce the secondary artifacts in the corrected image.⁵ The denormalized *sinogram* is now used to reconstruct the *corrected image* (using the MatLabTM function *iradon*) after which the *metal image* is patched back into the *corrected image* to insert the metal information. In the second iteration, this *corrected image* is put into the iterative loop where the *metal image* and the *prior image* are now constructed by using thresholding in exactly the same way we described above. After two more iterations (3 including the first corrected image), the *final corrected image* is obtained.

5.2.3 Dosimetric evaluations

In our clinic, patients having pelvis disease and dual hip prostheses are often treated on TomoTherapyTM Hi-Art machines using OMAR corrected kVCT images for planning purposes. An inverse plan is created and optimised in the TomoTherapyTM treatment planning system with beams blocked through the prostheses, i.e., when the prosthesis is in the beam's eye view of a beamlet, the beamlet weight is set to zero.

In this study we used the image set of patient no 3, a prostate cancer patient with implanted dual hip prostheses, for the dosimetric evaluations. The prescription dose was 78 Gy with the constraint that 100% of the PTV should contain 95%-105% of the prescription dose. Two plans, one with the beams blocked through the prostheses and the other unrestricted, were generated and optimized on an OMAR corrected image set. Those two plans were then applied on an MVCT-NMAR corrected image set utilized as a delivery quality assurance

(DQA) phantom and the dose distributions were recalculated. Then, the dose distributions as a function of image correction method (OMAR vs MVCT-NMAR) as well as a radiotherapy plan type (blocked vs unblocked) were evaluated.

5.3 Results

5.3.1 Image quality evaluation

Figure 5.2 shows the images of prostate cancer patient no. 1 with dual hip prostheses. Figure 5.2(a) shows the uncorrected image which contains severe streaking and shading. These artifacts are significantly reduced in all the corrected images: the OMAR corrected image [Fig. 5.2(b)] and the MVCT-NMAR corrected image with one iteration [Fig. 5.2(c)] or three iterations [Fig. 5.2(d)]. However, there are important differences among these corrected images. The fine streakings in Fig. 5.2(c), emanating from the implants and distributed radially, are reduced in Fig. 5.2(d). In the OMAR corrected image [Fig. 5.2(b)], there is a band of dark shadow connecting the hip implants. Above and below this band are horizontal bands of bright shadow which obscure a part of the bladder and its interface with surrounding structures including rectum (arrow 1). Besides, there are other bands of bright and dark shadow oriented in various directions. Parts of the high contrast bony anatomy close to the implants in Fig. 5.2(b) are missing (arrow 2). Also, some of the soft tissue structures close to the implants are blurred (arrow 3). Due to this blurring one cannot resolve two closely located tissue

structures. All of these artifacts are greatly reduced, in fact are removed, in the MVCT-NMAR corrected image in Fig. 5.2(d).

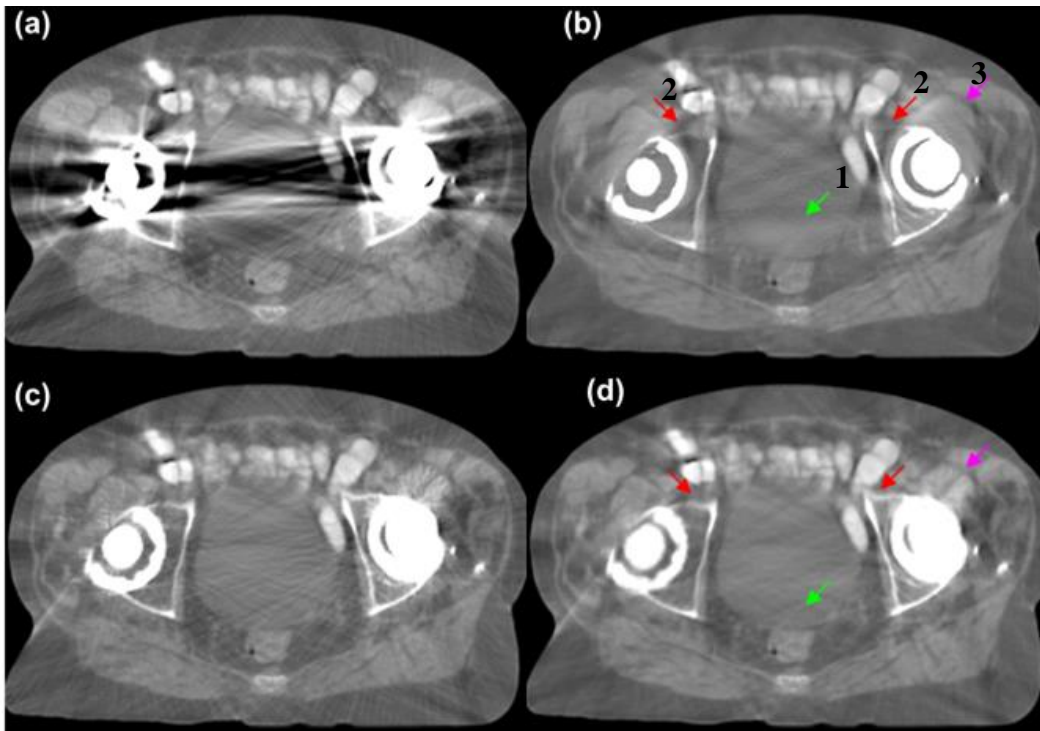


Figure 5.2. (a) Original uncorrected image (b) OMAR corrected image, MVCT-NMAR corrected images after (c) one iteration and (d) three iterations. The streaks present in (c) are successfully removed in (d). In (b) arrows 1, 2, and 3 show an obscured region anterior to the bladder-rectum interface, lost bone information, and blurred soft tissue close to metal implant, respectively. All of these artifacts are removed in (d) shown by the respective arrows.

Similar results are seen in the image of patient no. 2 [Fig. 5.3], a prostate cancer patient with dual hip implants. A band of dark shadow connecting the implants can be seen along with other bands of bright and dark shadows in the image corrected by the OMAR algorithm. The two horizontal bright bands that we saw in Fig. 5.2, above and below this dark band, are also present in this image. Moreover, about 50% of the bladder pixels have higher than normal CT numbers due to the bright band whereas the other 50% of pixels have lower CT numbers. This results in an incorrect density map in the same structure (bladder). These

artifacts are significantly reduced in the MVCT-NMAR corrected image where tissue structures and their interfaces, mainly in the bladder/rectal area, can be seen more clearly and have more accurate CT numbers.

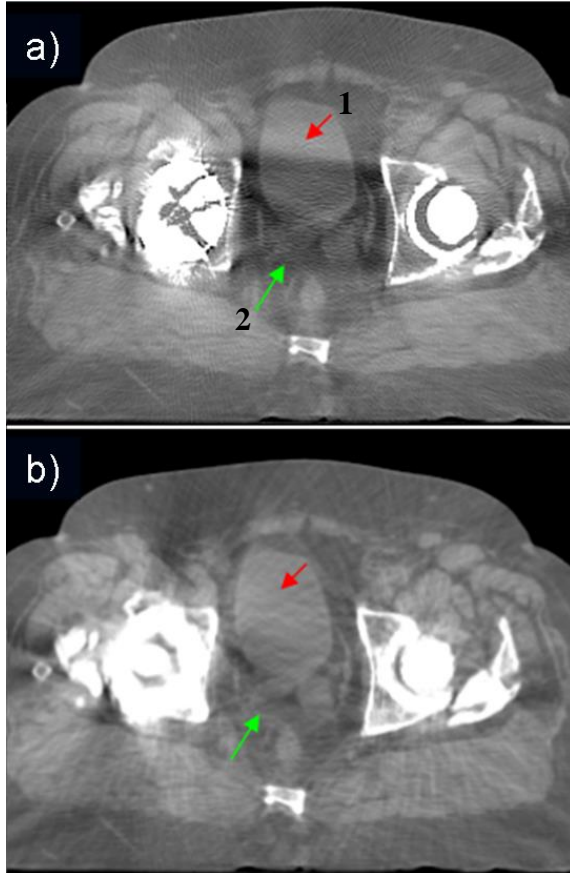


Figure 5.3. (a) OMAR corrected image and (b) MVCT-NMAR corrected image of a prostate patient with dual hip implants. In (a) arrow 1 shows part of the bladder with higher CT number and arrow 2 shows an obscured region near the bladder-tissue interface. These artifacts are removed in (d) shown by the respective arrows.

To see the effect of artifact reduction in the planning target volume (PTV), the area that contains the highest radiation dose, we compared the corrections in four successive image slices (of patient 2) which contain prostate, bladder and rectum. The image slices corrected by the OMAR algorithm [first row in Fig. 5.4] contain band and streaking artifacts that obscure the prostate and its interface (indicated by arrows 1) with bladder or rectum. In each corresponding slice of the

MVCT-NMAR corrected image, prostate is seen very clearly within clear surroundings. The bladder in the OMAR corrected images [Fig. 5.4(a) and (d)] has higher CT number (arrow 2) and cannot be distinguished from the prostate. But these shortcomings are improved in the MVCT-NMAR corrected images [Fig. 5.4(c') and (d')]. In all four slices of the OMAR corrected image [Fig. 5.4(a-d)], large regions in the pubic bone are eroded (arrows 3) whereas they are intact in the MVCT-NMAR corrected images [Fig. 5.4(a'-d')].

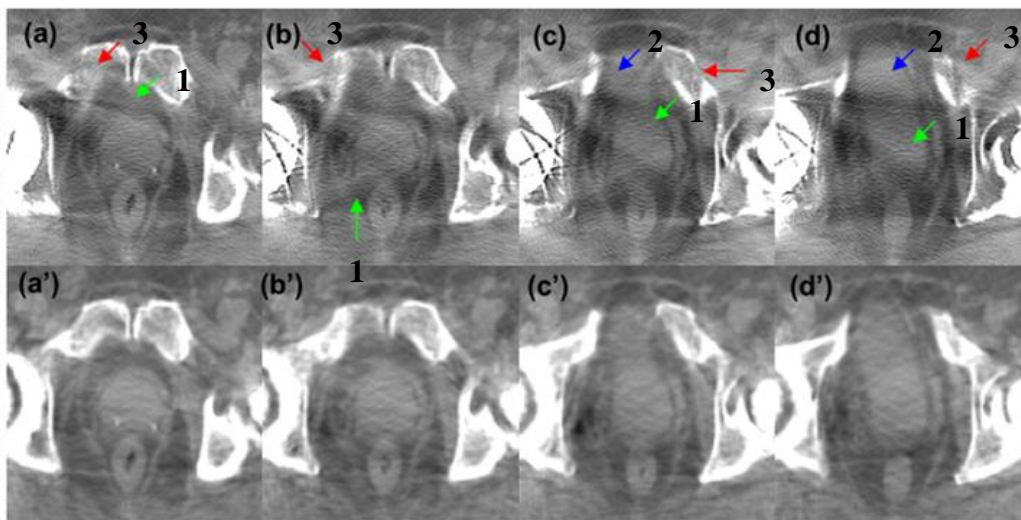


Figure 5.4. Four successive image slices of patient no 2 showing prostate, bladder and rectum. The images in the top row (a-d) are corrected by the OMAR algorithm and those in the bottom row are corrected using the MVCT-NMAR method. In the OMAR corrected images, arrows 1 show an obscured region near the prostate-bladder or prostate-rectum interface, arrows 2 show bladder with higher CT number and arrows 3 show eroded bone regions. These artifacts are removed in the MVCT-NMAR corrected images making tissue structures more visible.

The corrected images of patient no. 4, the patient with gynecological cancer and bearing single hip prosthesis, are shown in Fig. 5.5. In comparison to the images of patients with dual hip prostheses, the images corrected by the OMAR algorithm contain fewer areas with band and streaking artifacts. However, the blurred soft tissue structures (arrow 1), eroded bone (arrow 2) and bright band of artifact (arrow 3) below the implant that extends horizontally are still there.

Particularly, this bright band obscures the tissues and their interfaces in the bladder/rectum region. These artifacts are removed in the MVCT-NMAR corrected image, making it better suited for tissue visualization and obtaining accurate CT numbers for anatomical structures.

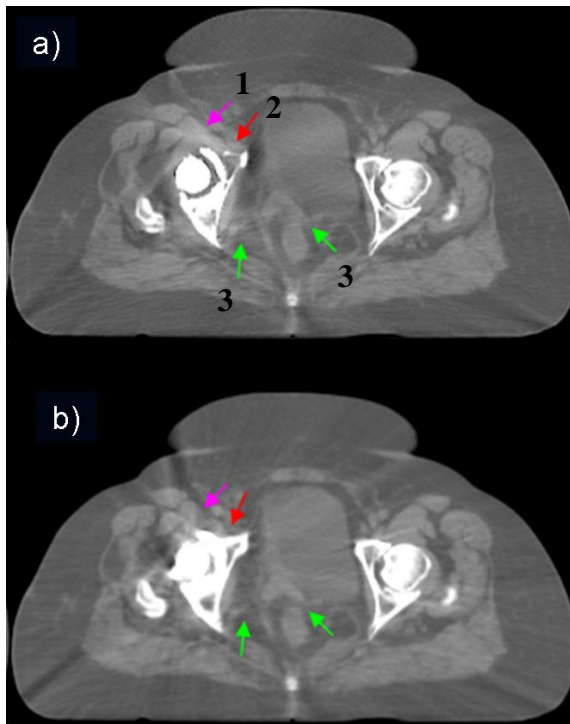
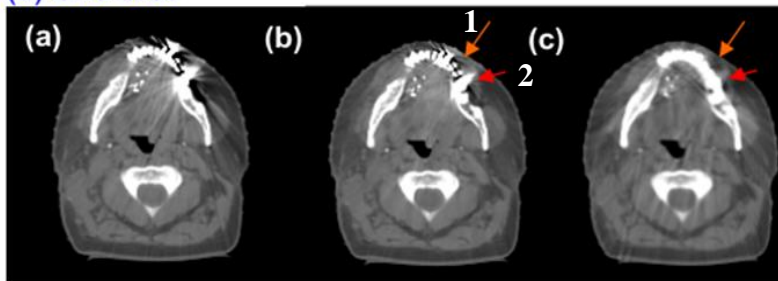


Figure 5.5. (a) OMAR corrected image and (b) MVCT-NMAR corrected image of a female patient with a single hip prosthesis. In (a) arrow 1 shows blurred soft tissue close to the implant, arrow 2 shows eroded bone, and arrows 3 show obscured regions near bladder-tissue-rectum interfaces. These artifacts are removed in (b) as shown by the respective arrows.

(a) One slice



(b) Next slice

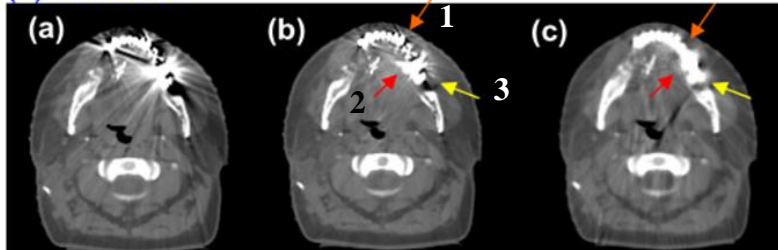


Figure 5.6. Two successive image slices of a head and neck patient with dental implants: (a) uncorrected images; (b) OMAR corrected images; and (c) MVCT-NMAR corrected images. In (b) for both slices arrow 1 shows remaining artifacts, arrow 2 shows false bony anatomy, and arrow 3 shows a false air gap. These artifacts are removed in (c) as shown by the respective arrows.

The images for two successive slices of a head and neck cancer patient containing dental implants (patient no 5) are shown in Fig. 5.6. There are very bright and very dark streakings in the uncorrected images, some of which are reduced but still present in the images corrected by the OMAR algorithm (arrows 1). There are areas in the image containing false bone (arrows 2) or a false air gap (arrow 3). In the MVCT-NMAR corrected images these artifacts are significantly reduced.

The images corrected by MVCT-NMAR images are slightly blurred compared to the OMAR corrected images. This is partly because³ the OMAR corrected image uses the original raw sinogram whereas we have used generated sinogram by forward projecting the original uncorrected image for MVCT-NMAR method. The other reason could be due to the nature of image

correction technique⁴ that OMAR adds an error image to the original uncorrected image whereas MVCT-NMAR corrects the sinogram itself before using it for the image reconstruction.

5.3.2 Dosimetric evaluations

Figure 5.7 shows a comparison of dose distributions in MVCT-NMAR corrected and OMAR corrected images for an unblocked beam plan. The plan is optimised in the OMAR corrected images of patient no. 3, a prostate cancer patient with implanted dual hip prostheses. The comparison of differential dose histogram within the PTV in two corrected image sets is shown in Fig. 5.7(a). A relative shift in the distribution (indicated by an arrow) can be seen in the figure, showing the existing difference. This difference results from the fact that the metal information inside the implants in the OMAR corrected images is incorrect because of a large cupping artifact present inside a solid implant.³ This artifact in the OMAR corrected image incorrectly lowers the density of metal in these corrupted voxels. With the more accurate higher density of metal in the MVCT-NMAR corrected image, the beam gets attenuated more before reaching the PTV and hence we observe a lower dose (the shift is towards the lower dose in the differential dose histogram) in the MVCT-NMAR corrected image. Figure 5.7(b) shows the dose profile comparison along a line through the image, as indicated in the inset. There is a lower dose in all the voxels within the PTV in the MVCT-NMAR corrected image compared to the dose in the OMAR corrected image. Although the dose difference is only about 1%, this difference can become

larger if a larger implant or higher density metal or both are present in the image slice containing PTV.

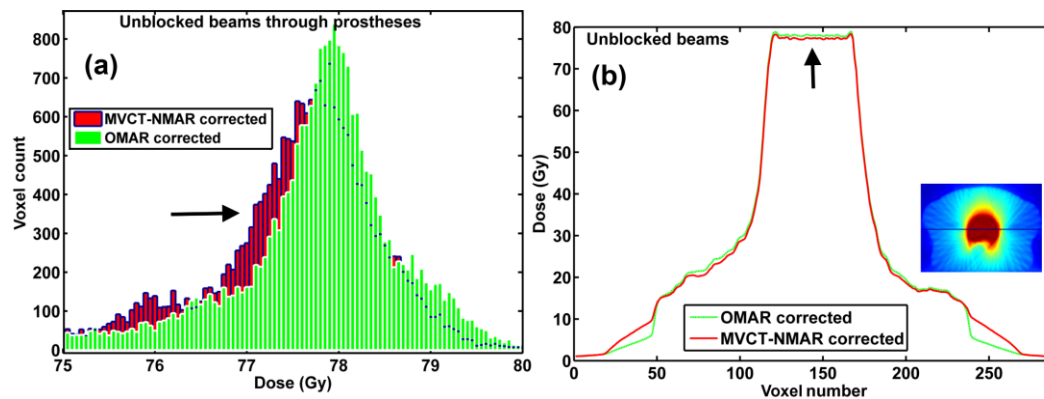


Figure 5.7. (a) Differential dose histogram in the planning target volume (PTV) showing the difference in dose of image sets corrected by the MVCT-NMAR and OMAR algorithms for a radiotherapy plan created without blocking the beams through the prostheses. The plan was optimized on an OMAR corrected image set and recalculated on an MVCT-NMAR corrected image set. (b) The dose profiles through the PTV of these images (along a line shown in the inset) show a small (shown by arrow) but constant dose difference. The difference results from the lower CT number inside the metal prostheses and in the shaded region between them in the OMAR corrected images.

The dose profiles in the MVCT-NMAR corrected image for the plans with blocked and unblocked beams through the prostheses are shown in Fig. 5.8 for two image slices that contain the PTV. We chose the MVCT-NMAR corrected images for this purpose because the CT number of both metal and tissues are more accurate in these images compared to the OMAR corrected images.¹ In both Fig. 5.8(a) and Fig. 5.8(b), the dose within the PTV is basically the same for both the plans. However, a large difference in dose can be seen in almost all the voxels just outside the PTV. The dose in these voxels in the blocked beam plan is always higher than in the unblocked beam plan. In Fig. 5.8(b), a point in the pubic bone (see the inset image) shows 59.23 Gy dose in the blocked beam plan compared to 52.51 Gy dose in the unblocked beam plan, which amounts to a 12.8% increase in

dose in the blocked beam plan. Above and below this point, the dose differences are similar. In fact, almost all the slices containing PTV showed this trend.

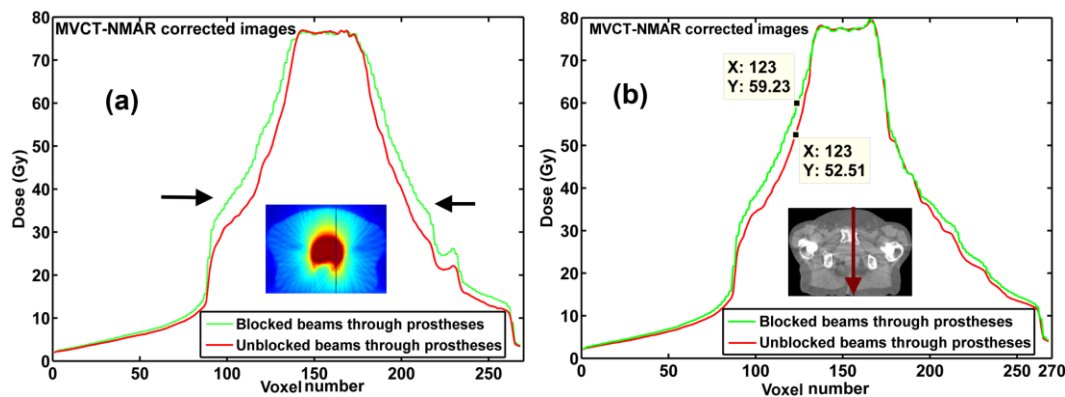


Figure 5.8. (a) Dose profiles through a slice containing PTV, along a line as shown in inset, in the image corrected by MVCT-NMAR using two plans (one with beams blocked through the prostheses and the other with beams unblocked) showing significantly higher dose outside PTV in the blocked beam plan compared to the dose in unblocked plan. (b) Similar dose profiles in another slice containing pubic bone where there is 12.8% higher dose in the blocked beam plan compared to the unblocked beam plan. Inset in (a) is the dose distribution image whereas the inset in (b) is the CT image.

5.4 Discussion

Both the visual appearance and the accuracy of CT number information are necessary for radiotherapy treatment planning. In previous studies^{6,7} with OMAR, it was pointed out that the only major benefit of OMAR comes from its better visualization of the structures (in radiotherapy planning where the beams were not passing through the metallic implant) so that the tissues could be delineated with increased confidence. In this study, we showed that the patient images corrected using the MVCT-NMAR method contain more accurate information, and have far fewer secondary artifacts compared to the image corrected by the commercial OMAR algorithm. In patients having either a single or dual hip prosthesis, the secondary artifacts in the OMAR corrected images obscure parts of the tissue structures. These artifacts can make it hard to identify

tissue boundaries. In radiotherapy treatment planning, it is vital that we correctly outline the planning target volume containing tumor as well as the surrounding tissues or the organs that are healthy. The blurring in soft tissue and eroded bony anatomy can lead to a false delineation. The OMAR algorithm makes a prior image using thresholding and segmentation from the original kVCT image, in a very similar way as the general normalized metal artifact reduction (NMAR) technique does. In earlier studies,^{1,8,9,10} the erosion of a high contrast structure like bone is shown to be present in NMAR corrected images, and other studies have shown^{1,8} that these artifacts stem from the non-optimal prior image. Our observation of the erosion of bony anatomy in OMAR corrected images is consistent with those studies in NMAR. In the patient with dental implants, significant amounts of artifact are still present in the OMAR corrected images that were present in the uncorrected image. This makes images less useful for diagnostic and tissue delineation purposes. In our clinical practice for head and neck patients, these artifacts need manual delineation and density setting to that of water. In all the patients, the images corrected by MVCT-NMAR do not contain these artifacts (blurring of tissues, obscuring of structures, erosion of bones, remaining primary artifacts) making them more useful for radiotherapy treatment planning.

In the clinic, beams are usually not passed through the metallic prostheses because of the lack of correct information of metal in kVCT images. Earlier evaluation study⁷ of the OMAR algorithm in the patients with pelvic region cancers showed a clinically insignificant difference in the dose distribution

between the images corrected by OMAR and an uncorrected image where the artifact region was overridden by the density of water. The IMRT plan evaluated in the study had beams arranged not to pass through the implants. In our case, the small pilot study showed that the dose outside the PTV is demonstrably higher in the treatment plan that avoids the beams through prostheses, in comparison to the unrestricted beam plan in TomoTherapy™ planning. The OMAR technique does not restore the lost information inside the metal implants¹ due to the metal artifacts and hence any radiotherapy plan that consists of beams passing through the prostheses can have large dose difference compared to the dose in an ideal image. The density of metal inside the patient can only be found from MVCT imaging as kVCT attenuation data is completely inaccurate due to photon starvation as described in Chapter 3. If the correct information of metal is obtained, as is the case in MVCT-NMAR corrected images, the dose outside the PTV can be significantly reduced when the beams are not blocked through the prostheses. A large dose in the healthy tissues (around 59 Gy) can be reduced (to around 52 Gy) so that damage to the healthy tissues is less. Thus, MVCT-NMAR corrected images can provide two major benefits in radiotherapy treatment planning compared to the commercially corrected (with OMAR) images: (1) more accurate diagnosis or more accurate delineation of tumor/tissue structures due to better visualization and fewer secondary artifacts, and (2) more accurate dose distribution in addition to significantly lower dose in healthy tissues yet optimally covering the planning target volume.

In this study, we used MVCT and kVCT images from two different scanners requiring that patients be scanned at two different times. Rigid registration of the 3D image sets was used to obtain prior images. In this scenario, it is very likely that significant anatomical changes in terms of tissue shape, size and position can occur between two scans. A patient's body is not perfectly rigid and mismatch in the position and orientation of metallic implants due to patient positioning differences can result in registration differences between MVCT and kVCT images. Furthermore, the regions containing air or gas (rectum, oral cavity etc.) can easily change their positions. Moreover, there is a relatively larger partial volume effect in the axial direction (along the slice thickness) in the MVCT images due to an increased slice thickness. All of these changes can introduce significant secondary artifacts in the MVCT-NMAR corrected image due to a reduction in "closeness" of the prior image from the correct image. This is because the closeness of the *prior image* to the actual object in this type of correction scheme (normalized metal artifact reduction⁵) is critical^{1,8} to the success of metal artifact reduction. The use of deformable registration and a similar slice thickness for MVCT and kVCT may reduce these uncertainties, and future studies employing these strategies should be conducted. However the improvements in the MVCT-NMAR corrected images presented in this study strongly support the development of an MVCT imaging modality sharing the same gantry with a kVCT imaging unit.

5.5 Conclusions

The use of MVCT images to correct kVCT images in the MVCT-NMAR technique greatly reduces metal artifacts, avoids secondary artifacts, and makes patient images more useful for accurate dose calculation in radiotherapy. These are significant improvements over the commercial correction method, and can be realized provided a correct registration of the MVCT and kVCT images is achieved. A large dose reduction is possible outside the planning target volume (e.g. 52.5 Gy vs 59.2 Gy in pubic bone for a prostate cancer patient) when MVCT-NMAR corrected images are used without constraining beams to avoid prostheses in TomoTherapy™ treatment plans. Thus the use of MVCT-NMAR corrected images in radiotherapy treatment planning could be beneficial and may raise the quality of cancer treatment for patients having metallic implants.

5.6 References

1. M. R. Paudel, M. Mackenzie, B. G. Fallone, and S. Rathee, "Evaluation of NMAR in kVCT using MVCT prior images for radiotherapy treatment planning," *Med. Phys.* **40**, 081701 (2013).
2. Metal Artifact Reduction for Orthopedic Implants (O-MAR). Philips HealthCare System 2012 [URL: [http://clinical.netforum.healthcare.philips.com/us_en/Explore/White-Papers/CT/Metal-Artifact-Reduction-for-Orthopedic-Implants-\(O-MAR\)](http://clinical.netforum.healthcare.philips.com/us_en/Explore/White-Papers/CT/Metal-Artifact-Reduction-for-Orthopedic-Implants-(O-MAR))].
3. M. Bal and L. Spies, "Metal artifact reduction in CT using tissue-class modelling and adaptive prefiltering," *Med. Phys.* **33**, 2852-2859 (2006).
4. H. Li, C. Noel, H. Chen, H. Harold, D. Low, K. Moore, P. Klahr, J. Michalski, H. A. Gay, W. Thorstad, and S. Mutic, "Clinical evaluation of a

- commercial orthopedic metal artifact reduction tool for CT simulations in radiation therapy,” *Med. Phys.* **39**, 7507-7517 (2012).
5. E. Meyer, R. Raupach, M. Lell, B. Schmidt, and M. Kachelriess, “Normalized metal artifact reduction (NMAR) in computed tomography,” *Med. Phys.* **37**, 5482-5493 (2010).
 6. H. Li, C. Noel, H. Chen, H. Harold, D. Low, K. Moore, P. Klahr, J. Michalski, H. A. Gay, W. Thorstad, and S. Mutic, “Clinical evaluation of a commercial orthopedic metal artifact reduction tool for CT simulations in radiation therapy,” *Med. Phys.* **39**, 7507-7517 (2012).
 7. C. Glide-Hurst, D. Chen, H. Zhong, and I. J. Chetty, “Changes realized from extended bit-depth and metal artifact reduction in CT,” *Med. Phys.* **40**, 061711 (2013).
 8. S. Karimi, P. Cosman, C. Wald, and H. Martz, “Segmentation of artifacts and anatomy in CT metal artifact reduction,” *Med. Phys.* **39**, 5857-5868 (2012).
 9. E. Meyer, R. Raupach, M. Lell, B. Schmidt, and M. Kachelriess, “Frequency split metal artifact reduction (FSMAR) in computed tomography,” *Med. Phys.* **39**, 1904-1916 (2012).
 10. K. V. Slambrouck, and J. Nuyts, “Metal artifact reduction in computed tomography using local models in an image block-iterative scheme,” *Med. Phys.* **39**, 7080-7093 (2012).

CHAPTER 6 : Conclusions and future work

6.1 Conclusions

Computed tomography (CT) in radiotherapy treatment planning is mainly used for two purposes: to delineate tumors and organs at risk, and to obtain the electron density distribution required for radiation dose calculation. High density/high atomic number metallic objects create shading and streaking in the CT image, often termed *metal artifacts*. Metal artifacts may lead to missing or false anatomical information, create an impediment for proper visualization of the internal structures of interest, and provide incorrect electron density information in some voxels of the image. This can cause an inaccurate delineation of anatomical structures or inaccurate radiation dose calculation, resulting in poorly designed treatment plans. The American Association of Physicists in Medicine (AAPM) task group report #63 suggests that 1%-4% of cancer patients' diagnosis/treatment can be adversely affected by the presence of metallic implants such as hip prostheses, dental fillings and other such medical implants. Hip prostheses and dental fillings pose a serious problem for radiotherapy treatment planning of pelvic, and head and neck region cancers.

We designed studies to understand these metal artifacts and developed techniques for reducing them in both MVCT and kVCT images; with the goals of minimising the introduction of secondary artifacts so that the corrected images could be used in radiotherapy with increased confidence to delineate the tissue structures, and to obtain more accurate electron density information of not only the tissue structures but also the metallic implants.

Our study in chapter 2 demonstrates the importance of model based image reconstruction in two MVCT systems for metal artifact reduction. The study shows that given accurate geometrical information of the CT scanner and the photon beam spectrum, the shading metal artifacts can be almost completely removed in MVCT images using an iterative reconstruction algorithm such as IMPACT. The error in CT number, and consequently the error in electron density, is significantly reduced by this method. The difference in the electron density in the plexiglass background is $< 1\%$, and it is $< 3\%$ averaged over the range of electron densities (0.295 - 1.695 relative to water) investigated. However, the accurate modeling of detectors' energy dependent response and a model for the energy dependence of relevant photon interaction processes are found to be crucial for the successful implementation of the method.

The study in chapter 3 shows that photons reaching the kVCT detector are either so low in number that the signal measured has large quantum noise, or that the photons are completely absorbed inside the attenuating plate so that the discrete quantization levels become visible in the plot of *measured attenuation vs views*, for steel thickness greater than or equal to 13 mm. This is the condition of *photon starvation*. Therefore, the measured signal does not follow the signal model used in the IMPACT algorithm. As such, the modified IMPACT technique that uses a realistic signal model for the measured data can not model photon starvation, nor can we introduce any model for this effect. The practical size of a steel hip implant is at least 13 mm and hence we can not apply a model based

method like modified IMPACT to reduce metal artifacts in kVCT for higher density implants.

In chapter 4, we used prior information from MVCT images to correct artifacts in kVCT. The study shows that the use of MVCT images without tissue classification as priors, both with and without artifact correction, greatly reduces metal artifacts in kVCT without deforming anatomical structures. The light streaks originating from the metals in the corrected images do not obscure the structures. The CT numbers for both the metal and the other tissue inserts in the RMI phantom are close to the reference image (the metal artifact-free image reconstructed in the absence of metal, but with the metal information artificially patched). The radiation doses calculated on these corrected images are closer to the doses in the reference image; within 2.7% and 5%, respectively, with corrected MVCT and uncorrected MVCT priors in a parallel opposed beams plan. Although the kVCT prior creates far fewer streaks in the corrected image than does the MVCT prior, the kVCT prior creates structural deformation, edge distortion, and large quantitative error in metal CT numbers. These result in large deviation (~15.5%) of the radiotherapy dose at the isocenter compared to the corresponding dose in the reference image.

Finally, in chapter 5, we applied the algorithm developed in chapter 4 to four patient images containing single or bilateral hip prostheses, and a patient with dental fillings. We also modified the algorithm in chapter 4 to further reduce the remaining fine streaks (we called the modified algorithm MVCT-NMAR technique). The use of MVCT images to correct kVCT images in the

MVCT-NMAR technique greatly reduces the metal artifacts, avoids secondary artifacts, and makes patient images more useful for accurate dose calculation in radiotherapy. These are significant improvements over the commercial OMAR correction method and depend upon accurate registration of the MVCT and kVCT images. The remaining and the secondary artifacts such as the blurring of soft tissues, erosion of bony anatomy, false bony structures or air gaps, and large cupping artifact inside metal implants present in the commercially corrected images are removed in the images corrected using our MVCT-NMAR method. Large dose reduction is possible outside the planning target volume (e.g. 52.5 Gy vs 59.2 Gy in pubic bone for a prostate cancer patient) when these MVCT-NMAR corrected images are used without requirement that beams avoid passing through prostheses in TomoTherapyTM treatment plans. Thus the use of MVCT-NMAR corrected images in radiotherapy treatment planning could be beneficial and may raise the quality of cancer treatment for the patients having metallic implants.

6.2 Future work

In this project, we evaluated a very small number of patients. With a large number of patients, statistical evaluation (using the chi-square test or Wilcoxon signed rank test) and receiver operating characteristics (ROC) analysis of the visual clarity of the corrected images would be possible with the involvement of radiologists/radiation oncologists. A comparative study of the changes in the dose distribution with changes in the volume of the PTV and organs at risk due to artifact correction could be undertaken with the commercially corrected images.

Our finding of increased dose outside PTV in chapter 5 suggests that statistical evaluation of the change in dose due to the directional beam blocks be made in a large number of patients. This evaluation can be extended to other treatment planning methods (such as IMRT, Rapid Arc etc.). The dosimetric evaluations could be made in other areas (such as the head and neck region) in addition to the pelvic region. A reduction of the slice thickness of MVCT images to reduce the partial volume effect (and hence to reduce registration errors) requires ethics approval. Deformable rather than rigid registration of the MVCT images might also reduce the registration errors.

The major limitation in applying our method using state of the art radiotherapy equipment and treatment protocols stems from the registration error between MVCT and kVCT images. So, future studies could profitably be focussed on developing a modality or extending existing radiotherapy equipment for the purpose of acquiring MVCT and kVCT images simultaneously, preferably using the same gantry, so that the registration issue could be completely removed. The addition of a kVCT scanner to a TomoTherapyTM system (at a right angle to the MVCT beam, as planned originally), or the development of MV cone beam CT using the existing flat panel porter imager of a VarianTM linac in conjugation with an on-board imager represent two possibilities for extending existing resources.